UNIVERSITAT DE
BARCELONA

Implementation of the direct force measurement method in optical tweezers

Frederic Català i Castro

Implementation of the direct force measurement method in optical tweezers

Programa de doctorat en Nanociències

Autor: Frederic Català i Castro

Directors: Dra. Estela Martín-Badosa
Dr. Mario Montes-Usategui

Tutora: Dra. Estela Martín-Badosa

Departament de Física Aplicada

Universitat de Barcelona

Setembre de 2018

UNIVERSITAT DE BARCELONA

Resum

Les pinces òptiques són una eina que permet la manipulació d'objectes de mida micromètrica mitjançant llum làser. En no ser necessari el contacte mecànic directe sobre una mostra, els dóna la característica de ser una eina no invasiva, fet que obre moltes aplicacions en nombrosos camps de la biologia, com ara en estudis de mecànica cel·lular en teixits.

A més a més, una pinça o trampa òptica pot emprar-se per tal de realitzar mesures quantitatives, com ara posicions i forces amb precisió de nanòmetres (10^{-9}) i femto-Newtons (10^{-15}). D'aquesta manera, magnituds que altrament foren inaccessibles, com ara la força en un contacte cel·lular, poden obtenir-se i engegar així una nova dimensió en la recerca en biomecànica.

El mètode de mesura directa de forces analitza els canvis en el moment lineal dels fotons que conformen el feix per tal de mesurar forces òptiques. Aquest mètode permet de mesurar forces sense dependre d'un alt control experimental, cosa que fa possible la mesura de forces, per exemple, en objectes irregulars. Per contra, això és gràcies a un disseny experimental capaç de capturar tota la llum que crea la pinça òptica i de mesurar-ne els canvis de moment.

En la meva tesi doctoral, demostrem l'aplicabilitat del mètode en situacions en què la força no es pot obtenir de manera indirecta a partir de tècniques de calibració. En primer lloc, analitzem les millores tècniques que fan del mètode de detecció de moment una eina robusta per tal de realitzar mesures de força en un ampli ventall de situacions experimentals.

Seguidament, emprem pinces òptiques controlades hologràficament per tal d'atrapar objectes irregulars, com ara sistemes de múltiples esferes i micro-cilindres, i mostrem la capacitat de mesurar l'intercanvi de moment entre el feix i les partícules que dóna lloc a les forces òptiques. Un altre aspecte que analitzem àmpliament gràcies a aquesta tècnica de mesura és l'escalfament que origina una trampa òptica sobre el medi que envolta la partícula atrapada. Finalment, ens endinsem en la biologia de teixits per esbrinar com la dispersió a través d'aquests afecta el moment del feix i, per tant, les mesures.

Les meves conclusions demostren l'aplicabilitat del mètode de mesura en situacions en què la calibració *in situ* pot esdevenir molt complicada o, fins i tot, impossible. Podem considerar que, per tant, el camp d'aplicació de les pinces òptiques anirà creixent i trobarà nous experiments en què s'elucidaran alguns dels interrogants més importants de la biologia.

Abstract

Mechanics is the branch of physics that studies movement and force, and plays an evident role in life. The swimming dynamics of bacteria in search of nutrients, organelle transport by molecular motors or sensing different kinds of stimuli by neurons, are some of the processes that need to be explained in terms of mechanics.

At a human scale, distance and force can be measured with a ruler and a calibrated spring. However, assessing these magnitudes may become an important challenge at a micron scale. Among several techniques, optical tweezers stand out as a non-invasive tool that is capable of using light to grab micron-sized particles and measuring position and force with nanometer (10^{-9}) and femto-Newton (10^{-15}) accuracy. Small specimens, such as a bacterium or a cell membrane, can be trapped and effectively manipulated with a focused laser beam. Light momentum exchanged with the trapped sample can be used for eventually measuring the otherwise inaccessible forces that govern biological processes.

Optical tweezers have enabled, after trapping cell vesicles in vivo, to measure the pulling force exerted by molecular motors, such as kinesin. Flagellar propulsion forces and energy generation have been investigated by optically trapping the head of a bacterium. Cell membranes have been deformed with optical tweezers and the underlying tension determined.

However, the exact forces exerted by optical tweezers are difficult to measure beyond the in vitro approach. In order to calibrate the optical traps, the trapped samples often need to be spherical or present some degree of symmetry, it is important to bear information on the experimental parameters, and one needs high control of several variables that determine the trapping dynamics, such as medium homogeneity and temperature.

A cutting-edge method, developed in the Optical Trapping Lab – BiOPT, from the Universitat de Barcelona, targets the light-momentum change as a direct reading of the force exerted by an optical trap. This frees experiments from the necessity of calibrating the optical traps, and makes possible to perform accurate force measurement experiments in vivo and involving irregular samples.

In my PhD thesis, the direct force detection method for optical tweezers has been implemented and tested in some of such situations. I first give a technical description of the set-up used for the experiments. The use of a spatial light modulator (SLM) for holographic optical tweezers (HOTs), a piezo-electric platform to induce drag forces, and the trapping laser emission characteristics, are explained in detail.

The light-momentum set-up is tested against certain situations deviating from the ideal performance and some steps for optimization of several effects are analyzed. Backscattering light loss is quantified through experiments and numerical simulations and finally assessed to account for an average $\pm 5\%$ uncertainty in force measurements.

Then, the method is used to measure forces on irregular samples. First, arbitrary systems composed of microspheres of different kinds are collectively treated as irregular samples, in which the global momentum exchanged with the trapping beam coincides with the total Stokes-drag force. Second, pairs of optical tweezers are used to stably trap cylinders of sizes from 2 μm to 50 μm and measure forces in accordance with slender-body hydrodynamic theory.

Another aspect of the thesis deals with the temperature change induced by water absorption of IR light, which is one of the major concerns within the optical trapping community. As main reasons, accurate knowledge of local temperature is needed for understanding thermally-driven processes, as well as eventual damage to live specimens. Here we use direct force measurements to detect changes in viscosity that are due to laser heating, and compare the results with heat transport simulations to discuss the main conclusions on this effect.

The last goal of my thesis has been the implementation of the method inside tissue. The laser beam is affected by the scattering structures present in vivo, such as refractive index mismatches throughout different cells, nuclei, cell membranes or vesicles. As a primary result, despite the trapping beam is captured beyond 95%, I quantified this effect to result in an increase in the standard deviation of force measurements around $\pm 20\%$. The approach has consisted in comparing the trapping force profiles of spherical probes in vitro (water) and in vivo (zebrafish embryos).

To conclude, I here demonstrate that the direct force measurement method can be applied in an increasing number of experiments for which trap calibration becomes intricate or even impossible. Quantitative measurements become feasible in samples with unknown properties, the more important examples being arbitrary, non-spherical samples and the interior of an embryonic tissue.

Contents

1. Overview

State-of-the-art research in biology requires novel techniques with the ability to shed light into an ever-increasing number of unanswered questions. Understanding nature at the cell scale was primarily possible thanks to the advances of optics and microscopy during the past century. X-ray crystallography revealed the characteristic molecular structure of DNA. Nuclear magnetic resonance paved the way to carrying out a number of biochemical studies.

The role of force in biological processes has been of increasing interest in the past decades. This has triggered the invention of a number of techniques that target, by using different strategies, the small forces governing such processes. For single-molecule force spectroscopy, the most common techniques are atomic-force microscopy (AFM), magnetic tweezers and optical tweezers [1]. Other techniques, which are applicable in cell culture and on living tissues, are based on laser ablation, optogenetics and traction force microscopy. [2, 3]

Optical tweezers enable contact-less manipulation of samples ranging from tens of nanometers to tens of microns [4, 5, 6, 7, 8]. Compared, for instance, to the manipulation capabilities of magnetic tweezers and AFM, optical tweezers require no additional magnetic probes to trap a sample of interest and can penetrate inside cells and tissue [9]. On the other hand, different to non-invasive techniques based on microscopy, optical tweezers can trap, move, and apply stresses to different kinds of samples.

Optical forces can be described and computed through quantum and electromagnetic theory using a number of analytical and numerical methods [5, 10, 11, 12]. However, computation of the optical forces in experiments is difficult due to the complexity of the microscopic world. The exact optical field at the focus of an optical trap, as well as perfect knowledge of the local parameters defining the light-object momentum exchange, such as the object geometry and refractive index, are strong requirements for accurate calculations [7].

For this reason, indirect, calibration-based approaches to determine the optical trap strength have been thoroughly developed throughout the past forty years. The most common situation of a spherical microbead trapped in a Gaussian beam trap can be linearized such that, for object positions in the vicinity of the trap focus (e.g. within 100 nm), the restoring force behaves as a microscopic, pN-scale spring of the form $F = -\kappa \cdot x$. Provided that some of the features of the surrounding medium are known and controlled (e.g. buffer viscosity, temperature and homogeneity),

trap stiffness (κ, pN/V) calibration can be performed, for instance, from thermal or hydrodynamic analysis.

This has enabled, after trapping cell vesicles *in vivo*, to measure the pulling force exerted by molecular motors, such as kinesin [13]. Flagellar propulsion forces and energy generation have been investigated by optically trapping the head of a bacterium [14, 15]. Cell membranes have been deformed with optical tweezers and the underlying tension determined [9]. And the elastic properties of DNA molecules have been obtained after stretching by use of microspheres bound to the molecular ends [16]. However, the actual characteristics of the experiment often deviate form the simplified model used for calibration. For example, vesicles trapped *in vivo* may deform from the ideal spherical shape or medium inhomogeneity may lead to different trap calibration at different regions of the sample [17, 18].

A different force measurement approach, *a priori* insensitive to local variations in trap calibration, is the direct detection of light momentum changes giving rise to optical forces. Force measurements based on light momentum detection require the caption of all the light interacting with the trapped sample. Their first implementation was introduced S. Smith *et al.* in a counter-propagating set-up [19]. In this set-up, low-NA trapping beams were entirely captured by the corresponding posterior microscope objective. In the more common, single-beam optical tweezers, A. Farré *et al.* demonstrated the use of a high-NA collecting lens to capture light over the whole forward 2π solid angle [20, 21].

Interestingly, one of the main advantages of single-beam optical tweezers is the ability to dynamically control several optical traps by means of modulation techniques [22, 23, 24, 25]. For example, spatial light modulation (SLM) can be used to drive optical trap positioning [26], create arrays of multiple traps to simultaneously manipulate several samples [24], and generate exotic trapping beams to explore novel optical trapping possibilities [27, 28, 29].

Direct trapping and manipulation of specimens, together with quantitative force measurements on irregular samples, is of high interest for optical trapping applications [14, 15, 30, 31, 32]. Usually, several optical traps are needed for stably trapping elongated or extended objects, for which holographic optical tweezers (HOTs) are importantly useful [33, 32, 34]. However, compatibility with light momentum detection needs to be confirmed.

Another important aspect concerning the innocuousness when directly manipulating biological samples with optical tweezers is the increase in temperature due to absorption of the laser light. Accurate knowledge of local temperature is needed for understanding thermally-driven processes, as well as eventual damage to live specimens. Several methods have been introduced to determine laser heating in optical traps [35, 36, 37, 38], although it is generally assumed that, for 1064 nm laser wavelength, the heating rate is around 1 $^{\text{o}}$C at 100-mW laser power [8].

1.1. Objectives

This four-year work aims at the demonstration of light momentum force measurements in complex samples, with especial insight in biological applications. This often requires the use of engineered optical fields with increasing capabilities concerning optical micromanipulation. For example, multiple-trap arrays and complex trapping beams. Here, this will be explored and implemented in a holographic optical tweezers set-up.

Light momentum detection has been reported to operate in a well-defined range of situations [20, 21]. However, experiments with biological samples require certain modifications, such as the use of multiple traps for stable trapping of extended objects (e.g. bacteria), or mounting samples in thicker microchambers (e.g. zebrafish embryos). The possibility to detect light momentum changes will be studied in such situations, which deviate from the ideal performance.

Regarding the applicability into biological samples, the effect of sample heating is a strong concern that questions the non-invasive action of light for optical trapping. One needs to make sure that such heating does not affect the normal functioning of live samples. Moreover, local temperature is important for optical trap calibration. I will tackle this question by introducing a reliable approach for determining local viscosity heating-induced changes.

The goals of my PhD thesis can be summarized as follows:

Holographic optical tweezers set-up The first objective is to settle the experimental set-up for accurate optical micromanipulation experiments. On one hand, generation of the holographic optical traps require control of the laser emission and phase modulation by means of the spatial light modulator (SLM). I will analyze them in detail and focus then on the trap positioning accuracy that is achievable.

On the other hand, it is crucial for the object of this thesis to have a good force reference that I will use for testing and calibration purposes. I will test a piezoelectric stage as a precise drag force generator. Flow velocities will be accurately determined from the stage oscillation performance.

Robustness of light-momentum force measurements I will carry out a deep analysis on the direct force measurement method. Detection of light momentum requires a number of experimental optimizations that ensure the absolute calibration of force measurements, which will be thoroughly studied. The analysis will be complemented with simulations in the far field.

I will also analyze back-scattered light loss. In single-beam optical tweezers, this is the main source of error in light-momentum measurements. My goal is to determine, for a wide range of samples with different properties (e.g. size and refractive index), the validity of the method.

Force measurements on irregular samples   Compatibility of the method in experiments involving complex samples and beams will be studied. With the intention of proving the applicability of light momentum force measurements in arbitrary complex samples, I will make use of holographic trap arrays to trap systems of multiple beads.

Motivated by a wide scope in biological applications, optical trapping and measurements on elongated objects will be technically analyzed by using synthetic rod-shaped samples. For example, there has been increasing interest, within the optical trapping community, to perform studies on chromosomes, elongated bacteria and sperm cells. I will aim at demonstrating the use of holographic trap pairs for stable manipulation of this kind of samples and their precise compatibility with the direct force measurement method.

Determination of heating due to IR light absorption in the optical trap   My approach to determine the effect of laser absorption in optical trapping experiments will consist of using the absolute calibration of light momentum force measurements to detect the decrease in viscosity induced by heating around the trap.

Importantly, I aim to study the variability of this effect depending on the specific properties of the experiment, by performing a large number of tests, for example, on samples of different sizes. The role of the trapping beam numerical aperture and optical trap distance to the microchamber surfaces will be also analyzed. In parallel, heat transport simulations and modeling of the optical trap as a heating source will be performed.

Optical trapping and light-momentum detection in embryonic tissue   The last goal of my thesis is to implement the method inside biological tissue, which constitutes a cutting-edge application of optical tweezers that is envisioned to solve many questions in developmental biology. The trapping beam is strongly affected by tissue-induced scattering, whose effect in measurements will be assessed. As a preliminary check for the possibility to detect light momentum changes in living tissue, I will do trapping experiments in zebrafish embryos.

1.2. Structure

The thesis is structured as follows:

In Chapter 2, I first give a brief introduction into optical trapping theory and modeling and highlight the main technical strategies for quantitative measurements.

In Chapter 3, I analyze in high detail the precision offered by SLM to position the optical traps within subnanometer accuracy [26, 39]. I study the generation

of controlled drag forces by means of a piezo-electric stage and the trapping laser emission properties.

In Chapter 4, I focus on the implementation of the direct force measurement method. Several technical optimization steps need to be carried out for the light creating high-NA, single-beam optical tweezers to be entirely captured for momentum measurements.

In Chapter 5, measurement of forces through light momentum detection is performed on irregular samples manipulated with HOTs. I use this scheme to measure the collective force on a system composed of multiple spherical particles, as well as rod-shaped samples of different sizes. The use of holographically modulated exotic beams is as well explored.

In Chapter 6, I apply the same force detection method to determine laser-induced heating in several experimental situations. I describe in detail the experimental routine to assess the heating effect, as well as the simulation approach to analyze this phenomenon.

Finally, in Chapter 7, I describe the manipulation and measurements inside embryonic tissue. I show how the laser beam is affected by the scattering structures present in live zebrafish embryos and discuss their effect on force measurements.

2. Micromanipulation and force measurements with optical tweezers

Radiation pressure was firstly observed to accelerate dielectric, micron-sized particles in a laboratory by A. Ashkin in 1970 [4]. Using a weakly focused laser beam, he observed two contributions to the optical force: one accelerating particles downstream (*scattering force*), and another one attracting particles into higher beam intensity regions (*gradient force*). Importantly, he described the necessity that the particle be of refractive index higher than that of the surrounding medium ($n_p > n_m$), otherwise there was no attracting, but repulsive force. By means of two counter-propagating beams, scattering forces were balanced so that particles with high n_p could get stably trapped.

In 1986, A. Ashkin and co-workers pioneered the construction of a single-beam optical trap and demonstrated the stable trapping of particles ranging from 25 nm to 10 μm [5]. Basically, it was observed that focusing the laser beam through a sufficiently high-NA objective produced an axial intensity gradient capable of counteracting the downstream, scattering force. Regarding the technical point of view, this is a much simpler scheme that has been largely exploited in optical micromanipulation and has been complemented with other techniques, such as dynamic optical tweezers by the use of wavefront modulation or acousto-optic deflectors [7].

In the following chapter, we briefly present the optical trapping technique and introduce the main theoretical approaches describing the optical forces governing an optical trap. Some indirect trap calibration methods for experimental, quantitative force measurements are then reviewed. The direct force measurement method, which is based on the determination of light momentum changes arising form an optical force, as will be analyzed in depth in this thesis, is explained in detail.

2.1. Optical force

A single-beam optical trap is illustrated in Fig. 2.1a. When focused through a high-NA objective, the trapped particle produces changes in light momentum that result in optical forces that point to the trap focus. The use of high-NA objectives

is needed to produce gradient forces higher than scattering forces, i.e. for stable trapping.

A number of theoretical approaches have been developed to describe the optical force either analytically or numerically. Optical trapping is often distinguished into two regimes: the Rayleigh approach, which describes optical forces for particles much smaller than the trapping wavelength ($D \ll \lambda$), and the ray optics approach, which is applicable to larger particles ($D \gg \lambda$).
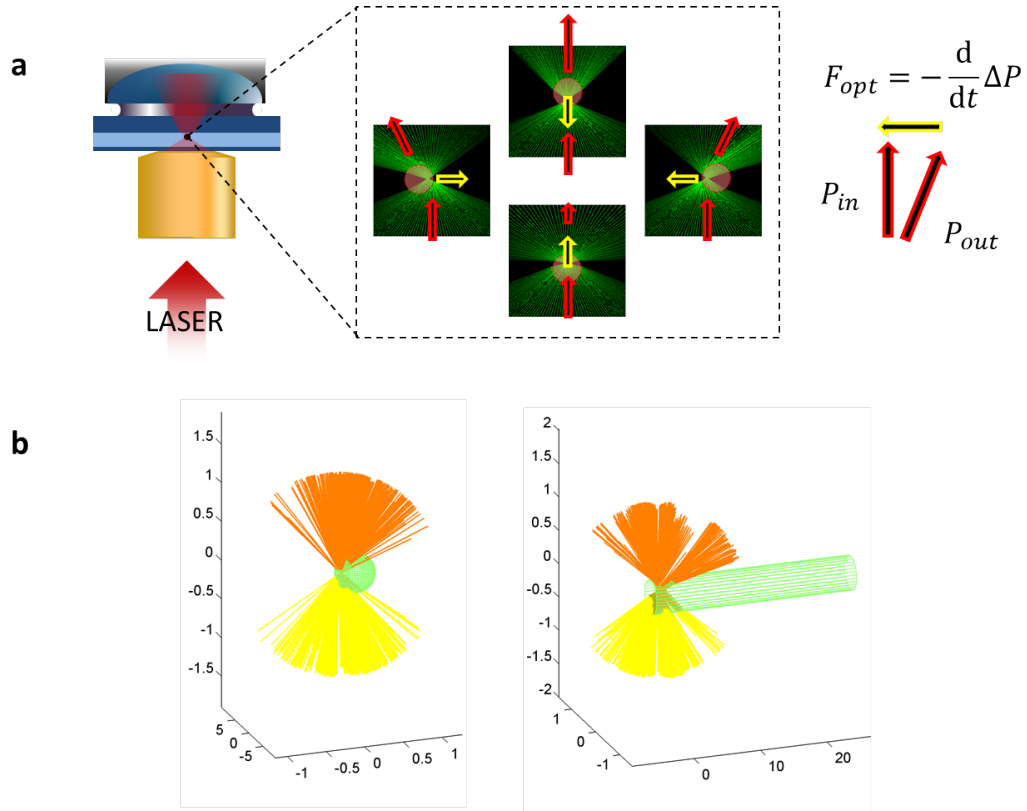
Figure 2.1.: Single-beam optical tweezers. (**a**) Light momentum changes of the trapping beam result in forces that attract the trapped particle towards the trap focus. (**b**) Ray-optics sketches using the Optical Trapping in Geometrical Optics toolbox [40].

Under the Rayleigh regime, or dipole approximation, Y. Harada and T. Asakura found the following gradient and scattering forces [10]:

$$\overrightarrow{F_g} = 2\pi \frac{n_m}{c} a^3 \frac{n_{rel}^2 - 1}{n_{rel}^2 + 2} \vec{\nabla} I\left(x, y, z\right) \tag{2.1a}$$

$$\overrightarrow{F_s} = \frac{n_m}{c} \frac{8}{3} \pi k^4 a^6 \left(\frac{n_{rel}^2 - 1}{n_{rel}^2 + 2}\right)^2 I\left(x, y, z\right) \hat{z} \tag{2.1b}$$

where n_m is the medium refractive index, $n_{rel} = n_p/n_m$ is the relative refractive index of the particle, a is the radius of the particle and $k = 2\pi/\lambda$ (λ is the trapping laser wavelength). We can be observed that, while the scattering force, $\overrightarrow{F}_s$, points the beam propagation direction (indicated by the unit vector $\hat{z}$) and is proportional to the laser intensity, the gradient force, $\overrightarrow{F}_g$, points towards the intensity gradient, $\vec{\nabla}I(x, y, z)$, i.e. towards higher intensity regions.

For large particles compared to the trapping wavelength, ray optics provides precise calculation of the momentum exchanged with the trapping beam that give rise to optical forces. A recent software has been released by A. Callegari *et al.* [40] that is based on this approach and applies for spherical particles, as well s cylinders and ellipsoids (see. Fig. 2.1b). Each ray composing the trapping beam undergoes a change in momentum that results in the following force, $\overrightarrow{F}_{ray}$, exerted onto the particle:

$$\overrightarrow{F}_{ray} = \frac{n_m P_i}{c}\hat{u}_i - \frac{n_m P_r^{(1)}}{c}\hat{u}_r^{(1)} - \sum_{j=2}^{\infty} \frac{n_m P_t^{(j)}}{c}\hat{u}_t^{(j)} \tag{2.2}$$

Here, n_m is again the refractive index of the medium. P_i and $P_r^{(1)}$ are the powers of the incident ray and the first reflected ray, respectively. $P_t^{(j)}$ are the powers of the rays transmitted out the particle after the jth scattering event. $\hat{u}_i$, $\hat{u}_r^{(1)}$ and $\hat{u}_t^{(j)}$ are unit vectors pointing the direction of each ray. Usually, computing up to $j = 10$ suffices for precise calculation of the optical force. At every scattering event, reflection and refraction angles and relative powers for the subsequent rays are calculated through Snell and Fresnel laws [40].

The more general approach to calculate optical forces consists in computationally solving the electromagnetic equations to obtain the momentum exchange by integration of the Maxwell stress tensor (MST) [11, 41]. The optical fields can be obtained from finite-difference time-domain (FDTD) simulations, from which the optical force is calculated as follows [42]:

$$\overrightarrow{F} = \int_S \overleftrightarrow{T} \cdot \mathrm{d}\overrightarrow{S} - \epsilon\mu\frac{\mathrm{d}}{\mathrm{d}t}\int_V \overrightarrow{U}\,\mathrm{d}V \tag{2.3a}$$

$$T_{ij} = \epsilon E_i E_j + \mu H_i H_j - \frac{1}{2}\left(\epsilon\,|E|^2 + \mu\,|H|^2\right)\delta_{ij} \tag{2.3b}$$

where $\overleftrightarrow{T}$ is the MST, V and S are the volume and surface surrounding the trapped particle and $\mathrm{d}\overrightarrow{S}$ is the surface element pointing outwards. ϵ and μ are the permittivity and permeability of the medium, respectively. In principle, this approach is applicable to arbitrary geometries, but computation time increases considerably.

In the far field, integration of MST over an spherical surface enclosing the sample reduces to integration of the Poynting vector, i.e. the plane wave angular spectrum [42]. Force is thereby obtained by directly computing the change in light momentum:

$$F_{\mathrm{x}} = \frac{n_m}{c} \oint [I_0(\Omega) - I(\Omega)] \sin\theta \cos\phi \, \mathrm{d}\Omega \tag{2.4a}$$

$$F_y = \frac{n_m}{c} \oint [I_0(\Omega) - I(\Omega)] \sin\theta \sin\phi \, \mathrm{d}\Omega \tag{2.4b}$$

$$F_z = \frac{n_m}{c} \oint [I_0(\Omega) - I(\Omega)] \cos\theta \, \mathrm{d}\Omega \tag{2.4c}$$

Here, $\mathrm{d}\Omega$ is the solid angle element and θ and ϕ are the spherical coordinates, respectively. $I(\Omega)$ and $I_0(\Omega)$ are the light intensity distributions in the far field with and without the particle scattering the beam [11]. We used the Optical Tweezers package from Lumerical's FDTD Solutions to solve Maxwell equations and calculate forces by integrating the Poynting vector in de far field. In Fig. 2.2, the presence of a microsphere in the trap focus is observed to deflect the beam, which gives rise to an optical restoring force.
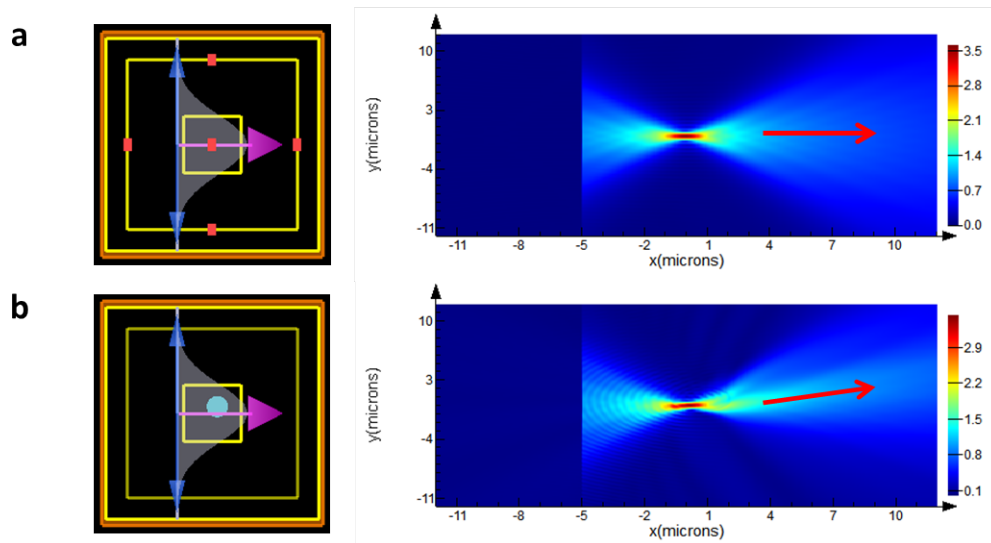
Figure 2.2.: FDTD simulations using Lumerical software. (**a**) Layout of a freely propagating beam. (**b**) When a spherical bead is places at the trap focus, slightly displaced laterally, the trapping beam is deflected.

A fast computational strategy for obtaining trapping forces consists in decomposing the far field into a base of functions. This enables to define a scattering matrix, so-called T-matrix, that describes particle-induced scattering [12, 43, 44].

2.1.1. Comparison example

The complete force profile for an NA = 1.2 trapping beam, obtained from FDTD simulations, is shown in Fig. 2.3. Importantly, it accurately fits the force profile obtained in the ray optics regime by means of the Optical Trapping in Geometrical Optics (OTGO) [40] toolbox, according to the bead diameter, $D = 3.00\,\mu$m, being much larger than the wavelength ($\lambda = 1064\,$nm). It is worth commenting on the fact that the force is not perfectly described around the particle surface, i.e. $x_{trap} \sim {}^{D}/_{2}$ [44]. We additionally compared the force profile, for a trapping beam with a beam waist of $\omega_0 = 0.4\,\mu$m, with that obtained from the T-matrix method, by use of the Optical Tweezers Toolbox 1.3 (OTT) [12].
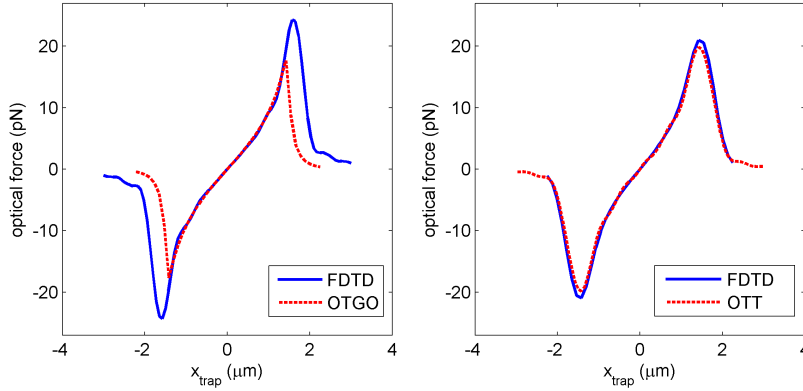
Figure 2.3.: (**a**) Force profile for an NA = 1.2 trapping beam simulated in FDTD (solid line) and OTGO (dashed line). (**b**) Force profile for a $\omega_0 = 0.4\,\mu$m simulated in FDTD (solid line) and OTT (dashed line).

Among the several approaches introduced, we will use the Poynting integration in the far field to compute trapping forces. Calculation of forces from light momentum changes reproduces the technical functioning of the direct force measurement method and provides useful insight on the effects arisen from different experimental situations. For example, FDTD will shed light into the effect of back-scattered light loss in force measurements, as well as non-uniform transmittance of the force detection set-up.

2.2. Indirect force measurements

Usually, force measurement strategies in optical tweezers consist in two steps. Calibration of the optical trap connects a magnitude accessible from experiments with the optical force. First, a method to determine such calibration is carried out. Second, measurement of the so-called *primary variable* yields thereby force readings.

The sample position and the minimal trapping power to counter-balance escape forces are the two main paths for obtaining calibration-based force measurements. The sample position relates to force through the linear optical spring approach, which is valid for small displacements with respect to the focus of the trap:

$$F = -\kappa\, x \tag{2.5}$$

The trap stiffness, κ (pN/μm), can be obtained through a number of methods. In general, they can be classified into two groups, depending on the forces that are used for calibration [45]. Thermal calibration employs the spontaneous fluctuations, with no external force, yielding Brownian motion of the trapped sample. The equipartition theorem and the power spectrum methods are based on this analysis. On the other hand, a known, external force, can be applied to the sample while its position is recorded, allowing for the drag force method, which uses Stokes-drag forces induced, for instance, with a piezo-electric stage.

On the other hand, the minimal trapping power necessary for keeping a sample trapped can as well provide quantitative force measurements. Optical force scales linearly with the trapping laser power:

$$F = \frac{n\,Q}{c}\, P \tag{2.6}$$

Here, F is the optical force, n is the refractive index, c is the speed of light and P is the trapping power. The dimensionless parameter Q is the so-called trapping efficiency. One first needs to determine, for a known force value, e.g. from Stokes drag, the minimal power for trapping. Force measurements therefore lie in trapping the sample at decreasing powers until it escapes from the trap.

Such indirect approaches necessitate that the calibration procedure be performed on the same probe eventually trapped for measurements, i.e. *in situ*. If a new sample is trapped, a new calibration must be carried out, due to the calibration being strongly dependent on a number of experimental parameters. Moreover, theoretical descriptions of thermal or hydrodynamic forces are required for determining the force reference for calibration, which limits the existence of calibration-based strategies, for example, within spheres and cylinders or samples that can be modeled this way.

2.2.1. Position measurements

Position measurements in optical tweezers are commonly carried out in two ways. Standard back focal plane (BFP) interferometry uses light scattered by the trapped sample to detect 1-nm scale displacements at hundreds of kHz, by means of a quadrant photo-diode (QPD) or a position-sensing detector (PSD). Differently, tracking algorithms combined with fast cameras enable parallel position measurements on multiple spots with a speed on the order of 1 kHz.

If sample positions are to be measured for trap calibration purposes, it is worth that the acquisition rate be fast enough in order to monitor thermal motion, especially i thermal-based calibration strategies. We are here describing the main features of both approaches.

2.2.1.1. Video tracking

In Ref. [46], G. Gibson *et al.* describe the use of fast, 1-kHz CMOS cameras for calibrating optical traps through the analysis of the Brownian motion. They show the possibility to record histograms for equipartition theorem calibration, as well as power spectrum up to the thermal limit. Moreover, they show the possibility determine the cross-correlated motion of two beads. A similar approach was applied by A. Huhle *et al.* in a magnetic tweezers set-up [47]. In this case, 3D tracking of several particles was demonstrated at kHz rates with sub-nanometer accuracy, which enabled measurement of DNA stretching steps of 5 Å.

F. Marsà *et al.* similarly used a high-speed camera to detect the parallel drift motion in a dumbell trap configuration [48]. Sub-nanometer tracking in this configuration will enable measurements of trap positioning accuracy, as we will show in Chapter 3.

Video tracking can as well be applied to position and orientation measurements on non-spherical samples. In Ref. [33, 32], D.B Phillips *et al.* apply high-speed video imaging to calibrate holographically-trapped micro-rods and probes with complex shape for scanning force microscopy. In Chapter 5 of this thesis, we will use video images for determining the motion of trapped micro-cylinders to determine their trapping force profiles.

2.2.1.2. Back focal plane interferometry

Light scattering by an optically-trapped sample is sensitive to the relative position with respect to the trap focus. Interestingly, beam deflections can be tracked with a QPD or a PSD and, after calibration, be connected to sample displacements in 3D. A review of the main steps that made this a unique technique thanks to subnanometer displacement accuracy and high-rate bandwidth was published by I. Verdeny *et al.* [45]. An interferometric theoretical description of scattering by a particle in the Rayleigh regime was done by F. Gittes and C. Schmidt to find the position sensing profile of a trapped particle [49]. Usually, a high-NA collecting lens or a microscope objective is used to capture part of the light emerging from the optical traps to implement BFP interferometry. In Ref. [50], some experimental features for an optimized detection sensitivity are discussed.

In principle, BFP interferometry is applicable in single optical traps, due to light creating multiple traps will be mixed in the detector after scattering. Solutions for this can be found in dual trap systems with crossed polarizations (dumbbell

configuration) [48] and using a pinhole at a plane optically equivalent to the trapping plane to select for the trap of interest [51].

BFP interferometry can be rapidly calibrated by the use of acousto-optic deflectors (AODs) [52]. Importantly, the use of an additional laser beam for detecting sample displacement, has been lately implemented independent of the trapping beam for rheological studies in zebrafish embryos [53]. Recently, some modification of the detection set-up have been shown to improve the displacement resolution [54, 55] and aberration effects in the optical traps [56].

In this thesis, we use an optimized version of BFP interferometry that constitutes the direct force measurement method in optical tweezers [20, 21], as discussed in Section 2.3.

2.2.2. Thermal forces

Thermal fluctuations can be analyzed in different ways for calibrating the stiffness of an optical trap. We here review the two methods more used in optical trapping laboratories.

Equipartition theorem   From the linear spring assumption for an optical trap, spontaneous thermal fluctuations can be applied the equipartition theorem to obtain the trapping stiffness as follows [7]:

$$\frac{1}{2}k_B T = \frac{1}{2}\kappa \left\langle x^2 \right\rangle \tag{2.7}$$

where k_B is Boltzmann's constant and $\left\langle x^2 \right\rangle$ is the variance of the sample position. Under this approach, no knowledge of the sample properties is *a priori* a need but we only need to know the local temperature, T. For example, medium viscosity or sample geometry is not a requirement. On the other hand, one does need to calibrate the position detection performance (e.g. through BFP interferometry if no high-rade video recording is available).

Concerning irregular samples, this method can be generalized to include higher degrees of freedom to calibrate the stiffness matrix of micro-rods [33] and rod-like shape bacteria [57].

Power Spectrum   When parameters describing the experiments are known, such as the particle radius and the medium viscosity, Lagevin's equation can be used to model thermal fluctuations. This method is particularly useful for standard calibration using BFP-interferometry set-ups, for which sample positions are measured as $x = \beta \, S_x$. In a viscous medium, such as water or glycerol, the power spectrum of

the Brownian thermal motion damped by a linear optical trap becomes a Lorentzian that can be fitted as follows:

$$P(f) = \frac{1}{T_{msr}} |\tilde{x}(f)|^2 = \frac{a}{1 + \frac{f^2}{f_c^2}} \tag{2.8}$$

Here, T_{msr} is the time length of the measurement, f is frequency coordinate and $\tilde{x}$ is the Fourier transform of the trapped particle position. From the corner frequency, f_c, and the lorentzian amplitude, a, we can easily obtain the sensor responsivity (β, µm/V) and the trapping stiffness (κ, pN/µm):

$$\kappa = 12\pi^2 \eta R f_c \tag{2.9a}$$

$$\beta = \sqrt{\frac{k_B T}{12\pi^3 f_c^2 \eta R a}} \tag{2.9b}$$

A thorough implementation software for this calibration method, that accounts for further corrections to the power spectrum (such as aliasing due to digital acquisition and surface hydrodynamic correction) was published by I. M. Tolic-Nørrelykke *et al.* [58] in Matlab. Under this scheme, forces are eventually obtained as $F = \kappa x = \kappa \beta x$, from which we can obtain a direct connection from the sensor voltage signals with the applied forces:

$$\alpha_{trap} = \kappa \cdot \beta \tag{2.10}$$

As will be discussed in the Section 2.3, this parameter becomes in principle invariant in the direct force measurement method. Chapter 4 focuses thereby on using this, together with α_{trap} Stokes calibration int he next section, to analyze this property.

2.2.3. Drag forces

The drag force that a fluid exerts on a spherical particle at low Reynolds number is described by the following equation [7]:

$$F_{drag} = 6\pi \eta R b\, v_{flow} \tag{2.11a}$$

$$b = \frac{1}{1 - \frac{9R}{16h} + \left(\frac{R}{2h}\right)^3} \tag{2.11b}$$

where η is the fluid viscosity, R is the particle radius, v_{flow} is the fluid velocity and h is the distance to the surface. Factor b is Faxén's coefficient correcting for the sphere-to-surface interaction.

Stokes-drag forces can be used for trap calibration in two ways [8]. In the position-based calibration approach, a known force is applied to the sample whilst its displacement is recorded to obtain the trapping stiffness, κ. In the escape-force-based strategy [59], the force at which a trapped sample escapes the trap at a given trapping power is known through equation 2.11 and can be similarly expressed as:

$$F_{esc} = \frac{n\,Q_{esc}}{c}\,P \tag{2.12}$$

Following Eq. 2.12Force measurements are eventually carried out by monitoring the minimal power keeping the sample trapped, which scales linearly with respect to the former power value.

In BFP-interferometry-like set-ups, a factor directly relating force values (pN) to sensor responses (V), i.e. α_{trap} (pN/V), is obtained as follows:

$$\alpha_{trap} = \frac{6\pi\eta R b\,v_{flow}}{\langle S_x \rangle} \tag{2.13}$$

Here, $\langle S_x \rangle$ is the average voltage signal while a constant flow is applied. This scheme will be carried out in Chapter 4 for testing the accuracy of the direct force measurement method on different samples.

The Stokes-drag approach can be applied as long as theoretical description of hydrodynamics is available. For example, the head of an *E. Coli* bacterium has been modeled as an ellipsoid for propulsion force measurement [15], and chromosomes have been represented as slender cylinder for motility measurements within the mitotic spindle [30].

2.3. Direct force measurement method

Light-particle interaction in an optical trap gives rise to forces that confine the trapped particle at the beam focus and, from the perspective of Newton third law, to beam momentum changes. Detection of such light momentum changes leads to direct measurement of optical trapping forces. The term *direct* expresses the fact that force is measured *itself*, instead of being inferred from a primary variable, such as particle position or laser power, that connects to force. As discussed in the previous section, relating another variable to force makes it necessary to accurately know the microscopic details of the experiment (e.g. viscosity, temperature, particle geometry) and the specific dynamics that govern optical forces and forces used for calibration (e.g. $F = -\kappa\,x$ linearity and drag coefficient γ).

These promising advantages necessarily come at the cost of a complex optical design, since it should be capable of collecting all the light interacting with the sample. If not so, the momentum information transferred to missing photons would eventually

produce errors in force measurements. Proper detection of light momentum requires the beam first be captured and, further, be conveyed to sensors accordingly assessing the beam momentum structure.

A first strategy, proposed by Smith *et al.* in 2003, was applied in counter-propagating optical traps [19]. In this system, two 1.2-NA objectives facing one another focus each low-NA beams at the same point, thus creating a stable optical trap. Underfilling the trapping objectives ensures the collection of most part of the light trapping the samples, since large beam deflections due to applying external forces can still be captured. Concerns on total light collection have led to using this approach by several laboratories [19, 60, 61, 7].

As has been discussed, single-beam optical tweezers offer important advantages with respect to counter-propagating optical traps, such as a simpler design strategy through a commercial inverted microscope and compatibility with wavefront modulation for dynamic trapping. Farré *et al.* described the technical conditions that ensured high-NA beams needed for creating stable optical tweezers (gradient forces must counterbalance scattering forces) to still be completely collected and their momentum measured [20].

Light emerging from such high-NA trapping beams after interacting with the trapped samples primarily travels towards the positive direction, as will be analyzed in Chapter 4, but one needs to make sure that light comprised in the forward 2π solid angle is wholly captured. This is achieved by means of an oil-immersion collecting lens with NA higher than the medium refractive index, i.e. $NA > n_m$, for which rays traveling at $\theta \rightarrow 90^{\text{o}}$ still enter the momentum detection optical system.

The second condition is that such collecting lens needs to accurately fulfill the Abbe sine condition, meaning that rays traveling at angle θ focus at $x = f'n\sin\theta$ at its back focal plane (BFP). Here, f' and n are the focal length of the lens and the refractive index of the immersion oil. In other words, it is a need that the principal surface of the lens be perfectly spherical. Under this assumption, a photon with lateral momentum $p_x = \hbar k \sin\theta = \frac{h}{\lambda_0} n \sin\theta$ (where h is Planck's constant and λ_0 is the trapping laser wavelength in vacuum) will focus at x.

The detection system is technically similar to that of a usual BFP interferometry (see section 2.2.1.2), but needs to be optimized to accomplish these conditions [21, 62]. The entirely captured beam is finally shined onto a position-sensing detector (PSD) appropriately placed at a plane optically equivalent to the BFP. This sensor yields positional and sum signals as follows, where γ is the sensor responsivity and R_{D} its radius:

$$S_{\mathrm{x}} = \frac{\psi}{R_D} \iint\limits_{PSD} xI\left(x,y\right)\,\mathrm{d}x\mathrm{d}y \tag{2.14a}$$

$$S_{\mathrm{SUM}} = \psi \iint\limits_{PSD} I\left(x,y\right)\,\mathrm{d}x\mathrm{d}y \tag{2.14b}$$

Using the aforementioned relations for x and p_x and that the energy of a single photon is $E = h\nu = h\frac{c}{\lambda_0}$, we obtain a direct reading of the total X component of the beam momentum, and hence the optical force, from S_{x} (similar for the Y component):

$$S_x = \frac{\psi f'c}{R_D} \iint\limits_{PSD} p_x\left(x,y\right)\frac{I\left(x,y\right)}{h\nu}\,\mathrm{d}x\mathrm{d}y \equiv \frac{1}{\alpha}F_x \tag{2.15}$$

Providing that light is chiefly scattered forward, expression 2.15 is the experimental equivalence to the momentum flux in Eqs. 2.4 for the lateral cases (X and Y). In turn, the S_{SUM} signal corresponds to the optical trap power by $S_{\mathrm{SUM}} = \psi P_{\mathrm{trap}}$. Again, such equivalence will be thoroughly assessed in Chapter 4.

Note that the optical force, $F_x = \alpha S_x$, is obtained from the direct reading of the sensor and that α is uniquely determined by the parameters of the optical detection set-up: ψ, f', R_D. In other words, this constitutes a macroscopic calibration insensitive to local, microscopic features of the optical trap, trapped specimen or medium.

The light capture performance is sketched in Fig. 2.4. Similar to a Ronchi ruling experiment, in Fig. 2.4(a) we used the SLM to display a circular pattern by alternating zero- and π-phase (see Chapter3). The pattern was visible at the PSD plane by means of a CCD. As will be shown in Chapter 4, the impact position of rays exiting the trap with angle θ is $f'n\sin\theta$ 2.4(b), according to the Abbe sine condition . Finally, a bead was placed at the trap focus to scatter light and rays exiting at $\theta \to 90^{\mathrm{o}}$ were observed to reach $f'n\sin\theta \sim f'n_m$.

The same principle can be applied to measure axial optical forces after some modification of the detection performance. Thalhammer *et al.* substituted the PSD at the BFP with a high-speed camera to digitally compute the three components of the beam momentum [63]. Similar to Eqs. 2.14, expressions defining the momentum flux in 3D (see Eqs. 2.4) can be reduced into integrals in the BFP. Combined with phase detection, this approach will eventually lead to complete determination of the forward-scattered field, providing information on higher-order momenta, such as torque. A different scheme was devised by Smith *et al.* to achieve beam power concentration measurements [64]. This briefly consists in using a mask with a circular transmittance profile, after which the S_{SUM} signal of the PSD is equivalent to F_{z}.
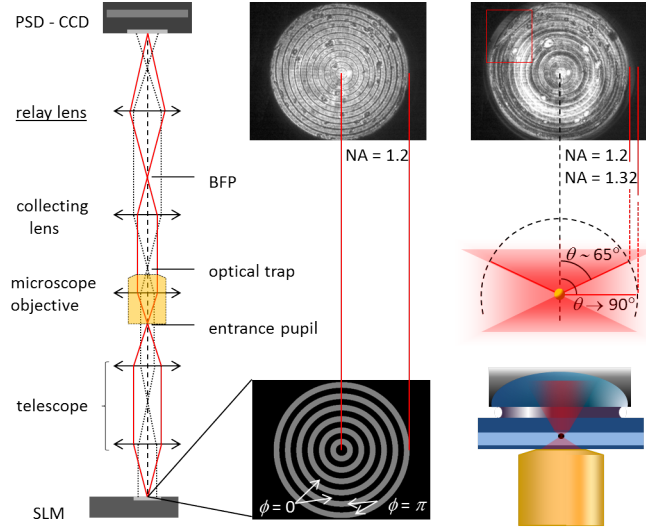
Figure 2.4.: Collecting the forward 2π solid angle. (a) A circular-grating hologram is displayed at the SLM, which is conjugated at the entrance pupil of the microscope objective (water-immersion, NA = 1.2), which is in turn conjugated at the BFP of the collecting lens. (b) A CCD camera substituting the PSD at a plane conjugate to the BFP records the BFP pattern obtained. (c) The same pattern recorded with a bead scattering light from the trap. Rays with NA = 1.32, which correspond to angle $\theta \rightarrow 90^{\text{o}}$ are still captured.

Beam momentum detection for force measurements has been applied in an increasing number of optical trapping laboratories. As has been mentioned, direct detection of force unbinds experiments to trap calibration prior to force measurements, which is difficult, if not impossible, when working in inhomogeneous buffers and non-spherical samples. J. Mas *et al.* measured stall forces in living cells and validated the momentum detection with active-passive calibration [65, 66]. Y. Jun *et al.* similarly explored the possibility to measure force *in vivo* with no need of *in situ* trap calibration [67]. M. Taylor *et al.* used the direct force measurement method to determine the trapping force profile in optimized, non-Gaussian traps [68].

In this thesis, beam momentum detection has been proven accurate to measure forces on microcylidners optically-trapped in pairs of holographic tweezers [69], and the invariant momentum calibration has been used to measure local trap temperature [70]. Recently, R. Meissner *et al.* similarly measured drag forces on microrods [71]. Examples of measurements on arbitrarily shaped particles using the absolute calibration of light momentum detection can be found in the work by A. Bui *et al.* [72].

Indirect calibration-based force measurements require high control of variables and physics governing the trapping process. The linear relationship $F = \kappa x$ is accurately assumable for the case of spherical particles in Gaussian traps, but cannot be taken for granted in more complex situations. In fact, even when trapping microspheres,

one needs to make sure that their position with respect to the trap remains within the linear response region, i.e. forces cannot be measured up to the escape force.

Knowledge of local variables is demanding in most applications and almost out of reach *in vivo*, importantly limiting accurate force measurements for biological applications. Local temperature, viscoelasticity and trapped particle geometry are crucial in nearly all the calibration schemes, which require precise thermal and/or hydrodynamic description. Trapping beam structure (i.e. NA or waist, power, relative refractive index or parameters as for non-Gaussian beams) strongly affects optical force, hence urging a new calibration if any of these parameters changes. Moreover, fulfilment of the fluctuation-dissipation theorem is of the utmost importance for thermal calibration, which is not straightforward under drift and *in vivo* conditions.

The invariant charactersitic of $F = \alpha S$ robustly overcomes the difficulties or inexistence for trap calibration. Results from several laboratories and conclusions of this thesis let us envisage that light momentum measurements in single-beam optical tweezers will trigger more precise experiments in optical trapping. For example, direct trapping and measurement on biological samples, such as microorganisms, chromosomes, cell membranes or actin bundles, will be possible with no need of auxiliary calibrated microbeads and the intricate force calibration strategies depicted in section 2.2.

3. Holographic optical tweezers

As introduced in the previous chapter, the manipulation versatility of optical tweezers becomes highly increased if a dynamic driving scheme is incorporated in the set-up. Several examples, such as scanning mirrors and acousto-optic or electro-optic deflectors, offer precise trap positioning and fast, time-sharing capabilities [7].

Among these, holographic optical tweezers (HOTs) [73, 74] offer useful and novel capabilities derived from beam shape engineering: creation of multiple optical traps in 3D [24], aberration compensation [75] and generation of exotic light beams, among others [76, 27, 29].

In the following chapter, the main features for the design of a holographic optical tweezers set-up based on an inverted microscope are analyzed. First, we briefly describe the optics to properly manipulate a laser beam to create a stable HOT. We then focus on the functioning of some of the devices used. We assess the effect of polarization instability of the fiber laser, as well as its high-frequency noise. The phase modulation performance of the SLM is accessed by use of a simple ellipsometric approach. In addition, the piezo-stage further used for accurate drag force measurements is calibrated to correct for its driving electronics transfer function.

Second, the manipulation flexibility of HOTs is shown. We first use a dumbbell configuration to split the laser beam into one modulated and one non-modulated orthogonally-polarized components [48]. This configuration enables accurate removal of slow drift noise, and sub-nanometer accuracy in single-trap positioning is demonstrated through precise video tracking. Positioning deviations due to phase quantization and plane pixelation are determined and corrections for hologram computation are presented. Generation of multiple-trap arrays is as well schemed, which will be eventually used for manipulation of multiple-bead systems and extended objects in Chapter 5. Finally, we show the modulation performance for exotic beam shaping, e.g. to create cogwheel beam traps [27].

3.1. Optical tweezers set-up

The holographic optical tweezers set-up used in our experiments is presented in Fig. 3.1. The laser (IPG YLM-5-1064-LP) emits a continuous, linearly polarized Gaussian beam TEM_{00} up to 5 W at a wavelength of $\lambda = 1064\,\text{nm}$, with a nominal beam diameter of 5.1 mm. A combination of a half wave-plate (HWP 1) and a polarizing beam splitter (BS) facilitates power control by polarization.
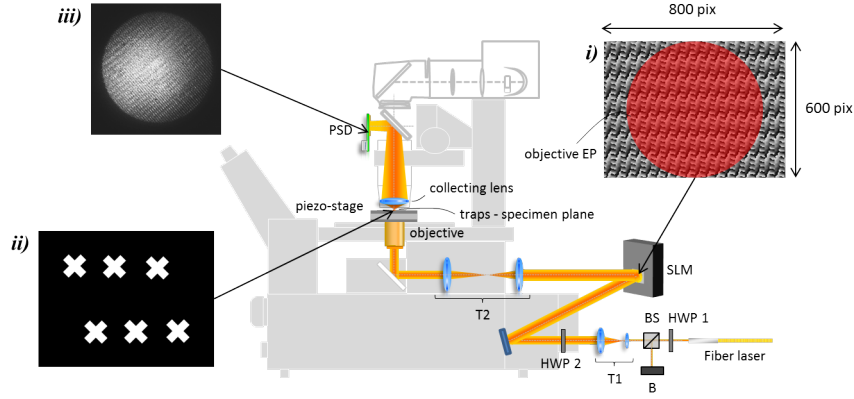
Figure 3.1.: Holographic optical tweezers set-up. (**i**) A typical phase hologram displayed at the SLM. (**ii**) Scheme of the multiple-trap array generated at the sample plane. (**iii**) BFP image of the trapping beam. HWP: half-wave plate; B: beam block; BS: beam splitter.

Telescope 1 (T1, $f_1 = 30$ mm, $f_2 = 100$ mm) widens the beam to overfill the SLM active area. We use a liquid crystal on silicon, parallel nematic reflective SLM (Hamamatsu X10468-03: 800x600 pixels, $p = 20$ μm pixel sized, 8-bit DVI signals). Before the SLM, another half-wave plate rotates the polarization to control the relative power of the phase-only modulated beam (horizontal polarization) with respect to the non-modulated beam (vertical polarization).

The beam enters a commercial, inverted microscope (Nikon Eclipse TE2000-U) through the rear port and is reflected up by a dichroic mirror. Telescope 2 (T2, $f_3 = 150$ mm, $f_4 = 100$ mm) conjugates the SLM plane at the back focal plane of the microscope objective in a 4f-configuration with a magnification f_3/f_4 [25], such that the 600 active pixels of the SLM (12 mm wide) exactly fit in the entrance pupil of the objective, with a diameter $\Phi_{EP} = 2\,\mathrm{NA}\,f = 8\,\mathrm{mm}$ (See Fig. 3.1i). We typically use a water immersion microscope objective (Nikon Plan Apo, 60x, NA=1.2) to focus the laser light into the specimen to create the optical trap (Fig. 3.1ii). It is an infinity corrected objective with a lens tube of focal length $f_{tube} = 200\,\mathrm{mm}$, therefore with a focal length $f = f_{tube}/60 = 3.33\,\mathrm{mm}$. This objective allows for compensating the aberration introduced by the microscope coverslip by means of a correction collar and enables creating the optical traps up to 280 μm in depth (working distance).

For typical optical microscopy applications, a condenser illuminates the sample from above, and its bright field image through the objective is registered by a conventional CCD camera (QICAM 12-bit Qimaging, 1392x1040 pixels, 4.65 μm pixel sized, 24 Hz) at a different port of the microscope. In force measurement experiments, the condenser is substituted by a direct force detection instrument (Impetux Optics, Lunam T-40i), which as well permits illumination of the sample plane, while collecting the laser beam emerging from the optical traps through an oil-immersion NA = 1.4

lens, as disscussed in Section 2.3. As will be thoroughly described in Chapter 4, the back focal plane (BFP) of the collecting lens is imaged at a position-sensing detector (PSD) for force measurements. This sensor yields positional signals, S_X and S_Y, related to trapping forces as $F_{X,Y} = \alpha S_{X,Y}$; and sum signals, S_{SUM}, related to trap powers as $P = 1/\psi S_{SUM}$ (see Eqs. 2.14). Similarly, the PSD can be substituted by a CCD camera (UEye, specs) to analyze the beam intensity distribution (Fig. 3.1iii).

Microchambers containing different kinds of samples are typically prepared by gluing a thin coverslip and a microscope slide. The coverslip (usually Deltalab or Menzel nr. 1, approximately 150 μm thick) faces the objective, while the microscope slide (Deltalab, 1 mm thick) is in contact with the immersion oil in force detection experiments. As spacers, we habitually use 90-μm double-scotch tape, in which an approximately 1x1cm cavity has been drawn out. When thicker microchambers are needed, i.e. in the experiments with embryos in Chapter 7, the upper thick slide is replaced by another thin coverslip and 3-5 tapes are carefully stacked for spacing. In this way, the collecting lens working plane can be located deeper in the chamber. Samples (polystyrene, melamine resin or silica microbeads, or glass microrods) are diluted in water, glycerol or sucrose solutions to a sufficiently low concentration to avoid unexpected trapping. Particular details on experiments will be given in the following chapters.

A piezoelectric platform (Piezosystem Jena, TRITOR 102 SG) is used, at the microscope stage, to induce precise drag forces on the optically-trapped particles. A National Instruments NI-DAQ interface enables driving and monitoring of the platform through LabView software. To prevent microchambers from sliding, they were fixed with tapes onto the piezoelectric platform.

3.1.1. Laser characterization

The combination of a half-wave plate (HWP) and a polarizing beam splitter allows for running the fiber laser at a relatively high power to improve stability. See in Fig. 3.2a the positional power spectrum recorded with the PSD through signal S_X at 15 kHz for an empty trap. High frequency peaks around 1-10 kHz are shifted out of the spectrum as the laser output power, P_{output}, is increased from 0.1 W to 2 W, while the trap power is set at $P_{trap} = 10$mW by properly rotating HWP 1 (see Fig. 3.1).

In Fig. 3.2b, two 1.16-μm beads are captured in traps with the same power values. The power spectrum becomes a typical lorentzian curve, arising from the harmonic potential introduced by the optical trap (see Section 2.2). Note that a high P_{output} is necessary for eliminating noise peaks that would eventually affect trap stiffness calibration.

On the other hand, using a polarizing beam splitter (BS) to control laser power makes evident that the output beam polarization oscillates in a long-range timescale, of around 1 min. As provided by the manufacturer, the laser source is a TEM_{00}
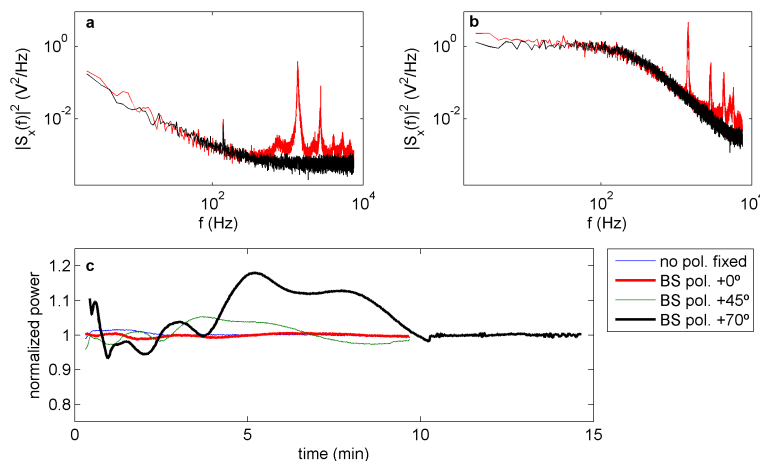
Figure 3.2.: Laser fluctuations. (**a**) Power spectrum recorded with no bead in the optical trap. In red (black), laser output is $P_{\text{output}} = 0.1$ W ($P_{\text{output}} = 2$ W) and the HWP rotates polarization parallel (obliquely) to the BS transmitting axis. Trap power is $P_{\text{trap}} = 10$ mW for both spectra. (**b**) The same spectra with 1.16-μm beads trapped. (**c**) Trap power recorded over 10 minutes. Oblique polarization with respect to the transmitting axis of the BS leads to power fluctuations due to polarization large-scale instability.

with linear polarization extinction ratio of 22 dB. See in Fig. 3.2c though, a certain instability for different polarization directions. The more orthogonal the polarization angle to the transmitting axis of the BS, the more visible the fluctuation, which is translated into power long-range instability. Differently, if no polarizing elements are used, P_{output} remains stable within less than 1% RMS. Also, the laser power remains stable within a similar RMS if polarization is set parallel to the BS transmitting axis.

An automated feed-back for stabilizing the laser power has been therefore programmed in LabView, which addresses P_{output} through an RS-232 interface when HWP 1 is required to control laser power. For the worst case in Fig. 3.2c, the laser power is stabilized from $t = 10$ min, within an RMS comparable to that reported by the manufacturer for P_{output}.

3.1.2. SLM characterization

Parallel nematic liquid crystal SLMs enable wavefront modulation in a phase-only performance. Liquid crystal is composed of anisotropic molecules whose extraordinary refractive index depends on their orientation with respect to the incident optical vector field [45]. This orientation can be tuned with computer-generated voltage signals, usually in the form of grayscale images in which each gray level corresponds to a voltage value and eventually to a local, pixel-wise phase delay. In our

set-up, modulation is applied to the horizontal polarization component, whereas the vertical component remains non-modulated, according to their being parallel to the refractive index ordinary axis. This will further enable splitting the laser beam into a holographically-modulated beam to draw several kinds of optical trap patterns, and a non-modulated, motionless beam creating an optical trap onto the optical axis [48], as shown in Section 3.2.

SLMs can be addressed both through digital and analog signals. As analyzed in Ref. [77], digital addressing leads to phase flickering due to the alternating voltage binary values generated through pulse-width modulation (PWM), finally giving rise to positioning instability. This can be considerably reduced by addressing SLM signals in an analog scheme. Our analog-addressed Hamamatsu X10468-03 SLM is driven by 8-bit DVI signals, thereby providing $2^8 = 256$ available phase values.

In order to assess the phase modulation for the horizontal polarization component, we shined a beam polarized at $+45^{\text{o}}$ onto the SLM, by properly orientating HWP 2 in Fig. 3.1, while a constant phase hologram was being displayed. The reflected beam intensity was recorded with a power meter (Thorlabs, S130C) placed after an analyzer at -45°. The phase delay, ϕ, between horizontal and vertical components leads to elliptical polarization for which the intensity after the analyzer reads as $I(\phi) = I_0 + A \sin^2 \frac{\phi}{2}$. In Fig. 3.3a, we show our SLM exhibiting a perfect linear response between the gray levels, g, and phase (the so-called look-up table, LUT). A sweep over the 256 values can hence be fitted by:

$$I(g) = I_0 + A \sin^2 \left[\frac{2\pi}{2M} (g - g_0) \right] \tag{3.1}$$

Here, M is the number of gray levels available between 0 and 2π and g_0 is the gray level for 0-phase modulation. Although phase modulation was linear, we did observe an effective phase modulation range beyond 2π, as has been reported by Albero *et al.* [78] and Calero *et al.* [79]. This effectively translates into less than 256 gray levels between 0 and 2π. In particular, we found values of M between 220 and 235, depending on the laser power and running time, as well as local variations due to the non-constant (ideally Gaussian) beam intensity profile. This is likely due to heating of the SLM, as suggested in Ref. [80]. In Fig. 3.3b, see the M values at different laser powers over 45 minutes. After an abrupt rise in the first 4-5 minutes (shaded area), it keeps slowly going up and nearly stabilizes after approximately 20 minutes. This will be taken into account in Section 3.2.2 to avoid *holographic drift* that leads to long-range trap positioning instability.

We further measured the local LUT by displaying constant phase values on pixels with greater effective size (Fig. 3.3c). The remaining pixels of the hologram were set to steer light off the power meter by applying a phase grating (see Section 3.2). In Fig. 3.3d, we obtained the Gaussian beam profile at the SLM by sending light polarized horizontally so as to not have the non-modulated counterpart, while the analyzer in front of the power meter was as well removed. The hologram was divided
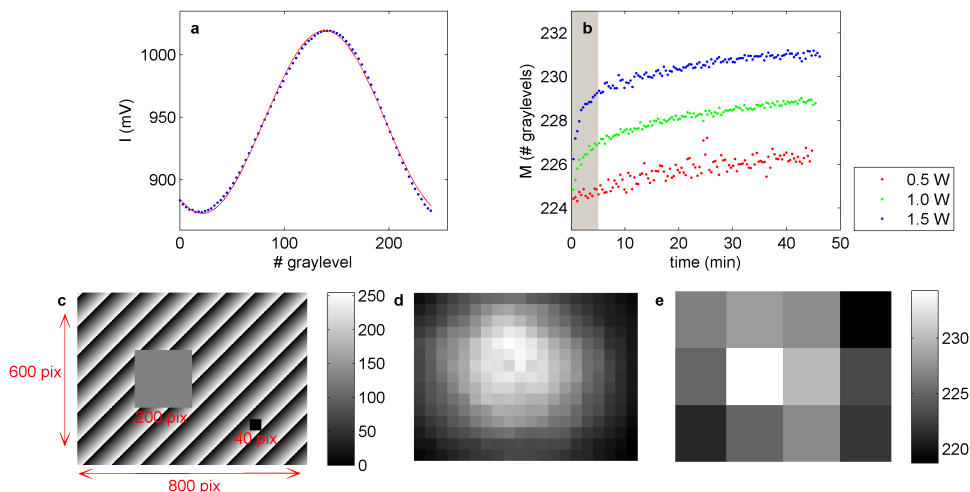
Figure 3.3.: SLM LUT analysis. (**a**) Intensity recorded from a power meter after an analyzer oriented at -45°. The incident beam is polarized at +45°. (**b**) M values for three different laser powers, over 45 minutes. (**c**) Typical hologram displayed for Gaussian beam profile and local LUT assessment with bigger effective pixels. (**d**) Trapping beam Gaussian profile obtained from holograms with 40x40 effective pixels. (**e**) Local values of M obtained over the SLM with 200x200 effective pixels.
.

into 15x20 effective pixels square-sized 40x40 (the total SLM pixel size is 600x800). The beam waist from fitting a 2D Gaussian to the data was 9.0 mm, similar to the theoretical value of 8.5 mm, calculated from the 5.1-mm-diameter waist laser output expanded through telescope 1 (See Section 3.1 and Fig. 3.1).

Variation of M over the SLM plane is shown in Fig. 3.3e. The SLM was now divided into 3x4 effective pixels of square size 200x200. Similar to the M-power dependence in Fig. 3.3b, M was observed greater for higher local intensity. As will be analyzed in Section 3.2.2, LUT inaccuracy is the main source of error in trap positioning, together with phase quantization effects.

3.1.3. Piezo-electric stage characterization for accurate drag force measurements

As depicted in the introduction of this thesis, most experiments to demonstrate the operation of beam momentum detection consist of applying controlled drag forces for which hydrodynamic analytical expressions are available, such as Eqs. 5.1, 5.2 and 5.3 in Chapter 5. Constant flow velocities were created by addressing triangular signals for $x_{piezo}(t)$ (Fig. 3.4a) such that stage velocity, $v_{flow} = v_{piezo}(t) = \frac{dx_{piezo}(t)}{dt}$, was thus a square-shaped waveform (Fig. 3.4b). In Fig. 3.4c, we compare the typical force signal obtained with the light-momentum sensor, i.e. $F_X = \alpha S_X$ (see

Section 2.3), with the hydrodynamic force through $F_{drag} = \gamma v_{flow}$ for a 3.00-μm bead captured in the optical trap.
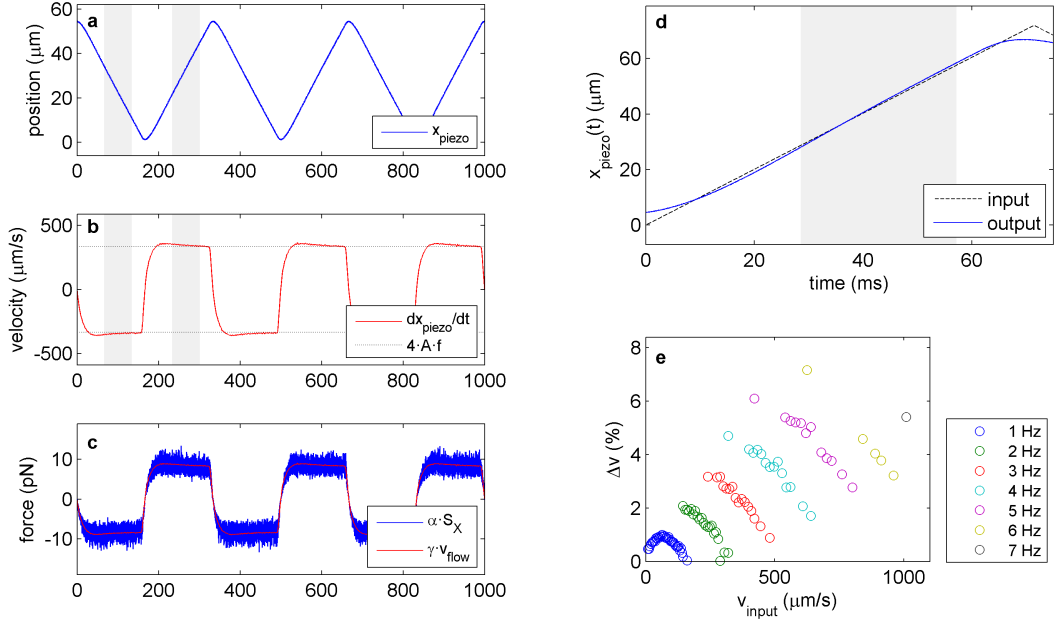
Figure 3.4.: Piezoelectric stage performance. (**a**) Triangular signal ($f = 3$Hz, $A = 28\mu$m) drawn by the stage. The shaded areas indicate the constant-slope timeframes. (**b**) Stage position derivative (red) and ideal velocity, $v_{flow} = 4Af$. The shaded areas indicate the constant-velocity timeframes. (**c**) Force obtained and ideal force signal, i.e. $\gamma \frac{dx(t)}{dt}$. (**d**) Triangular signal ($f = 3$Hz, $A = 28\mu$m) showing greater deviation. (**e**) Deviations for a series of driving frequencies and different amplitudes.

A close look onto the waveform makes one notice some deviation from the ideal triangular (stage position, $x_{piezo}(t)$) and from the derivative square (stage velocity, $v_{piezo}(t)$) shapes (Fig. 3.4d). This is due to the driving electronics transfer function, which decays similar to a single-pole-like function, as has been shown in Ref. [70] (Supplementary Information). This translates into the fact that constant velocity is only achieved within the 40% to 80% range of a semiperiod, approximately (see shaded areas in Fig. 3.4a,b,d).

In the experiments described in the next chapters, drag forces are eventually measured from the averaged 40-80% timeframe plateaus on signals analogous to Fig. 3.4c. For proper comparison with theoretical drag forces, flow velocities were as well measured over the same time range via the stage monitor output. Results are shown in Fig. 3.4e. Note discrepancies as high as 7% for certain amplitude-frequency combinations, especially for faster oscillations. To avoid waveform shape aberration, drag force experiments will be carried out at relatively low laser power.

This way, force accuracy assessment will be available up to the escape force with proper accuracy.

The absolute drag force is calculated as the half-difference between the two averaged plateaus, which automatically cancels out the initial momentum of the beam. To average the force values, approximately 10,000 data points are taken for a typical 50-kHz force signal. Signal averaging also eliminates zero-mean Gaussian noise, leading to eventually 20-fN to 50-fN standard deviation for measurements repeated over 20 cycles. Such reproducibility can be considered to be the minimum force value attainable for drag force measurements on microspheres.

3.2. Holographic steering of a single trap

Among the wide number of applications offered in optical trapping, SLMs can be applied to accurate beam steering and positioning of optical traps [23, 81]. A single beam is easily steered by generating a linear phase profile whose slope determines the deflection angle. The digital structure and the phase quantization of the SLM limit resolution but, for commercial SLMs having N $\sim$ 500 pixels and M $\sim$ 200 phase values, theoretically almost continuous positioning should be achieved [23]. In [26], a detailed analysis of the effects of phase quantization in a 1D phase-only SLM on beam steering is performed. They show that the staircase generated by the SLM pixels can lead to unexpected errors for certain steering angles, and they optimize the holograms to minimize the difference between the mean slope of the staircase grating and the aimed slope (a similar approach is performed in [39]). D. Engström and co-workers [26] also compare the theoretical predictions with experimental results, by measuring the center of mass of the far-field pattern of the steered beam. By artificially limiting the performance of the SLM down to $N = 256$ pixels and $M = 32$ phase levels, positioning deviations over steering angles of 2-3 mrad were outlined over the noise in the setup.

Microscope objectives are aplanatic lenses that satisfy the Abbe sine condition. The optical field distribution at the back focal plane (i.e. the plane containing the optical traps) is the Fourier transform of the electric field at the front focal plane, with a scaling factor λf, where λ is the laser wavelength and f is the focal length of the microscope objective [82]. Considering that telescope 2 (Fig. 3.1) conjugates the SLM plane onto the objective front focal plane with f_3/f_4 magnification, a linear phase profile displayed at the SLM of the form:

$$\phi^{ideal}\left(x;d\right) = \frac{2\pi}{\lambda f}\frac{f_4}{f_3}d\,x + \phi_0 \tag{3.2}$$

gives a displacement d of the focused beam at the trapping plane. ϕ_0 is an arbitrary offset phase value that can be used as a free parameter for optimization [26], as will be used in Section 3.2.2.2.

Considering the pixelated performance of the SLM, equation 3.2 reads as:

$$\phi_j^{ideal}(d) = \frac{2\pi}{\lambda f}\frac{f_4}{f_3}d\,x_j + \phi_0\ ;\ \ j = 1, ..., N \tag{3.3}$$

where the pixel position is now $x_j = p\,j$ (p is the pixel size) and N is the number of pixels along the steering direction. The effect on trap steering efficiency due to the discrete nature of digital holograms will be explained in Section 3.2.1.

The same conclusion can be drawn by considering the optical path slope applied to the wavefront (Fig. 3.5). In order to position the optical tap at a distance d from the optical axis, the SLM tilts the wavefront at an angle $\tan\alpha = \frac{d}{f}\frac{f_4}{f_3}$ (the beam is then magnified through telescope 2 as $\frac{f_3}{f_4}$). The optical path length modulated at the jth pixel will be $\delta_j = x_j\tan\alpha = \frac{\lambda}{2\pi}\phi_j$, whereby we can again obtain $\phi_j(d) = \frac{2\pi}{\lambda f}\frac{f_4}{f_3}d\,x_j$.

As will be shown in the next sections, the latter, slope-wise phase approach suffices for explaining the positioning deviation performance due to phase quantization (Section 3.2.2.2). Differently, deviations due to imperfect LUT will be described analytically from Fourier optics after applying the *mod 2π* function to the hologram, according to the fact that phase values are truncated at $\phi = 2\pi$.
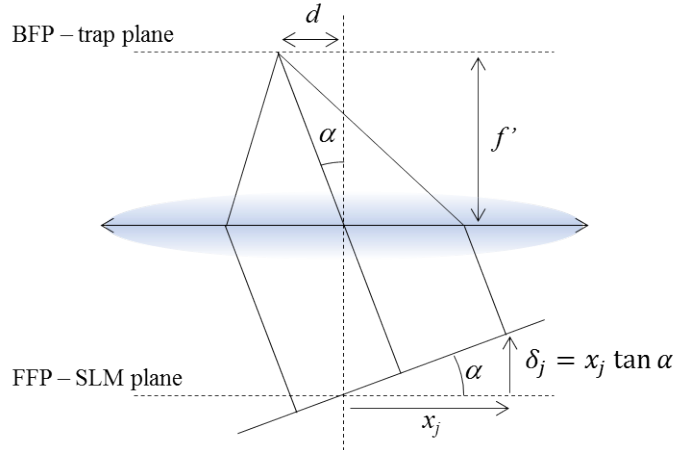
Figure 3.5.: Linear phase optical path.

Studies on beam steering accuracy have been scarce thus far, probably due to the difficulty of measuring positioning with the required precision. Trap positioning errors within $\sim$2 nm have been found in [81] for three holographic traps, for an SLM with N = 1080 pixels and M $\sim$ 200 phase values. These errors are mainly due to phase modulation deviations, i.e. in the conversion from the gray level (or voltage) addressed to the SLM at each pixel and the actual phase added locally to the incoming light beam. Mismatches on the look-up-table (LUT) conversion from gray levels to phase have been widely studied in terms of diffraction efficiency [80, 83], but not in terms of positioning accuracy.

In this section, we briefly analyze the efficiency drop when steering an optical trap off the optical axis and study both the phase quantization and imperfect LUT effects on single trap positioning. Trap positioning will be obtained by tracking trapped polystyrene microbeads, allowing subnanometer holographic trap displacement measurements, corresponding to steering angles of the order of 0.1 μrad. Importantly, it is necessary to split the laser beam into the non-modulated component, creating a static trap on the optical axis, and the modulated component that will be steered. This way, relative bead position cancels out drift-noise motion. In addition, trap focusing in terms of Fourier optics is used as a model to be qualitatively compared with measurements.

3.2.1. Efficiency

Single-trap steering efficiency can be predicted by focusing the optical field modulated by the discrete hologram described by Eq. 3.3 in terms of Fourier optics, with spatial frequency $u = \frac{x'}{\lambda f} \frac{f_4}{f_3}$ (x' is the spatial coordinate at the trapping plane). Let us consider the optical scalar field at the SLM plane as follows (see Appendix A.1):

$$U\left(x\right) = \mathrm{rect}\left(\frac{x}{L}\right)\left\{\mathrm{rect}\left(\frac{x}{p}\right) * \left[\sum_{n=-\infty}^{\infty} \delta\left(x - np\right) e^{i\frac{2\pi}{T}x}\right]\right\} \tag{3.4}$$

where $T = \frac{\lambda f}{d} \frac{f_3}{f_4}$ is used for simplicity, and p and L are the pixel and SLM size, respectively. By using the convolution and product properties of Dirac delta function and Fourier transform [82], we obtain:

$$\left|\tilde{U}\left(u\right)\right|^2 \propto \left|\sum_{n=-\infty}^{\infty} \mathrm{sinc}\left[L\left(u - \frac{1}{T} - \frac{n}{p}\right)\right] \mathrm{sinc}\left[p\left(\frac{1}{T} + \frac{n}{p}\right)\right]\right|^2 \tag{3.5}$$

The desired optical trap corresponds to the $n = 0$ term, for which $\mathrm{sinc}\left[L\left(u - \frac{1}{T}\right)\right]$ is equivalent to a plane wave diffracted through the SLM window, while it is weighted by the factor $\mathrm{sinc}\left(\frac{p}{T}\right)$ (see Eq. A.8):

$$\left|\tilde{U}\left(u\right)\right|^2 \propto \left|\sum_{n=-\infty}^{\infty} \mathrm{sinc}\left[p\left(\frac{1}{T} + \frac{n}{p}\right)\right] \mathrm{sinc}\left[L\left(u - \frac{1}{T} - \frac{n}{p}\right)\right]\right|^2 \tag{3.6}$$

In Fig. 3.6, the trap power as it is steered over a $\pm 50\,\mu m$ range is recorded from the S_{SUM} signal of the force detection instrument, and is observed to follow the efficiency curve arisen from Eq. 3.6. Mismatches are likely due to having not considered the finite size of the objective entrance pupil, quantization of the LUT or light driven at orders different from $n = 0$ still reaching the detector.

In addition, we used the S_x signals to calculate the trapping stiffness after recording the power spectrum density through back focal plane (BFP) interferometry. Trapping stiffness is proportional to the trap power, hence it is as well a good indicator for steering efficiency [80].
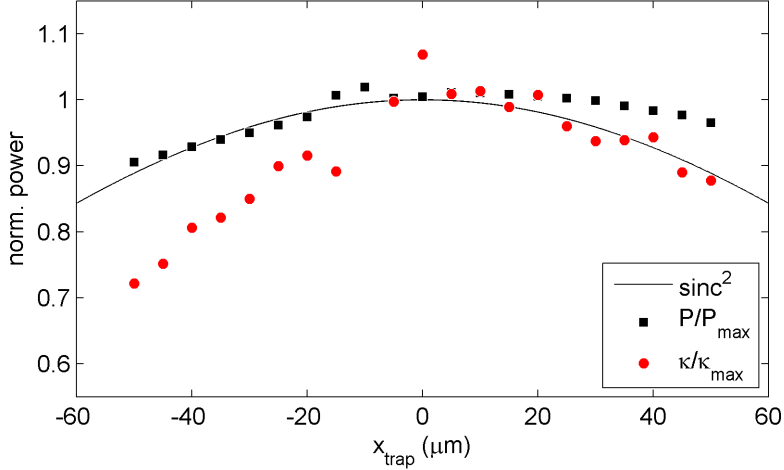
Figure 3.6.: Trap steering efficiency.

3.2.2. Trap positioning accuracy.

3.2.2.1. Bead tracking

As pointed out by Schmitz *et al.* in Ref. [23], almost continuous trap positioning is achievable by means of an SLM with $N = 512$ pixels (600x800 in our set-up) and $M = 130$ gray levels (220–235 in our set-up). We confirmed this by using the sub-nanometer tracking CISMM's software Video Spot Tracker [web] in a double-bead arrangement, so-called *dumbbell configuration*. As commented above, the two traps are created by shining the SLM with a 45°-polarized laser beam that splits into the modulated, steered trap after focusing through the microscope objective (horizontal polarization), and the non-modulated trap remaining static at the optical axis (vertical polarization) [48]. Both beams go past the same optical path, thereby being equally affected by drift noise due to the optical setup, i.e. in a parallel manner. Two 1.16-μm polystyrene beads are trapped and tracked from bright-field images after removing IR light with a neutral filter.

Drift noise cancellation is shown in Fig. 3.7a. In the top figures, position traces obtained at 24 fps for the two beads are represented, which clearly undergo parallel long-range, slow motion. The bottom figure shows the relative drift-less trajectory, which thereby exhibits Brownian-like motion. It is worth noting that stabilization

of the relative position occurs after approximately 4 minutes (shaded area), which corresponds to the transitory evolution of phase modulation shown in Fig. 3.3b.
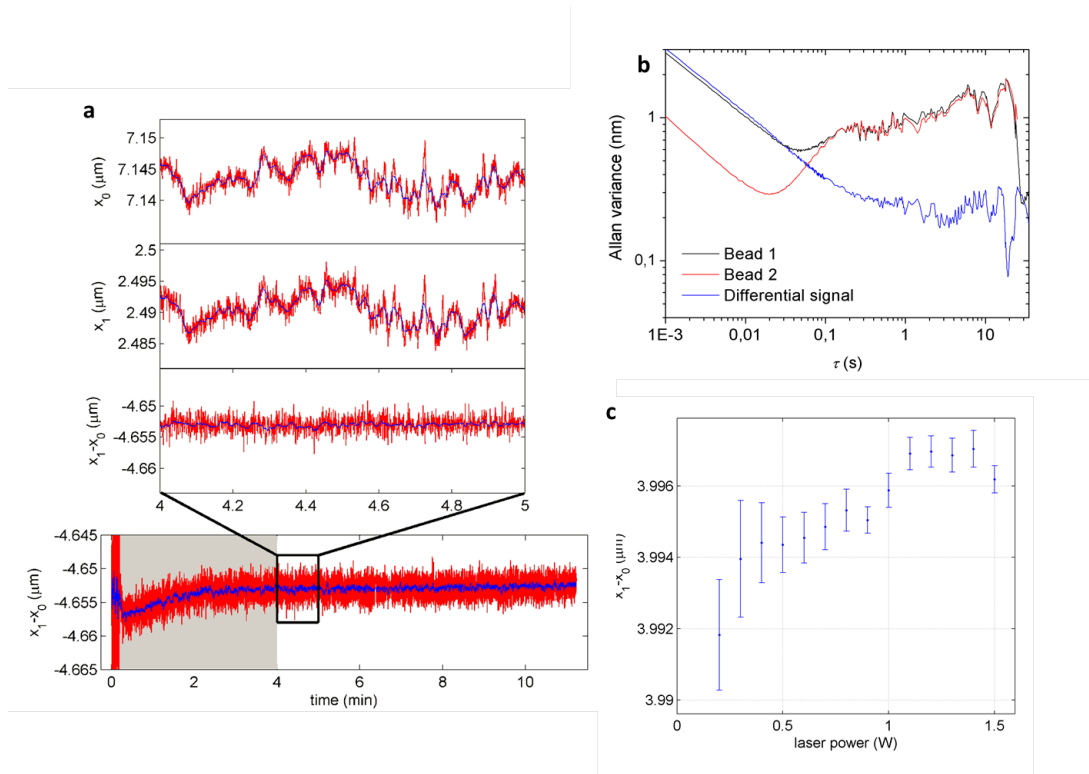
Figure 3.7.: Bead tracking. (**a**) Top - Position traces of the bead trapped by the non-modulated (bead 0) and modulated (bead 1) traps. Bottom - Relative position. In blue, signals smoothed by a 1-second digital filter. (**b**) Allan Variance for the three signals. (**c**) Relative position ($\bar{x} \pm \sigma_x$) as the laser power is increased.

Allan Variance analysis [84] for the three traces (bead 0, bead 1 and relative position) is shown in Fig. 3.7b.[1] At long-scale (large τ), see that the two beads experience highly correlated motion. In contrast, at low τ, motion is uncorrelated and the three signals exhibit the -1/2 slope according to the thermal limit.

We finally analyzed the effect of the laser-power-varying LUT of our SLM. In Fig. 3.7c, we show the relative position at different laser powers. Note that the LUT variation, shown in Fig. 3.3b, translates into actual positioning variations of up to 5 nm.

In the following measurements, we need highly control of the experimental conditions to achieve reproducible trap positioning. In particular, one needs to achieve a constant LUT response, for which the laser power needs to be set the same value

---

[1]Fig. 3.7b has been courtesy from F. Marsà and A. Farré, published in Ref. [48].

and, additionally, one needs to let the LUT stabilize a few minutes (10-20 minutes), according to Figs. 3.3b and 3.7a.

3.2.2.2. Positioning deviations due to phase quantization

As described in Section 3.1, our SLM is addressed through an 8-bit digital video interface (DVI). This results into a finite number of phase values in the $0 - 2\pi$ phase range, ideally $M = 2^8 = 256$, though it has been shown to be around 220-235 in Section 3.1.2. Every pixel takes the phase value that is closest to the ideal, what makes the linear phase profile in Eq. 3.3 therefore become:

$$\phi_j^{actual}(d) = \text{round}\left[\phi_j^{ideal}(d)\frac{M}{2\pi}\right]\frac{2\pi}{M} \; ; \;\; j = 1, ..., N \tag{3.7}$$

Such phase quantization leads to a staircase phase profile whose average slope will necessarily differ from the expected. In Fig. 3.8a, we show the ideal, continuous phase profile, $\phi^{ideal}(x;d)$; the ideal, pixelated phase profile, $\phi_j^{ideal}(d)$; the actual, pixelated phase profile, $\phi_j^{actual}(d)$; and the average, continuous phase profile, obtained from a linear fitting as $\phi_j = a\,x_j + b$. Actual trap positioning will be $d^{actual} = \frac{\lambda f}{2\pi}\frac{f_3}{f_4}a$ and will differ with respect to $d^{ideal} = \frac{\lambda f}{2\pi}\frac{f_3}{f_4}\frac{\phi_j^{ideal}(d)}{x_j}$.

The addition of an arbitrary phase offset in Eq. 3.2, as proposed by Engström *et al.* [26], leads to a different average slope, a. As shown in Fig. 3.8b, adding ϕ_0 to the phase staircase makes some of the pixels reach a different phase value after rounding in Eq. 3.7. This property can thus be used to optimize $d^{actual} \sim d^{ideal}$.

Phase-quantization-induced positioning deviations are shown in Fig. 3.8b. Curiously, these deviations especially occur around positions defined by phase slopes equal to an integer number (n) of gray levels per pixel, $\phi_j = n\frac{2\pi}{M}j$, i.e. so-called *M-positions*:

$$d_M^{(n)} = n\frac{\lambda f}{Mp}\frac{f_3}{f_4} \tag{3.8}$$

Although *M-positions* are perfectly reproduced because quantized phase values from Eq. 3.7 are equal to the ideal ones through Eq. 3.3, positioning around them behaves as shown in Fig. 3.8c. In our set-up, for a typical case of $M = 228$ gray levels, and $N = 600$ pixels, *M-positions* are $d_M^{(n)} = 1.1655\,n$ (μm) and deviations can reach 2-3 nm, which can be detected with video tracking after drift elimination, as described in Section 3.2.2.1. Re-positioning performance by the addition of ϕ_0 is shown in Fig. 3.8c - insets i and ii for two example positions.

Indeed, experimental results are shown in Fig. 3.8c. Trap positioning near $d_{M=228}^{(4)} = 4.662\,\mu$m fails with 2-3 nm errors in the first 5 nm (affected domain), whereas it is almost perfect, with clear subnanometer accuracy, beyond 5 nm (non-affected
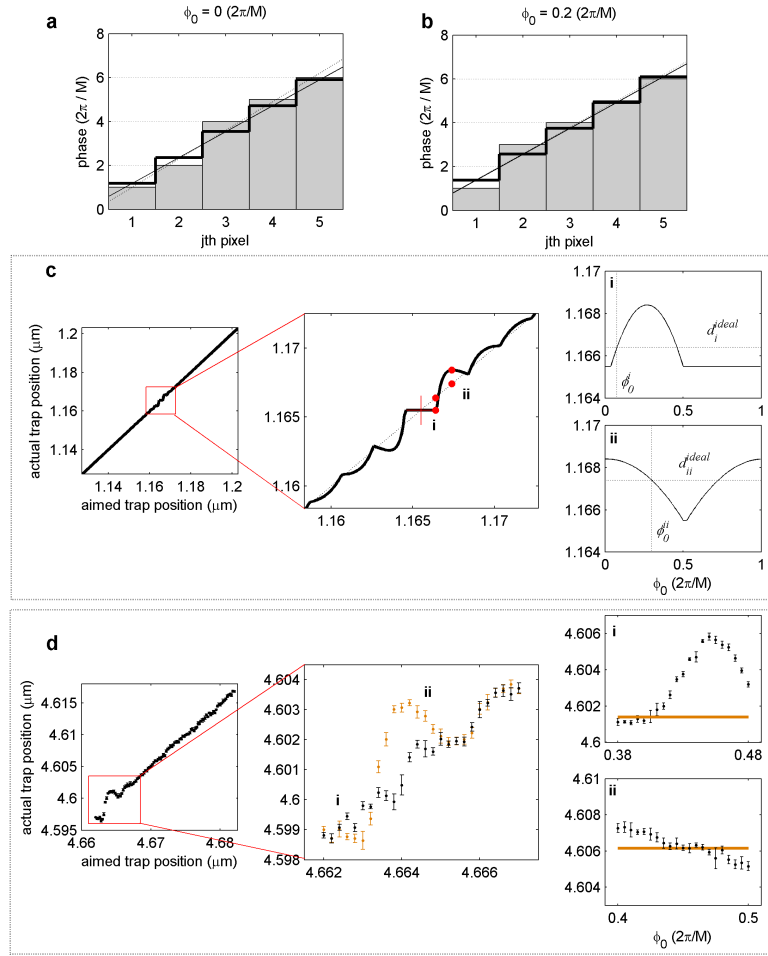
Figure 3.8.: Phase quantization effect on trap positioning. (**a**) Hologram with reduced number of pixels ($N = 5$). The continuous line is the ideal linear phase profile, $\phi^{ideal}(x)$, to steer the trap at d^{ideal} and the dashed line is the average phase profile obtained from the linear fitting, $\phi_j = a\,x_j + b$, eventually steering the trap at d^{actual} (see text). The thick line staircase represents the ideal discrete phase values, ϕ_j^{ideal}, and the bar plot corresponds to the nearest phase values, ϕ_j^{actual}. (**b**) For the same case, the addition of ϕ_0 produces a change in the 2nd pixel, which yields to an average phase profile closer to the ideal. (**c**) Trap positioning simulated over a position sequence around $d^1_{M=228}$. Insets i and ii show the effect of adding the term ϕ_0 for trap positioning at d_i and d_{ii}. Phase offsets, ϕ_0^i and ϕ_0^{ii}, optimizing for positioning at d_i^{ideal} and d_{ii}^{ideal} are indicated. (**d**) Mean positions ($\bar{d} \pm \sigma_d$) obtained from video tracking and phase optimization for two positions (insets ii and ii).

domain). Position correction is superimposed and exhibits an accuracy comparable to the non-affected domain. Two examples of the position changes for the addition of ϕ_0 are shown in Fig. 3.8d - insets i and ii.

3.2.2.3. Positioning deviations due to non-ideal LUT

As has been analyzed in section 3.1.2, our SLM exhibits a perfectly linear LUT with certain variations in the phase modulation range, which are mainly dependent on the laser power. The phase delay introduced by displaying the graylevel g, ideally $\frac{2\pi}{2^8}g$, will instead be $\frac{2\pi}{M}g \equiv a\frac{2\pi}{2^8}g$. For the typical case with $M = 228$, $a = 2^8/228 = 1.12$. In this section, we present a continuous model to qualitatively describe the effects of using a phase modulation range different from 2π on trap positioning. Further, we suggest a correction scheme similar to that used presented byu Engström *et al.* in Ref. [26] and used in Section 3.2.2.2.

Linear phase profiles, such as that in Fig. 3.5, become linear phase gratings due to the limitation of the SLM to modulate the wavefront within a finite phase value. This translates into the need of applying a *mod 2π* function, which instead leads to phase holograms with a sawtooth shape (Fig. 3.9a). To drive the trap onto position d, the optical field at the SLM plane can be described as follows (see Appendix A):

$$U(x) = \text{rect}\left(\frac{x - x_0}{L}\right) \cdot \left[\sum_{n=-\infty}^{\infty} \delta(x - nT) * \left(e^{i\frac{2\pi a}{T}x} \cdot \text{rect}\left[\frac{x - \frac{T}{2}}{T}\right]\right)\right] \quad (3.9)$$

where $\phi(x) = \frac{2\pi a}{T}x$ accounts for the actual phase scaling as $\phi^{actual} = a\,\phi^{ideal}$. The period of the grating, T, is related to the ideal steering position as $d = \frac{\lambda f}{T}\frac{f_3}{f_4}$, as used in Section 3.2.1. Here, x_0 and L are the center and length of a window defining the finite size of the SLM.

As discussed before, the scalar optical field at the trapping plane is the Fourier transform with spatial frequency $u = \frac{x'}{\lambda f}\frac{f_4}{f_3}$, hence:

$$\left|\tilde{U}(u)\right|^2 \propto \left|\sum_{n=-\infty}^{\infty} \text{sinc}(n - a)\, e^{i\pi\left(\frac{2x_0}{T} - 1\right)n} \text{sinc}\left[L\left(u - \frac{n}{T}\right)\right]\right|^2 \quad (3.10)$$

This summation can be understood as a series of diffraction peaks, $\text{sinc}\left[L\left(u - \frac{n}{T}\right)\right]$, each of which is modulated by the function $\text{sinc}(n - a)\, e^{i\pi\left(\frac{2x_0}{T} - 1\right)n}$ (Fig. 3.9b). The position of the nth peak, $u_n = \frac{n}{T}$, corresponds to $x'_n = \frac{\lambda f}{T}\frac{f_3}{f_4}n$. For the ideal case $a = 1$, all the terms vanish except for $n = 1$, hence the trap is created at $d = x'_1 = \frac{\lambda f}{T}\frac{f_3}{f_4}$, as expected, with an efficiency of 100%.

For other cases ($a \neq 1$), not only does the efficiency decrease due to the appearance of other diffractive orders (Fig. 3.9b), but we can have a close look into the intensity
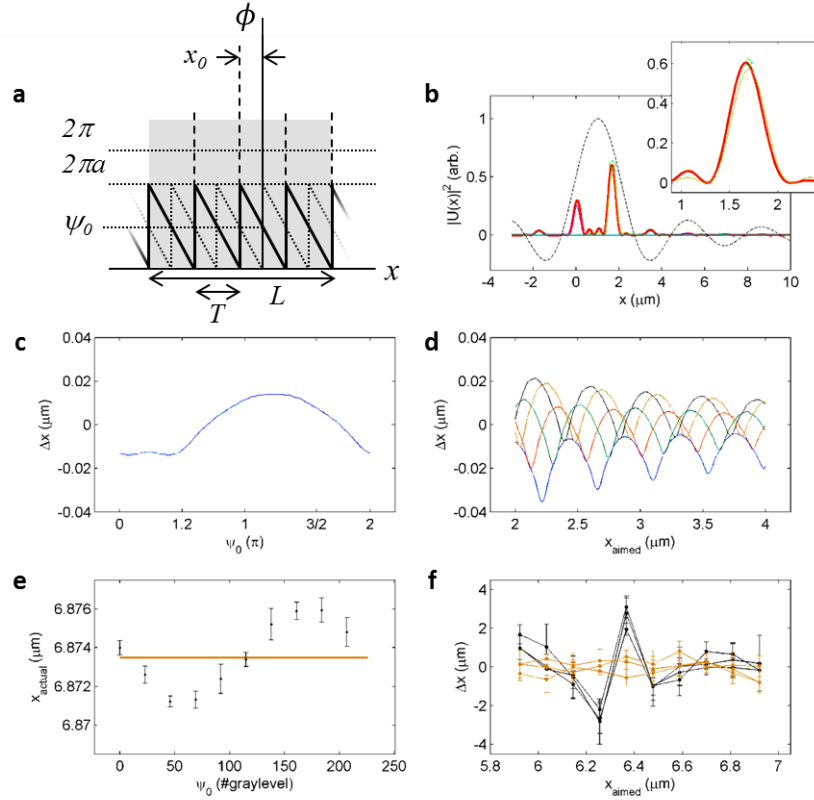
Figure 3.9.: (**a**) 1D Linear phase grating displayed by the hologram to create the optical trap at $d = \frac{\lambda f}{T}\frac{f_3}{f_4}$. T and L are the period and length of the grating. ψ_0 is the phase offset introduced to the hologram to induced a shift of x_0. The phase mismatch at $2\pi a$ eventually induces a drop in efficiency and trap positioning deviation. (**b**) In different colors, we represent absolute value for the the $n = -2, ..., 5$ terms the summation in Eq. 3.10. In red, their complex addition. The dashed line is describes de $\text{sinc}\,(n - a)$ factor. (**c**) Simulated position modified by the addition of ψ_0 at $x_{trap} = 3\,\mu$m. (**d**). Position deviation for constant $\psi_0 = 0$ (blue), $\psi_0 = 0.4$ (red), $\psi_0 = 0.8$ (orange), $\psi_0 = 1.2$ (black) and $\psi_0 = 1.6$ (green), over the $x_{trap} = (2, 4)\,\mu m$ range. (**e**) Experimental modification of trap positioning for a certain ideal position. (**f**) Deviations with no corrections (black) and ψ_0-optimization.

profile to notice a small deviation in the effective trap position (inset). In this simulated example ($a = 0.6$), we can see that the actual intensity profile is perturbed by the existence of other orders. Eventually, the trap position (considered by a center-of-mass calculation) will be different than the ideal from the 1st ($n = 1$) order.

On the other hand, we can use x_0 as a free parameter to reach the position closest to d, though no improvement in efficiency would be achieved, since x_0 only alters the relative phase between the orders. Mathematically, a change in x_0 can be produced by adding a certain offset phase, ψ_0, to the hologram. This is interestingly similar to the addition of ϕ_0 introduced in Section 3.2.2.2, since the same positioning correction strategy can be implemented.

The position variation induced by shifting the hologram through ψ_0-addition is shown in Fig. 3.9c for $a = 0.6$ and $L = 12$ mm. Indeed, there exists a certain value for ψ_0 that optimizes the trap position. In Fig. 3.9d, trap positioning for different constant ψ_0 values is shown. A certain periodical behavior can be observed, with a period of $u_L = \frac{1}{L}$, arising from the *sinc* function in Eq. 3.10. In spatial dimensions at the trapping plane, the period turns out, for the specs in our set-up:

$$d_L = \frac{\lambda f}{L} \frac{f_3}{f_4} = 0.4429 \mu m \tag{3.11}$$

Parameter d_L is an estimator of positioning inaccuracy due to imperfect LUT in relative terms and is so-called *L*-distance. In other words, steps far smaller than the *L*-distance will in principle be performed perfectly, while oscillations in trap positioning accuracy become visible for steps in the order of d_L.

The model described in Eq. 3.10 simplifies the effective LUT by considering $\phi^{actual} = a \phi^{ideal}$ over the whole SLM. Nonetheless, in Section 3.1.2 we showed that the LUT has more of a local response, probably due to the non-constant beam intensity profile. This leads to theoretical results notably different than experimental measurements, but on the other hand this permits to qualitatively predict the existence of micron-range positioning inaccuracy on the order of 2-3 nm and correction by ψ_0-addition, i.e. hologram shifting.

That hologram shifting induces changes in trap positioning, which can eventually be optimized, is experimentally shown in Fig. 3.9e. Trap position oscillates approximately ± 3 nm in the $\psi_0 = (0, 2\pi)$ range. In Fig. 3.9f, a similar ± 3 nm amplitude of deviation is shown for holograms created with the same $\psi_0 = 0$ for all positions, while it is corrected to less than ± 1 nm through ψ_0-optimization.

3.2.2.4. Discussion on single trap positioning accuracy

The two sources of positioning deviation are visible in different ranges. While phase quantization affects positioning over 5-10 nm around M-positions (Eq. 3.8), inaccuracy due to LUT mismatch is visible in positioning steps comparable and larger

than the L-distance (Eq. 3.11). It is interesting that correction proposed by Engström *et al.* [26] in order to correct for phase quantization (addition of ϕ_0) can be extrapolated to correct for non-ideal LUT (addition of ψ_0, i.e. hologram shifting). Otherwise, we envisage that correction of the local dependence of the LUT, which has been observed to correct for steering efficiency [80], would as well correct for trap positioning accuracy.

A comment on experimental intricateness is a need. Trap positioning and image tracking of the trapped beads with subnanometer accuracy is dramatically affected by any kind of optical aberration, drift and imaging optics. This eventually lessens the capacity to carry out experiments with sufficient reproducibility and forces ϕ_0 and ψ_0 optimizations to be performed *in situ*. After changing any of the experimental situation affecting trapping (e.g coverslip, trapped bead or spherical aberration compensation by the microscope) or tracking (e.g. illumination NA or Köhler system alignment), bead position measurements have repetitively exhibited variations of the order of 1nm. That is the order of the deviations observed in our case with $N = 600$ pixels and $M = 228$ gray levels.

Another issue strongly influencing trap positioning is the drift component remaining after relative position measurement in our *dumbbell* configuration. We believe that this arises from the LUT evolution throughout time (Fig. 3.3b) and so-call it *holographic drift*. In Fig. 3.7a, we showed an example of relative position stabilization. Nonetheless, position optimization experiments can last much longer than 10 minutes and unexpected position instability from LUT variations can likely occur. Thereby, the set of ϕ_0 and ψ_0 values for correction would be no longer valid and a new correction sweep should be performed.

Importantly, such lack of reproducibility is subject to the fact that we are using our SLM under its full capacity ($N = 600$, $M = 228$), which drives our deviations from ideal positioning down to the nanometer scale. In other works [26, 39], smaller values for N and M are used to produce larger deviations, i.e. over the detection limit, to test for correction. To conclude, we confirm that SLMs with a high number of pixels ($N \sim 500$) and phase levels ($M \sim 200$), facilitate continuous single-trap positioning within 2-nm deviations (induced by phase quantization and LUT aberrations). After correction for such effects, positioning is achieved with sub-nanometer accuracy.

3.3. Multiple trap generation

Holographic wavefront modulation in optical tweezers has been widely used to generate patterns of multiple traps to manipulate several particles at the same time [24, 22, 23], as well as large objects that need more than a single trap for stable trapping and orientation [34, 33, 69].

In Ref. [24], R. di Leonardo *et al.* review some of the algorithms most used for multiple-spot generation in HOTs and discuss the different compromise between

calculation time and efficiency. Another thorough description can be found in J. Mas PhD thesis [85]. Here, we briefly describe the algorithms used in further chapters that best fit to the needs of our experiments.

3.3.1. Prisms-and-lenses

Fast calculation of holograms for multiple-trap generation can be achieved through prisms-and-lenses algorithm. It lies in the direct addition of the complex amplitudes driving single traps in 3D. For transverse displacements, the complex amplitude arises from the linear phase gratings -emulating prisms- described in Section 3.2. For axial displacements, quadratic phase profiles emulating lenses are needed. Once the complex amplitudes are calculated, the resulting phase is displayed at the SLM as follows:

$$\phi(x,y) = \arg\left(\sum_j e^{i\phi_j(x,y)}\right) \tag{3.12}$$

We have used this scheme to rapidly generate dual trap configurations for trapping cylinders perpendicular to the optical axis, as will be shown in Chapter 5. We allow one of the traps to remain static at the optical axis, hence its phase profile will be a plane wave at angle $\alpha = 0$. The second trap will be created by a phase grating of the form described in Eq. 3.2. Note that the *mod 2π* function must be applied before the addition of the complex amplitudes. Taking $T = \frac{\lambda f}{d}\frac{f_3}{f_4}$ for simplicity, as has been done in the previous section, and steering the trap along the x axis, the complex amplitude will be:

$$\sum_j e^{i\phi_j(x)} = 1 + e^{i\frac{2\pi}{T}x} = \left(1 + \cos\frac{2\pi}{T}x\right) + i\left(\sin\frac{2\pi}{T}x\right) \tag{3.13}$$

from where we can easily obtain that the phase is:

$$\phi(x) = \arctan\left[\frac{\sin\frac{2\pi}{T}x}{1 + \cos\frac{2\pi}{T}x}\right] = \frac{\pi}{T}x \tag{3.14}$$

The same result can be obtained by applying $a = 0.5$ to the formalism introduced in Eq. 3.10. In this way, the $\text{sinc}(n-a)$ function modulating the diffractive orders will yield a 0th order (static trap) and 1st order (movable trap) weighted by the same factor. The works by Albero *et al.* [78] and Calero *et al.* [79] point to the same result when the phase modulation range is modified. In particular, prisms-and-lenses algorithm in Eq. 3.14 and the $a = 0.5$ case in Eq. 3.10 corresponds to the phase modulation range being equal to π.

3.3.2. Random-mask

Another approach for the direct addition of complex fields generating multiple trap patterns is the random-mask encoding algorithm introduced by our group in 2006 [86]. To create an array of n traps, it briefly consists of randomly splitting the pixels composing the hologram into n series of pixels. For our 600x800 SLM, each multiplexed hologram would have $\frac{4.8 \cdot 10^5}{n}$ pixels. The hologram defined by Eq. 3.3 is assigned to each series of pixels according to d_i . In Fig. 3.10a, a random-mask multiplexed hologram creating the three optical traps in Fig. 3.10b is shown. The superposition of the three linear phase gratings is clearly visible.
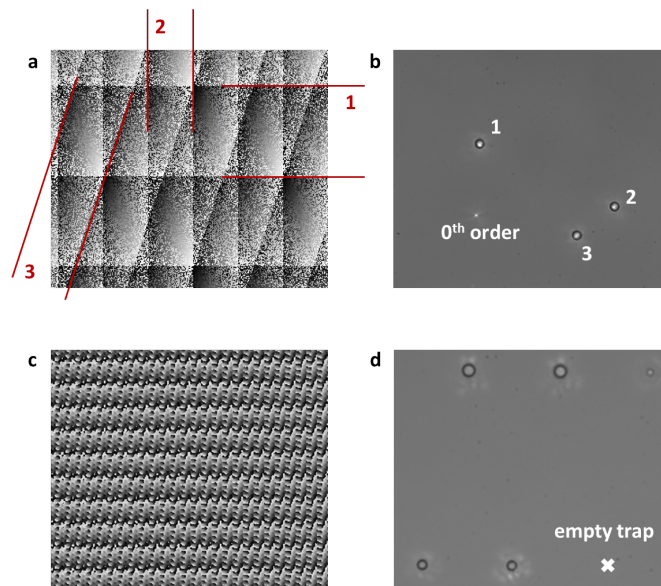
Figure 3.10.: Holograms for multiple trap generation. (**a**) Random mask hologram generating traps 1, 2 and 3 in (**b**). Red lines highlight the linear phase gratings superposed to create the three traps. In (b), a strong 0th order is as well indicated. In (**c**), a Gerchberg-Saxton hologram generating the array of six HOTs in (**d**) is shown.

The fast performance of the random-mask multiplexing algorithm comes at the cost of lower diffracting efficiency. As can be seen in Fig. 3.10b, a strong, undesired 0th order spot is created. To correct for such decrease, slower iterative (but considerably more efficient) algorithms are needed.

3.3.3. Gerchberg-Saxton algorithm

Both prisms-and-lenses and random-mask multiplexing algorithms constitute fast approaches to create arbitrary arrays of optical traps in real time. However, the drop

in efficiency is dramatic as the number of traps is increased, what makes it highly recommendable to explore new strategies to compute multiple-trap holograms.

Gerchberg-Saxton iterative algorithm works out the phase profile displayed on a phase-only SLM that creates the desired amplitude distribution at the sample plane. The algorithm is based on the digital Fourier transform (DFT). The field amplitude at the sample plane is set to be the desired pattern, while the hologram at the SLM is imposed to be a constant amplitude, phase-only field distribution. After some iterations, the algorithm converges and yields a hologram with, theoretically, 100% efficiency [24, 85]. The hologram shown in Fig. 3.10c creates the six-trap array (Fig. 3.10d) that will be used in Chapter 5 for force measurements.

As discussed by C. Schmitz *et al.* in Ref. [23], DFT-based performance for hologram computing limits the precision at the sample plane. The artificial discretization, i.e. the minimal spatial frequency, coincides with the L-distance introduced by Eq. 3.11.

3.4. Exotic beam optical traps

A promising application of wavefront modulation in optical manipulation is the creation of exotic traps with interesting properties beyond the parabolic potential created by a focused Gaussian beam. Some examples in HOTs set-ups are the generation of Laguerre-Gaussian beams with topological charge $l \neq 0$ to transfer orbital angular momentum to trapped particles [28], extended optical traps [87], optical solenoid beams [88] and tug-of-war optical tweezers with strong transverse momentum transfer for splitting cellular clusters apart [29].

Apart from holographic wavefront modulation, complex trapping geometries have been used to create tractor beams [89], and AOD-based set-ups have been applied to create object-adapted optical potentials [90, 91, 92, 93].

We here explore the generation and trapping of microspheres by means of cogwheel beam traps [27]. As will be discussed in Chapter 5, these are used in this thesis to perform calibration-free force measurements, from light-momentum detection, in an example of a non-Gaussian beam.

3.4.1. Cogwheel beam traps

Cogwheel beam tweezers are obtained by the superposition of two doughnut beams of equal opposite helical index l, meaning the optical field modulation takes the form $e^{il\theta} + e^{-il\theta}$, being ϑ the azimuthal coordinate [27]. A phase-only hologram with $l = 4$ is shown in Fig. 3.11a. The optical trap created by focusing the beam through the microscope objective is simulated in terms of a 2D Fourier transform in Fig. 3.11b. Observe that the number of azimuthal lobes appearing in the focus spot is twice the helical mode l. An image of our cogwheel trap, obtained by reflecting the trap

onto the lower coverslip of our micro-chamber is presented in Fig. 3.11c. On the other hand, note the appearance of the non-Gaussian "cog" modulation pattern at the BFP of the force detection set-up (Fig. 3.11d).
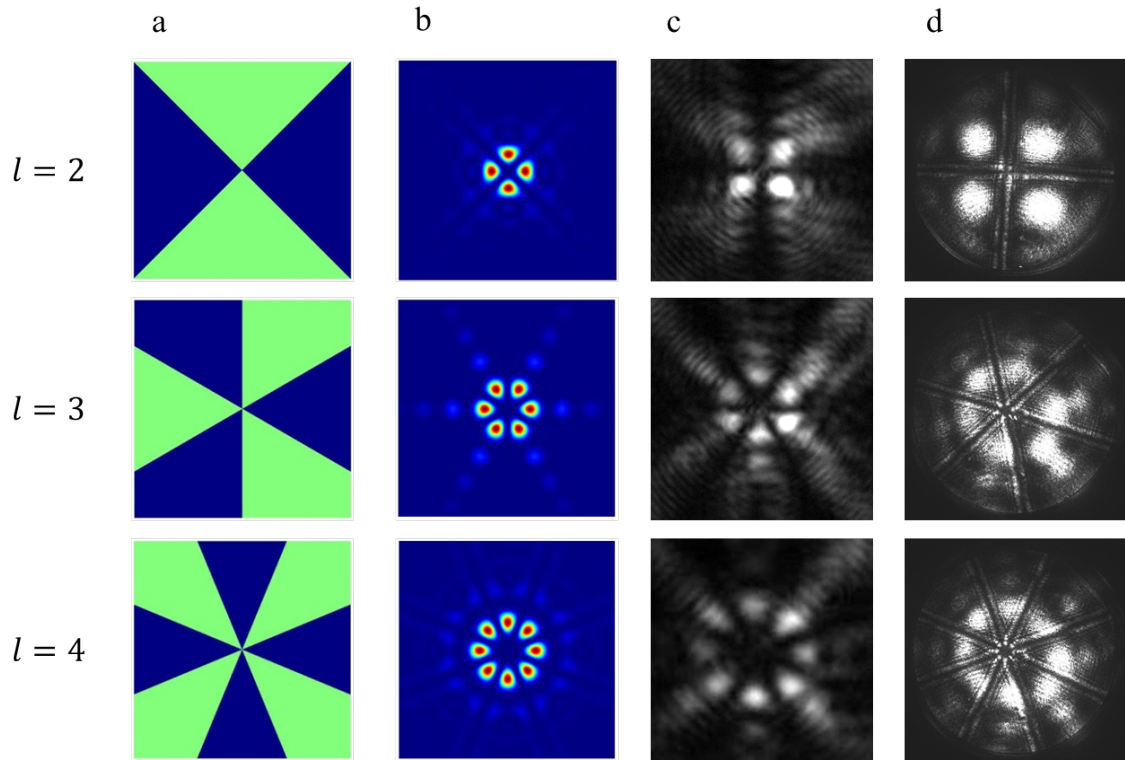
Figure 3.11.: Cogwheel holograms. (**a**) Holograms generating $l = 2, 3, 4$ cogwheel beams. (**b**) Transverse profile at waist and (**c**) actual image in our set-up (trap reflection at the coverslip). (**d**) Beam diffraction pattern at the BFP captured with a CCD camera for a 4.94-µm, PS bead trapped in the optical tweezer.

As reported by Jesacher *et al.* [27], only particles surpassing a certain size get trapped in these optical tweezers for a given helical mode, thus suggesting interesting applications in passive size-selective particle sorting. In our case ($\lambda = 1064$nm, NA = 1.2), 3.00-µm PS micro-spheres were stably trapped in $l \leq 3$ beams, 4.94-µm PS micro-spheres in $l \leq 4$ beams and 8.06-µm poly-methacrylate (PM) micro-spheres in $l \leq 13$ beams. Smaller micro-beads were actually pushed upwards as they could not be trapped for any l value.

4. Robustness of light-momentum force measurements

As discussed in Chapter 2, the first condition for accurate measurement of beam momentum changes is the capture of all the light emerging from the traps and thus contributing to the global momentum exchanged with the trapped samples. This is especially delicate when using single-beam optical tweezers, although they pose clear technical advantages with respect to counter-propagating beam traps.

When creating high-NA, single-beam traps, we need to make sure that 1) backscattered light losses represent a relatively small fraction of the total light scattered by the samples, and 2) the forward 2π solid angle is fully captured by an aplanatic lens (i.e. it fulfills the Abbe sine condition). Under these terms, the detection performance through Eq. 2.14a will be equivalent to the theoretical perspective of Eq. 2.4a.

In the practical implementation of beam momentum measurements, such equivalence might miss due to using samples that back-scatter a substantial fraction of light. Similarly, some situations may cause light loss or the Abbe sine condition to fail, for example, when creating the traps at a plane distant from the working distance of the aplanatic lens. In addition, the optical system transmittance is strongly variant for large angles, which high-NA collecting lenses need to be compensated for.

All these issues are addressed in the following chapter in two steps. First, we explore the tolerance of the forward-scattered light-momentum detection system and determine the effects mentioned on force measurements by using drag forces as a calibration reference. Similarly, we use scattering simulations to estimate measurement errors. Experimental solutions to these effects are shown to minimize force inaccuracy down to the limit strictly due to backscattering.

Second, backscattering accounting for measurement deviations is determined numerically from simulations of the far-field angular distribution of beam intensity. Forward-backward splitting of light scattering is obtained from FDTD computation as described in section 2.1. Results are then confirmed experimentally, again, by using well-calibrated Stokes drag forces, as well as fast, AOD-based stepping for obtaining force and captured light profiles[1].

---

[1] We thank Raúl Bola for developing the acquisition software synchronizing AOD light modulation with force detection and devising the scanning experiments.

Previous to this analysis, we discuss Stokes-drag calibration as a fast and precise test for the performance of light momentum detection. Different to the power spectrum method used before as a reference for the absolute momentum calibration (see Section 2.2 and Ref. [21] by A. Farré *et al.*), Stokes-drag offers a one-step strategy to analyze measurement accuracy, as well as the fact that force detection can be studied within the whole trapping range –i.e. up to the escape force–.

4.1. Introduction. Deviations in light momentum detection

In Section 2.3, we described the main technical aspects for the implementation of light-momentum detection for force measurements in optical tweezers. We concluded that, provided that a position sensing detector (PSD) is used to integrate the transverse component of light momentum at the BFP of a high-NA collecting lens (NA $> n_m$), the voltage signals match lateral forces if:

1. The detection system fulfills the Abbe sine condition and maximizes light collection.

2. The optical transmittance of the detection set-up is constant over the whole angular range, especially for high-NA rays.

3. Most part of photons are scattered, following optical trapping, within the forward 2π solid angle.

From a theoretical perspective, this leads to a Volt-to-picoNewton relationship invariant to the local optical trapping dynamics, constituting a macroscopic force calibration of the form:

$$F_x = \alpha_{detector} \cdot S_x \equiv \frac{R_D}{\psi f' c} \cdot S_x \tag{4.1}$$

where R_D and ψ are the sensor radius and sensitivity, f' is the system focal length and c is the speed of light. As well, trapping power is obtained as $P_{trap} = {}^1\!/\!_\psi \cdot S_{SUM}$. From now on, we will discern such calibration from the actual, *in situ* calibration factor, α_{trap}, and we will thereby name it $\alpha_{detector}$. In non-optimized, typical BFP interferometry detection systems, α_{trap} is highly sensitive to the specific properties of the experiment (e.g. trapping power, sample size and refractive index), whereas it turns out to be constant –and equal to $\alpha_{detector}$– in light-momentum detection set-ups [21].

Yet some practical deviations from the ideal conditions 1, 2 and 3, necessarily lead to the actual α_{trap} differing form the ideal $\alpha_{detector}$ even in the light-momentum, optimized BFP interferometry scheme thoroughly described in Refs. [20, 21, 62]. That is, resulting into errors in force measurements. It is important that not only

does α_{trap} differ from $\alpha_{detector}$, but it becomes dramatically sensitive on the experimental parameters, leading to the loss of the invariant property of light-momentum detection. The scattered pattern of the trapping beam strongly depends on the properties of the scatterer, e.g. refractive index, size and position within the optical trap. Inhomogeneities in the beam collection performance (e.g. light loss and instrument transmittance non-uniformity) result thereby in variations of the signal-to-force conversion α_{trap}.

This chapter is therefore focused on the analysis of the discrepancies induced by the practical implementation of light-momentum measurements and discuss the limits in the accuracy after compensating for the effects associated with light detection. As we will show in the next sections, an important part of these discrepancies comes from an incorrect capture of the forward-scattered light as this represents most of the trapping beam. We will finally show that measurement inaccuracy can be brought from $15-20\,\%$ to the minimum strictly due to back-scattered light loss, around $5\,\%$.

4.1.1. Drag force measurements as a calibration reference

Detector calibration, $\alpha_{detector}$, can be tested against actual trap calibration, α_{trap}, using two of the approaches introduced in Section 2.2. In Ref. [21], A. Farré *et al.* described the optimization method in order for BFP interferometry to detect light-momentum changes and demonstrated, both theoretically and through power spectrum experimental calibration, the invariant feature of α_{trap} on a range of microspheres. On one hand, linear trapping response permits to define a spring constant (κ, pN/µm), such that $F_x = -\kappa \cdot x$. On the other, little particle displacements within the optical trap can be tracked through the detector sensitivity (β, µm/V), i.e. $x = \beta \cdot S_x$. It was thereby shown that, if BFP interferometry was optimized to account for the aforementioned point 1, the product $\alpha_{trap} = \kappa \cdot \beta$ was constant and equaled $\alpha_{detector}$ (pN/V).

Here we use an alternative scheme which we consider has several advantages over the former, thermal-based approach. Stokes-drag calibration of optically trapped spherical microbeads has become robust and well-established, thanks to the fact that measurements are accessible in a single step, through $F_{drag} = 6\pi\eta R v_{flow}$ (η: medium viscosity[2], R: particle radius, v_{flow}: flow velocity)[3]. Thermal motion analysis (e.g. power spectrum calibration [94] or equipartition theorem) is reduced to a small region around the trap equilibrium position due to the lightness of Brownian forces. In contrast, Stokes drag can operate over a wider range and can eventually provide escape force calibration [59], clearly increasing the extent for calibrated force values. Since the Stokes-drag scheme sets the external force for which α_{trap} is calibrated, measurement discrepancy can as well be analyzed as a function of it.

---

[2]Viscosity dependence on temperature is considered as described in detail in Chapter 6.

[3]Faxén sphere-to-surface factor is omitted for simplicity. See Eq. 2.11.

Furthermore, Stokes-drag forces have been widely applied for trap calibration on non-spherical samples, as was discussed in Section 2.2. In Chapter 5, hydrodynamic expressions for slender cylinders or sphere-to-sphere interaction will be used to test the light-momentum performance on irregular samples.

In Section 3.1.3 we described our using a piezo-electric stage to induce controlled drag forces, from which we can calibrate α_{trap}, for the case of microspheres, as follows:

$$\alpha_{trap} = \frac{6\pi\eta Rb\, v_{flow}}{\langle S_x \rangle} \tag{4.2}$$

where $\langle S_x \rangle$ is the average voltage output of the sensor over the constant velocity time frame (see Fig. 3.4). In Fig. 4.1, typical force deviation curves are shown for a set of polystyrene microbeads of different diameters up to the escape force. Here, forces are measured as $F_{measured} = \alpha_{detector} \cdot S_x$ and are compared to F_{drag}. Note that the measurement error depends on the force applied or, similarly, on the position in which the trapped particle locates to optically counterbalance the drag flow (especially for the largest beads). This will be discussed in depth in the next sections.
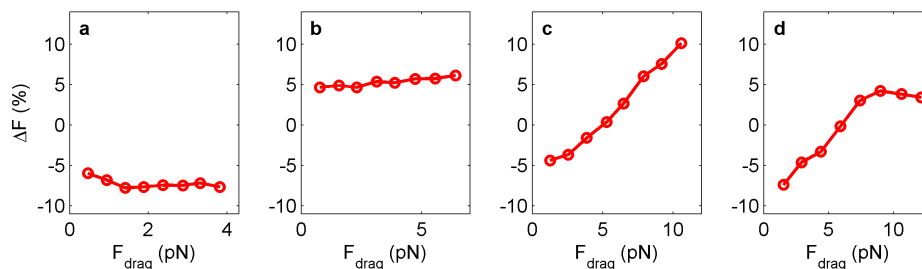
Figure 4.1.: Example of a deviation curve for 061-µm (**a**), 1.16-µm (**b**), 1.87-µm (**c**) and 3.00-µm (**d**) polystyrene (PS) microbeads in a 20-mW optical trap.

We compared α_{trap} calibrations from both procedures to confirm that discrepancy arises from deviations in the light momentum detection performance, instead of some kind of inaccuracy related to the experimental method. As shown in Fig. 4.2, both α_{trap} obtained via Stokes calibration at low forces, and via power spectrum calibration ($\alpha_{trap} = \kappa \cdot \beta$), accurately coincide. This indicates that some features in relation to points 1, 2 and 3 –which ensure the invariant property of the macroscopic calibration $\alpha_{detector}$– fail to a certain extent and, as will be discussed, need to be corrected for.

Importantly, we can observe that although the error in the force calibration reached a $\pm 5 - 10\,\%$ in this example, light loss accounted for $2 - 3\,\%$ at most. This evidences that the amount of light collected cannot be used as a reliable indicator of the quality of the measurements, due to our unknowing the momentum information

Figure 4.2.: Deviation of actual trap calibration with respect to $\alpha_{detector}$. Stokes-drag α_{trap} values are obtained in the limit $F_{drag} \to 0$.
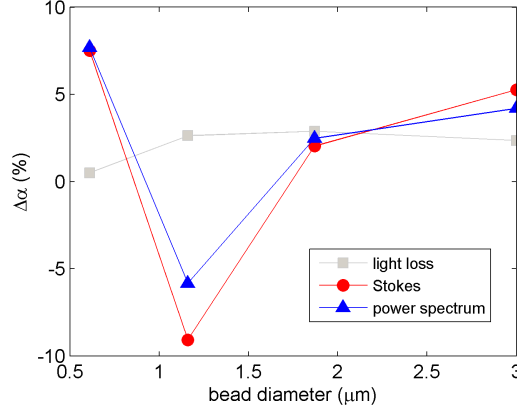
missing alongside lost light. Instead, two strategies will be used in order to assess trap calibration accuracy. First, a vast range of calibration results in situations with different properties will be used as a suitable predictor for further force measurements. Second, simulations will shed light onto the scattering properties of several samples and will be used to determine the contribution to the momentum exchanged with them arising from back-scattered light.

4.2. Tolerance of the force detection instrument

In the following section, we examine conditions 1 and 2, which are required for properly conveying the forward-scattered beam onto the PSD placed at the BFP. Condition 3, regarding the loss of momentum information along with backscattered light, will be studied in Section 4.3.

First, we studied the effect of axial incorrect positioning of the force detection instrument (condition 1). This leads to an effectively different numerical aperture ($\mathrm{NA_{eff}}$) that produces less than a 2π forward solid angle to be captured. Besides, this causes the Abbe sine condition to fail. We measured the $G(\theta)$ function to show the actual correspondence between angles at the sample plane and ray impact positions at the BFP plane, $x = f'G(\theta)$ [20]. Finally, positioning of the optical trap is as well explored. Especially in thick chambers (used in further Chapter 7 for working with zebrafish embryos), creating the trap at the bottom surface produces high light loss for which the detection instrument position needs to be accurately corrected.

Second, the effect of the instrument non-uniform transmittance is studied (condition 2). Especially for large angles, Fresnel coefficients at the different lens surfaces differ from angles near the optical axis. This can be corrected with a compensating mask at the BFP.

We used polystyrene (PS) spherical microparticles of four different diameters (0.61 μm, 1.16 μm, 1.87 μm and 3.00 μm) as good targets for drag force experimental references. As mentioned above, forces are measured through $F_{measured} = \alpha_{detector} \cdot S_x$ and are compared to $F_{drag} = 6\pi\eta R v_{flow}$ to test for light-momentum calibration deviations. In order to complement the discussion from a qualitative perspective, far field simulations accounting for the effects mentioned are as well presented.

4.2.1. Instrument and trap position

4.2.1.1. Instrument height

The first problem we encounter is the difficulty in setting the height of the instrument from the sample. This involves two main questions: where to put the instrument and how to set it reproducibly. An incorrect positioning of the system can lead to essentially two different effects: losses of light due to the truncation of the lateral components of the momentum or the modification of the beam structure due to the deviation from the Abbe sine condition.

In either case, the error introduced in the measured force depends on the intensity distribution scattered by the sample and may yield therefore different instrument responses for different conditions. This ultimately translates into both a larger discrepancy between samples of different kinds (loss of the invariant property of light momentum calibration) and to errors in the absolute value of the force calibration ($\alpha_{trap} \nsim \alpha_{detector}$).

To show the variation of the instrument's force response in the presence of controlled light losses, we analyzed the measured drag force truncating the light pattern at different NA$_{\text{eff}}$. We used rings of calibrated size placed at the BFP of the front lens of the instrument to partially block the laser from the trap (Fig. 4.3). Their inner diameter, D_{in}, was selected so that the effective capturing angle of the lens, θ_{eff}, could be reduced in a controlled manner, $NA_{\text{eff}} = n \sin\theta_{\text{eff}} = D_{in}/2f'$. Four values, NA$_{\text{eff}}$ = 1.33, 1.3, 1.25, 1.2, were selected. Values lower than that of the trapping objective (water-immersion, NA = 1.2) were disregarded as they would introduce too large errors.

As expected, results in Fig. 4.4a-d show that the error introduced by the different rings does not only depend on the sample kind but also on the applied force, since the result ultimately relies on the specific structure of the scattered intensity. Discrepancies between different microspheres can increase by 10% when NA$_{\text{eff}}$ is reduced down to that of the trapping objective. Likewise, for a single particle at a given applied force, differences in the measured force of 5-10% can show up. This can drive to maximum discrepancies between different conditions of 20-25%.

Changes in the measured force can be qualitatively explained by the light patterns observed at the BFP of the collecting lens (Fig. 4.3). When the diameter of the bead increases, the scattering structure varies from a uniform disk to a sort of
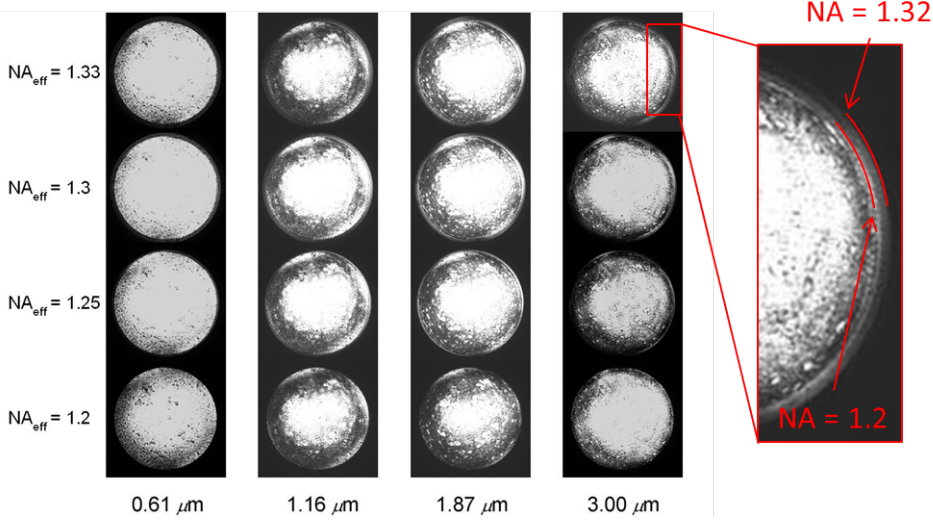
Figure 4.3.: BFP images after rings truncating the beam at NA_{eff} = 1.33, 1.3, 1.25, 1.2 are placed at the BFP of the collecting lens.

reduced pattern. For particles smaller than the beam waist ($D \lesssim 2\omega_0 \sim 1\,\mu m$), the intensity distribution can be approximated by the addition of a simple spherical wave, observed here as a faint disk of NA_{eff} = 1.33, and the reference incident beam with NA_{eff} = 1.2. As the particle is displaced, both the spherical wave and the incident beam remain unaltered, and only the interference term between them changes. Neither of the two first terms carries net transverse momentum, so only the interference pattern confined in the disk of NA_{eff} = 1.2 contains information about the force. This explains why the measurement barely changes when the light between NA_{eff} = 1.2 and NA_{eff} = 1.33 is blocked.

For the largest particles, the interaction between laser and sample can be described in terms of ray optics. In this case, the sphere acts as a small lens focusing the incident beam. This produces a contraction of the pattern at the BFP of the lens; light is confined in smaller NA_{eff}. Transverse displacements of the trapped object produce motions of the entire pattern.

When the particle is pulled by a large force, the beam can be eventually deflected to angles larger than those given by the NA of the incident beam, producing an underestimation of the pattern displacement and therefore of the force if light at $NA_{eff} > 1.2$ is truncated. This reduction in the measured force is clearly observed for 1.87-μm 3.00-μm particles. For intermediate sizes, $D \sim \lambda$, the error introduced in the measurement is a combination of the two extreme cases.

In Fig. 4.4e-h, we show simulations for the situations plotted in Fig. 4.4a-d. Although average accuracy is observed to be substantially better, we do notice the different experimental behavior for the different size of the beads. Whereas the smallest, 0.61-μm bead shows a flat force deviation curve, larger beads exhibit a force-dependent inaccuracy originating from the beam being deflected beyond
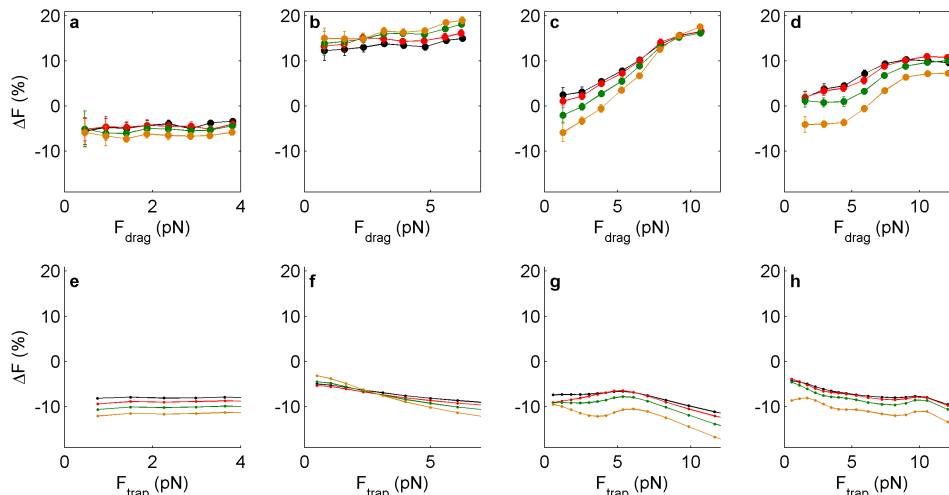
Figure 4.4.: Drag force measurements on 0.61-μm (**a**), 1.16-μm (**b**), 1.87-μm (**c**) and 3.00-μm (**d**) PS beads after reducing NA_{eff} by means of different blocking rings at the BFP of the beam collection lens. Far field simulations of this effect are shown for 0.61-μm (**e**), 1.16-μm (**f**), 1.87-μm (**g**) and 3.00-μm (**h**) beads. Colors correspond to $NA_{eff} = 1.33$ (black), $NA_{eff} = 1.3$ (red), $NA_{eff} = 1.25$ (green) and $NA_{eff} = 1.2$ (orange) in all figures.

$NA_{eff} = 1.2$ in a ray-optics picture. As well, reducing NA_{eff} results in a decrease in the absolute force measurement by the order of 5%. This is clearly visible to coincide with measurements on 1.87-μm and 3.00-μm beads.

This simulation considers the effect of the non-uniform transmittance of the collecting lens, since the compensating mask used to correct for this effect could not be placed together with the calibrated blocking rings at the BFP. Explanation for the average -10% deviation when simulating the non-uniform transmittance is discussed in section 4.2.2.

Forced light loss shown in Fig. 4.4 reproduce the effect of real NA_{eff} reduction when positioning the instrument at an incorrect height. For a situation in which this locates at $z = 2\,\text{mm}$ above the ideal position, we obtain $NA_{eff} = 1.2$, besides certain beam pattern aberration at the BFP due to the failing Abbe sine condition. In Section 4.2.1.2, this will be explained in detail and a reproducible solution for the instrument axial position corresponding to the trap working plane will be used.

To accurately determine NA_{eff}, we used a calibrated ring with the correct aperture while carefully making the beam size at the BFP coincide with it. For this position, we measured the drag force applied on the same set of four PS microspheres and we compared the result with that obtained in the correct position. As can be observed in Fig. 4.5, force measurements decrease with the higher positioning of the force detection set-up. We found a mean change in the force calibration of 4%, similar to that observed for the blocking ring with $NA_{eff} = 1.2$ in Fig. 4.4.

Again, variations were slightly different for the several particles due to the different scattering patterns for each bead. This might explain the difference between the 1.16-μm bead measurement deviation here (-5%), and that obtained from artificially blocking the captured light cone at $NA_{eff} = 1.2$ (+4%).
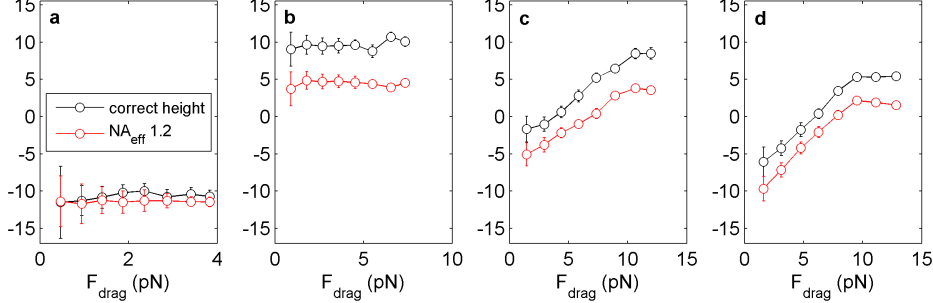

Figure 4.5.: Drag force measurements on 0.61-μm (**a**), 1.16-μm (**b**), 1.87-μm (**c**) and 3.00-μm (**d**) PS beads after positioning the force detection at $z = 0.2$ mm from the ideal working plane (hence reducing NA_{eff} down to 1.2).

4.2.1.2. Optical trap position in thick microchambers

In the optical trapping experiments shown so far, we used thin microchambers that were made of a coverslip and a microscope slide spaced with a 90-μm-thick double-scotch tape. We here study the light-momentum detection performance in thicker chambers that are needed, for instance, in experiments with 500-μm zebrafish embryos (Chapter 7).

We performed this study by displaying calibrated phase patterns at the SLM that become visible at the BFP and can be used to measure the $G(\theta)$ function to observe the fulfillment –or fail– of the Abbe sine condition. As schemed in Fig. 4.6a, the SLM (plane A) is conjugated, through telescope 2, onto the front focal plane of the trapping objective (plane B). In turn, this is conjugated onto the collecting lens BFP (plane C) and, last, onto the PSD plane (plane D), through the relay lens. This makes the hologram become visible with a CCD substituting the PSD[4]. Square patterns were displayed to show the dramatic distortion when the trap is created off the working plane (Fig. 4.6b), while circular patterns were used to measure impact ray positions, x, at the BFP (Fig. 4.6c).

The Abbe sine condition is strictly valid for a specific position of the lens –i.e so-called *working distance*–, and at a particular plane, the top interface between the suspension medium and the glass surface. Actual $G(\theta)$ might deviate from Abbe's

---

[4]Ideally, phase-only holograms should not be visible at the BFP, but it is likely due to a slight affection from imperfect conjugation that 0 - π phase jumps become noticeable.
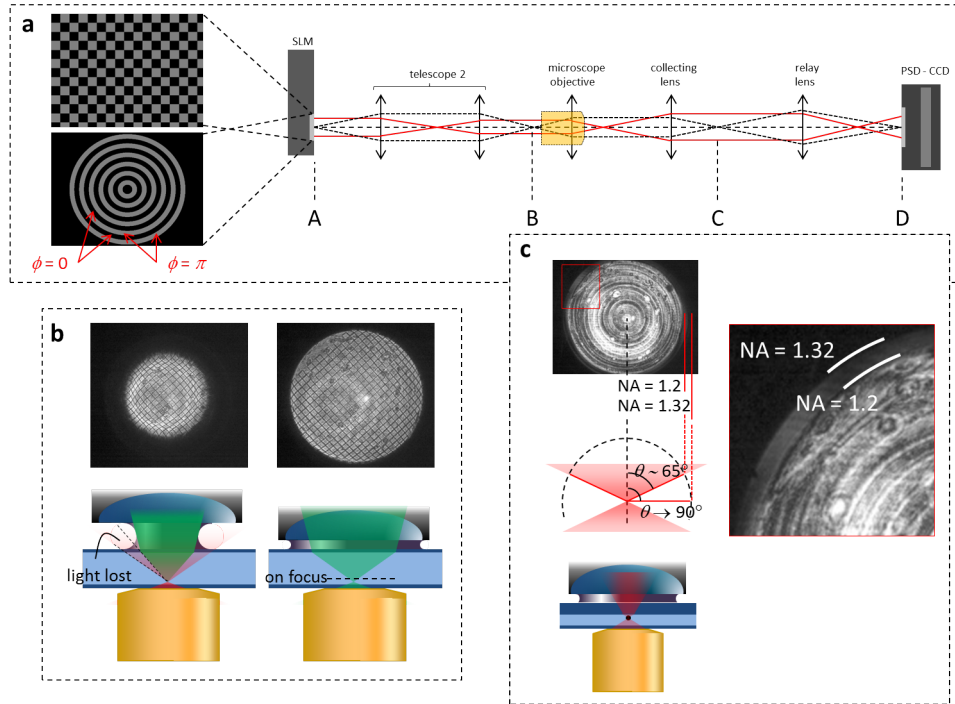
Figure 4.6.: Loss of the Abbe sine condition. (**a**) Experimental sketch of the holographic patterns used to observe distortion and measure the $G(\theta)$ function. (**b**) Effect of improper setting the force detection instrument height leading to a working plane different from the trapping plane. (**c**) Typical circular pattern to measure $x = f'G(\theta)$. Note the appearance of the NA = 1.32 disk due to the presence of a bead in the optical trap.

due to the front lens itself, to a wrong positioning of the same or the trapping plane, and due to the design of the relay lens system.

In order to place the instrument at the proper height from the sample, we first need to observe, by means of a CCD camera at the BFP, that the beam diameter equals that expected from the Abbe sine condition, i.e. $D = 2 \cdot f' \cdot n \sin \theta_0 = 2 \cdot f' \cdot \mathrm{NA}$ (θ_0 is the divergence angle for the current trapping objective, e.g. water-immersion, NA = 1.2). Note the focal length here, f', is that of the instrument –considering the relay lens–, but not that of the collecting lens. When this is fulfilled, an iris (or alternatively a reference element) is placed at the illumination path so that it appears in sharp focus at the trapping plane. From now on, the CCD can again be substituted by the PSD and the instrument height is determined by the iris imaging condition at the trapping plane. Deep details on this method for accurate axial positioning of the force detection instrument are published in Patent [95].

In Fig. 4.6b, we show a beam profile affected from positioning the trap at the bottom surface of a 500-μm-thick camber, while the detection instrument locates such that the iris image plane is at the top surface. As easily observed, a large amount of light, especially that propagating at large angles, is not captured by the collecting lens.

Moreover, a strong aberration of the square pattern appears. Importantly, a perfect square shape, as well as the accurate beam diameter for NA = 1.2, is recovered when the iris image working plane coincides with the trapping plane, demonstrating that the Abbe sine condition is successfully recovered.

We next measured the $G(\theta)$ functions in 300-µm and 500-µm chambers. We performed this measurement by displaying a circular pattern at SLM, whose size (largest circle) corresponded to the NA = 1.2 rays. By creating the trap onto a 1.16-µm microbead as a scatterer, light travelling up to NA = 1.32 (i.e $\theta \to 90^{\circ}$) appeared, so that $G(\theta)$ could be measured up to the full angular domain (Fig. 4.6c).

In the ideal case, the iris image plane and the trapping plane are placed at the top, water-coverslip interface. We can observe that $G(\theta)$ fulfills the Abbe sine condition, i.e. exhibiting a perfect response from which the linear fit leads to a system focal length of $f' = 2.16\,(\pm 0.5\%)\,$mm (Fig. 4.7a). Differently, when creating the optical traps at $z = 300\,\mu$m and $z = 500\,\mu$m down from the top interface, $G(\theta)$ collapses and gets considerably distorted, resulting in a noticeable reduction of NA_{eff}.

Different to the Abbe sine condition expressed in terms of Eq. 4.3a, we can model distortion in Fig. 4.7b through Eq. 4.3b, which fits distortion with accurate agreement:

$$x = f'n \sin\theta \tag{4.3a}$$
$$x = f'(1 - A\sin^m\theta)\,n\sin\theta \tag{4.3b}$$

As a qualitative study on the impact of such aberration onto force measurements, Eq. 2.14a can be modified to include for this effect:

$$S_{\text{x}} = \frac{\psi}{R_D}\iint\limits_{PSD} f'(1 - A\sin^m\theta)\,n\sin\theta\,I(x,y)\,\mathrm{d}x\mathrm{d}y \tag{4.4}$$

Here, we can identify the term $T_{eff} \equiv (1 - A\sin^m\theta)$ as an effective transmittance –due to the $G(\theta)$ curvature induced by the loss of the Abbe sine condition– to emulate the actually measured force, F_x, through Poynting vector integration in the far-field (from Eq. 2.4a):

$$F_{\text{x}} = \frac{n}{c}\iint\limits_{2\pi} T_{eff}(\theta)\,I(\Omega)\sin\theta\cos\phi\,\mathrm{d}\Omega \tag{4.5}$$

After such transformation, we obtained the results in Fig. 4.8. Force measurement deviation in the 300-µm thick microchamber case is estimated to decrease by 10%, whereas it turns out to be dramatically erroneous in 500-µm thick microchambers, not only due to the fail of the Abbe sine condition, but as well due to the high loss of light. NA_{eff} in this case is 0.9.
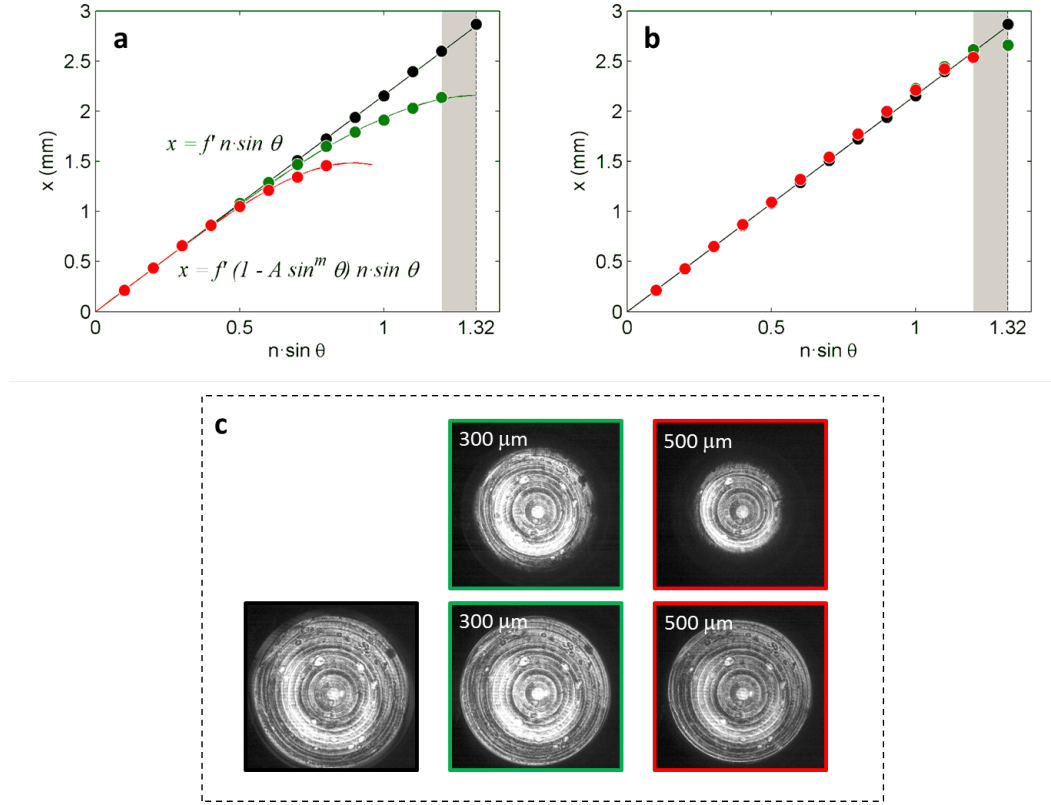
Figure 4.7.: $G(\theta)$ functions in thick chambers. (**a**) The iris image plane is placed at the top, water-coverslip interface while the trapping plane is created at $z_{trap} = 0$ (black), $z_{trap} = 300\,\mu$m (green) and $z_{trap} = 500\,\mu$m (red) from the interface. The black linear curve is the Abbe sine condition fit (Eq. 4.3a) to the measured impact positions, x, while the red and green curves are fits using Eq. 4.3b. (**b**) Same measurements after locating the force detection instrument so that the iris image plane coincides with the trapping plane. (**c**) BFP images corresponding to the different measurements in **a** and **b**. In the upper images, the iris image plane is at the top interface while, in the lower images, it coincides with the trapping plane.
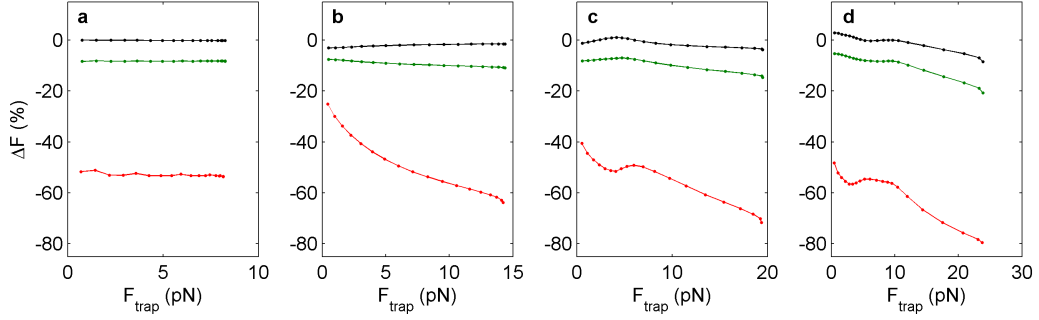
Figure 4.8.: Simulations of the fail of the Abbe sine condition in thick chambers for 0.61-μm (**a**), 1.16-μm (**b**), 1.87-μm (**c**) and 3.00-μm (**d**) PS microspheres. In all the figures, the ideal case is plotted in black, whereas traps created at the bottom interface of 300-μm (500-μm) thick microchambers are plotted in green (red).

Fortunately, light loss can be minimized and the Abbe sine condition notably recovered after relocating the instrument by making the iris image plane coincide with the trapping plane. In Fig. 4.7b, we can observe that an effective focal length equal to that in the ideal case ($f' = 2.16 \, (\pm 0.5\%)$ mm, obtained from linearly fitting $G(\theta)$) is perfectly recovered. In the 300-μm case, we obtain $f' = 2.19 \, (\pm 1.8\%)$ mm and, for the 500-μm case, we obtain $f' = 2.19 \, (\pm 0.9\%)$ mm.

However, in spite of recovering the Abbe sine condition, light loss still occurs for such thick chambers, especially in the 500-μm thick ones. In Fig. 4.7b, see that rays traveling beyond NA = 1.2 are missed by the collecting lens. We can therefore assume force measurement deviations comparable to those shown by the use of blocking rings with calibrated diameter, around 10%.

In Fig. 4.9, we indeed see that drag force measurements at the bottom interface of a 500-μm thick microchambers are 10% lower than those carried out at the upper interface. This agrees with the results shown in Fig. 4.4, where light loss produced by blocking the captured beam beyond $NA_{eff} = 1.2$ leads to a 5% decrease in the measured force for 0.61-μm PS beads, whereas 3.00-μm PS beads suffer from a 10% reduction. As has been discussed, larger beads tend to deflect the trapping light at angles higher than θ_0 (for $NA_{eff} = 1.2$), which explains the stronger deviation in these measurements.

All in all, the use of an iris at the illumination optical plane to reproducibly set the instrument height has been shown to maintain α_{trap} calibration within a $\pm 5\%$ in all the samples used. Similar, it has been shown to be equal to the macroscopic, $\alpha_{detector}$ calibration within a $\pm 10\%$ margin of error. On the other hand, simulations can be used to explain, in a qualitative approach, the errors arisen from light loss and the fail of the Abbe sine condition.
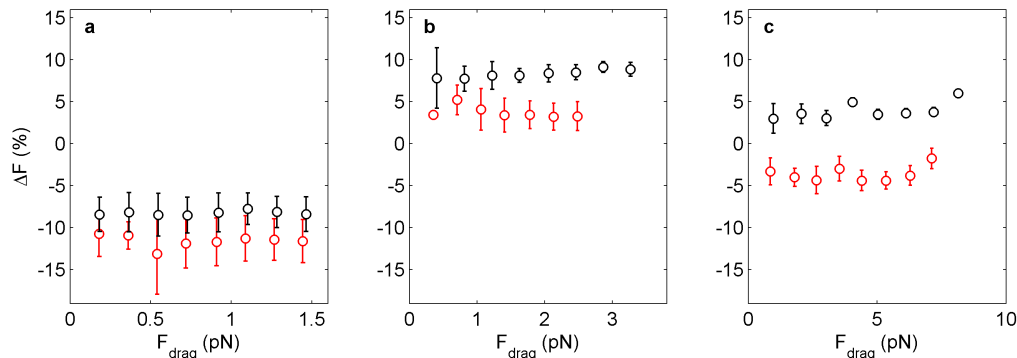
Figure 4.9.: Drag force measurements in thick microchambers on 0.61-μm (**a**), 1.16-μm (**b**) and 3.00-μm (**c**) PS microspheres. In all the figures, measurements at the top (bottom) interface off a 500-μm thick microchamber are plotted in black (red). The iris image plane and the trapping plane coincide in both.

4.2.1.3. Optical trap lateral position

To conclude, we assessed possible loss of light and force measurement deviations from driving the traps off the optical axis. In Fig. 4.10, we recorded the power of an empty trap steered holographically along X and Y to show that there was no loss of light resulting from the position of the optical trap in the trapping plane. That is, we found decreased intensity for off-center traps merely due to diffraction of the pixilated SLM. In Section 3.2.1, the same decrease was observed when determining trap stiffness through power spectrum calibration. We additionally applied a 60-μm/s flow to induce a drag force of 1.6 pN on a 3.00-μm polystyrene bead trapped at the same trap positions before, confirming that the measured force could be reproduced independently of the trap position. The standard deviation was found 0.6%.

4.2.2. Collecting lens optical transmittance

Even when the instrument is correctly set and the sample is kept within a safe margin of positions, there is a second problem that needs to be compensated for. The high-NA lenses used in microscopy show a non-uniform transmittance. In optical trapping, this has been discussed for the computation of the total power at the sample [96] and to obtain accurate simulations of the optical forces [97]. Here, we explored its effect in light momentum detection.

Due to the angular dependence of the Fresnel coefficients, transmittance through a lens is not uniform. In general, this effect is negligible but, for high-NA optics, the difference between marginal rays and those propagating close to the optical axis can be large, which gives rise to a non-uniform transmittance of the beam (Fig. 4.11a)[5].

---

[5]We kindly acknowledge F. Marsà and A. Farré for providing the high-NA lens transmittance
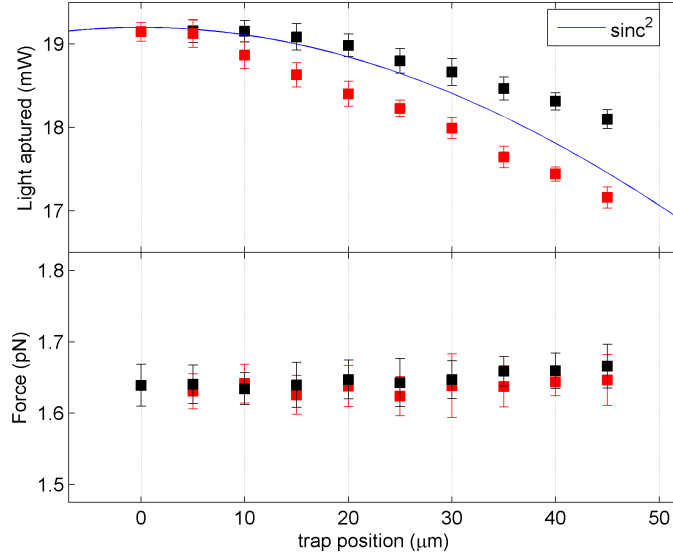
Figure 4.10.: Top - Light intensity captured for an empty trap at different positions from the center, which overlaps with the sinc² modulation originating from the SLM pixel structure. Bottom - Force measured on a 3.00-μm PS bead in a medium flowing at 60 μm/s trapped at the same positions above. The black and red symbols show results from the trap steered perpendicularly and parallel to the flow, respectively.

To emulate the effect of the non-uniform transmittance of the collecting lens, we used a polynomial fitting of the following form, which is similar to that used by M. Mahamdeh *et al.* for an NA = 1.3, oil-immersion objective [97]:

$$T_s\left(\theta\right) = T_s^{(0)} + b_s \sin^2 \theta + c_s \sin^{14} \theta \tag{4.6a}$$

$$T_p\left(\theta\right) = T_p^{(0)} + b_p \sin^8 \theta + c_p \sin^{12} \theta \tag{4.6b}$$

According to the polarization used in our experiments, we took $T_s\left(\theta\right)$ and calculated the integral of the momentum balance:

$$F_{\mathrm{x}} = \frac{n}{c} \iint_{2\pi} T_s\left(\theta\right) I\left(\Omega\right) \sin\theta \cos\phi \, \mathrm{d}\Omega \tag{4.7}$$

Results are shown in Figs. 4.11c-f for the common set of four PS microspheres. Simulations predict an average error (mean ± s.d.) of $\Delta F = -8.9 \pm 2.6\,\%$. For the case of ideal, uniform transmittance, and only accounting for back-scattered light

---

profile measurement.
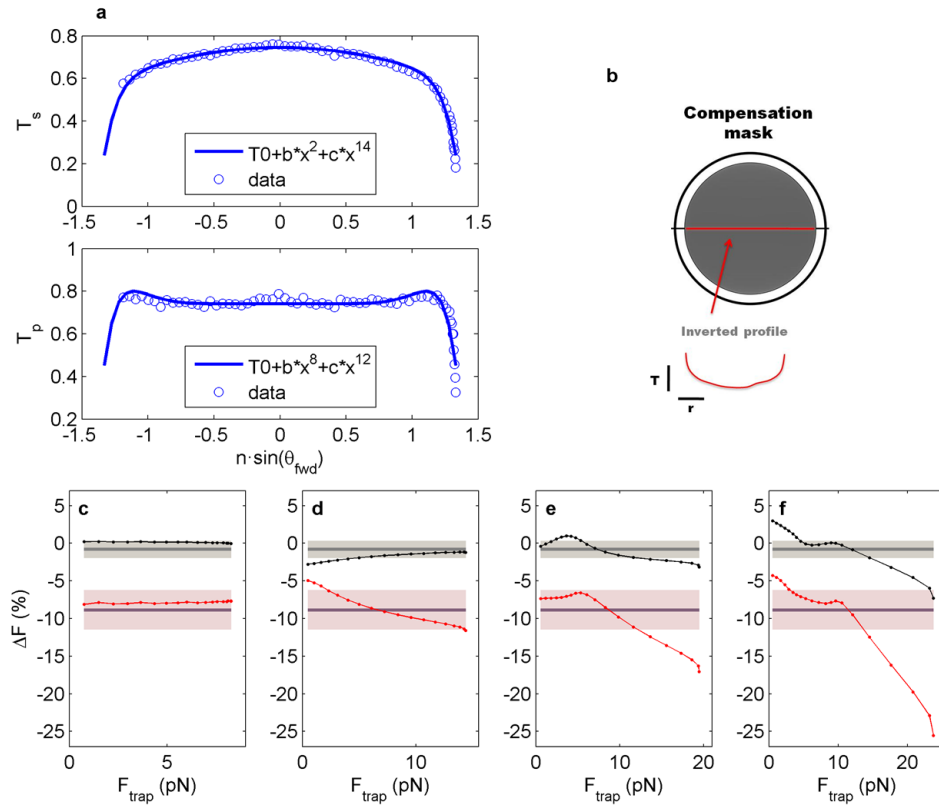
Figure 4.11.: Simulation of the effect from non-uniform transmittance profile. (**a**) Collecting lens transmittance profile for s (top) and p (bottom) polarizations. Circles are experimental data and the curves are the fits from Eqs. 4.6. (b) Scheme of the compensation mask with an inverted transmittance profile. Simulations accounting for the non-uniform transmittance effect are shown in red for 0.61-µm (**c**), 1.16-µm (**d**), 1.87-µm (**e**) and 3.00-µm (**f**) PS microspheres. The shadowed area shows the standard deviations of the measurement errors. Similarly in black for an ideal, uniform transmittance.

loss, we obtain $\Delta F = -0.8 \pm 1.2\,\%$. In other words, the non-uniform transmittance results in a $+8.9\%$ deviation for α_{trap} with respect to $\alpha_{detector}$, while its reproducibility (calibration invariance in light momentum detection) is of $\pm 2.6\%$. Differently, uniform transmittance, leading to the only deviation produced by backscattering, predicted α_{trap} to be closer to $\alpha_{detector}$ and more insensitive over samples of different size.

The non-uniform transmittance can be corrected by use of a compensation mask with an inverted transmittance profile (Fig. 4.11b). Our force detection instrument (Lunam T-40i, Impetux Optics, Spain) includes this possibility, hence the effect of correcting for this can by analyzed as well experimentally.

Nominal calibration of the force detection instrument was performed by the manufacturer in the presence of the compensation mask, which defines ψ according to a uniform transmittance profile. When this is removed to assess the effect of the non-uniform transmittance, $\alpha_{detector}$ modifies according to the new value for ψ. How to measure it through a non-uniform transmittance is unclear, because the power responsivity of the instrument, $S_{SUM} = \psi\,P_{trap}$, will thereby be dependent on the angle of propagation. Considering the laser beam with no sample trapped, a mean value was determined by taking average power values through S_{SUM} as $\psi' = S'_{SUM}/S_{SUM}\,\psi$. Yet we obtained a certain average deviation for α_{trap}, for the overall set of beads, with respect to $\alpha'_{detector} = R_D/\psi' f' c$. We therefore suggest, as discussed in Section 4.4, that a global correction optimizing for $\alpha_{detector}$ to be closer to α_{trap} can be implemented. As shown in the example in Fig. 4.12, $\alpha'_{detector}$ can differ by 5% on average from α_{trap}.
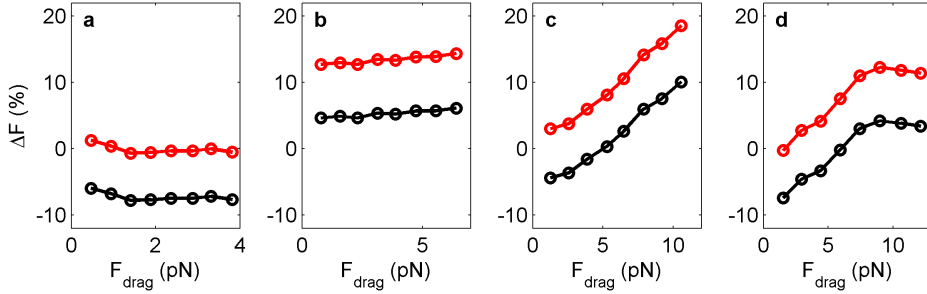
Figure 4.12.: $\alpha_{detector}$ scaling. Measurements on 0.61-μm (**a**), 1.16-μm (**b**), 1.87-μm (**c**) and 3.00-μm (**d**) obtained from $\alpha'_{detector} = R_D/\psi' f' c$ (red) and from scaling to overall α_{trap} (black).

We performed three series of measurements for the four set of PS microbeads. Drag force measurements show a standard deviation of $\pm 7.2\,\%$ when the collecting lens transmittance was not compensated (Fig. 4.13a-d). This result is substantially higher than the $\pm 2.6\%$ variation observed in simulations in Fig. 4.11c-f. Inaccuracy in the modeling of the scattered beam transmitted through the non-uniform transmittance profile can account for that.
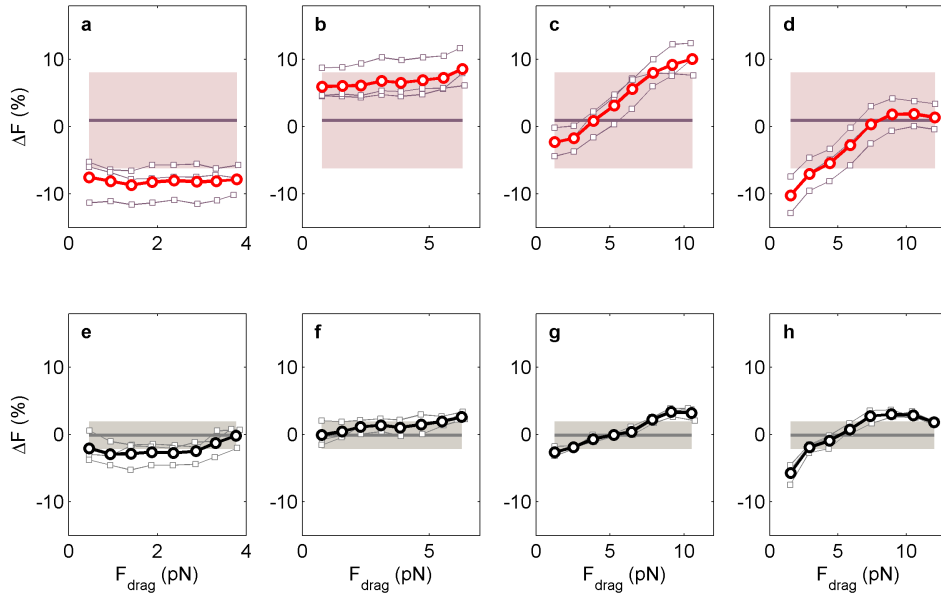
Figure 4.13.: Three series of drag force measurements with and without compensating the non-uniform transmittance of the collecting lens. Averaged measurements on 0.61-μm (**a** – not compensated, **e** – compensated), 1.16-μm (**b** – not compensated, **f** – compensated), 1.87-μm (**c** – not compensated, **g** – compensated) and 3.00-μm (**d** – not compensated, **h** – compensated) PS microspheres.

The most visible effect is that measurement inaccuracy is different for each kind of microbead. Although 0.61-μm and 1.16-μm beads have flat responses, they show errors differing by 15%. In other words, α_{trap} calibration will be more than 15% different between these beads. More importantly, the same bead (1.87-μm and 3.00-μm ones) show different errors depending on the drag force applied, resulting in non-unique α_{trap}, which can vary up to 10% in the whole tapping range.

There is a notable improve in force measurements when the collecting lens transmittance is corrected for (Fig. 4.13e-h). In this case, measurement errors exhibit a standard deviation of $\pm 2.1\,\%$ and maximum deviations, peak-to-peak of $\pm 5\%$. This result is close to that obtained from simulations (Fig. 4.11c-f), which now accounted only for the effect of not capturing back-scattered light. From a numerical $\pm 1.2\%$ deviation in calibrating α_{trap}, we observed an experimental $\pm 2.1\%$ deviation, obtained from accurate drag forces, with respect to $\alpha_{detector}$.

4.3. Back-scattered light loss

After correcting for the effects worsening the detection of the forward-scattered contribution to light momentum (conditions 1: positioning of the force detection instrument; and 2: collecting lens transmittance), we finally need to prove that light is mostly scattered forward and that the contribution of backscattered light to the total momentum is negligible (condition 3).

The amount of light scattered backwards in single-beam optical tweezers is known to be small in several cases of practical interest, such as spherical beads and microcylinders [20, 69]. However, we consider that a systematic study of its effect on force measurements accuracy is still needed. In fact, although low backscattering is partly indicating that the error in momentum measurements will be small, one needs to specifically determine the amount of momentum information lost alongside missing photons. According to our forward-based capture performance, the question we want to address is not only the amount of light missing detection (Eq. 4.8a), but also to what extent the momentum integral over a half sphere coincides with that over the entire solid angle (Eq. 4.8b):

$$P = \oint I\left(\Omega\right) \, \mathrm{d}\Omega \simeq \iint\limits_{2\pi,fwd} I\left(\Omega\right) \, \mathrm{d}\Omega \tag{4.8a}$$

$$F_x = \frac{n}{c} \oint I\left(\Omega\right) \sin\theta \cos\phi \, \mathrm{d}\Omega \simeq \frac{n}{c} \iint\limits_{2\pi,fwd} I\left(\Omega\right) \sin\theta \cos\phi \, \mathrm{d}\Omega \tag{4.8b}$$

From computer simulations, we can obtain a qualitative analysis of the different situations (Fig. 4.14). For dielectric particles, most of the light is always scattered in the forward direction, and shows up as a deflection of the laser beam, pointing towards the same direction of the external force, F_{ext}. Nonetheless, the scattering process is, in general, complex, and a fraction of the light may be also reemitted in the opposite direction of the force or in the backward direction, either in the direction of the force or opposite to it. Light missing detection will result in different errors in the force measured. In general, if light backscattered points towards the direction of the force, the measurement will be underestimated. On the other hand, if light backscattered points to the opposite direction, force measured will be greater than F_{ext}.

This illustrates that the recorded laser power cannot be used as an indicator of the quality of force measurements. The disconnection between light intensity and the direction of propagation brings about that here is no control of the error in the force unless it can be tested against a known value.

In the next sections, we show that the inaccuracy in momentum measurements can be reliably predicted from an FDTD-based scheme that considers splitting of
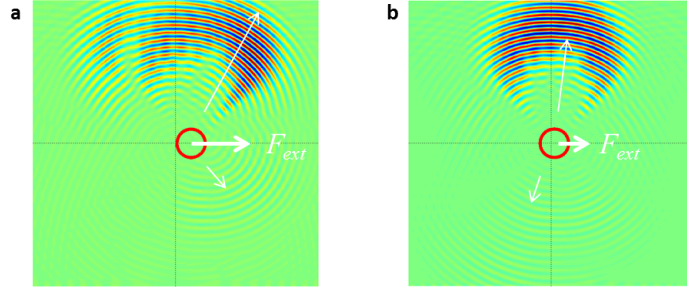
Figure 4.14.: Backscattering contribution to momentum. (**a**) A 3.00-μm PS bead at the escape force position produces backscattering pointing towards the external force, eventually producing an underestimation in the measurement. (**b**) Differently, in an intermediate position, force will be overestimated due to the backscattering component pointing against the external force.

light scattered forward and backward (light loss). For a series of microspheres of different sizes and materials, simulations are compared with force and backscattering experimental profiles based on AOD fast stepping of the optical trap, which proves to yield trap stiffness calibration in coincidence with that from power spectrum analysis. Theoretical errors from simulations are finally observed to coincide in magnitude with momentum-based measurements of Stokes forces, thus making forward-backward splitting of trapping light scattering a good estimator for the measurement accuracy.

4.3.1. Analysis from simulations

Finite difference time domain (FDTD) computation provides useful insights into the behavior of fields in optical trapping [11, 41, 42]. Once the field distribution is known, optical forces are typically obtained by integrating the Maxwell stress tensor (MST) over a surface surrounding the particle. If such surface is located in the far field, the calculation is reduced to integration of the Poynting vector [43], i.e. the angular distribution of beam intensity. The amount of light missing the force detection set-up can be computed as follows:

$$p^{(fwd)} = \frac{n}{c} \int_0^{2\pi} d\phi \int_0^{\pi/2} I(\theta, \phi) \sin\theta d\theta \tag{4.9a}$$

$$p^{(bck)} = \frac{n}{c} \int_0^{2\pi} d\phi \int_{\pi/2}^{\pi} I(\theta, \phi) \sin\theta d\theta \tag{4.9b}$$

where the total trapping power is $P = p^{(fwd)} + p^{(bck)}$, being $p^{(fwd,bck)}$ the power corresponding to light propagating forward and backward after scattering, respectively.

Similarly, we can emulate the precision of lateral force measurements by splitting the forward- and backward-scattered light momentum contribution:

$$f_x^{(fwd)} = \frac{n}{c} \int_0^{2\pi} \mathrm{d}\phi \int_0^{\pi/2} I(\theta, \phi) \sin\theta \cos\phi \, \sin\theta \mathrm{d}\theta \tag{4.10a}$$

$$f_x^{(bck)} = \frac{n}{c} \int_0^{2\pi} \mathrm{d}\phi \int_{\pi/2}^{\pi} I(\theta, \phi) \sin\theta \cos\phi \, \sin\theta \mathrm{d}\theta \tag{4.10b}$$

Here, the total optical force is $F_x = f_x^{(fwd)} + f_x^{(bck)}$, where $f_x^{(fwd,bck)}$ is the force exerted by forward- and backward-scattered photons. As commented before, for accurate light momentum measurement in single-beam optical tweezers, not only do we need to confirm that $p^{(bck)}$ is negligible, but also that so is the momentum carried by the term $f_x^{(bck)}$. To this end, we made use of the Optical Tweezers package from Lumerical's FDTD Solutions to solve the optical trapping problem on microspheres of different sizes and materials and computed the light distribution in the far field by means of the Near to Far Field Projection function. Simulations were performed in 2D for faster computing speed and were proved to yield proper results in accordance with other optical trapping simulation software schemes (Section 2.1.1).

An instantaneous screenshot of the field scattered by a spherical particle out of the equilibrium position is pictured in Fig. 4.15a (diameter $D = 3.00\,\mu$m, refractive index $n = 1.57$, particle position $x_{trap} = 1.5\,\mu$m). A close observation to the angular distribution of light intensity in Fig. 4.15b makes us notice a non-zero momentum contribution to the optical force arising from back-scattered light, leading to an eventual error of $-f_x^{(bck)}$ to the force measurement (Fig. 4.15c).

An example for the optical force split into the contributions to trapping light momentum arising from forward ($f_x^{(fwd)}$) and backward ($f_x^{(bck)}$) scattering appears in Fig. 4.15c. The measurement error, $-f_x^{(bck)}$, indicated for the worst case ($x_{trap} = D/2$) in this specific set of parameters, will be generally different at every trap position. Similarly, the amount of light propagating forward after trapping –and thereby ideally captured by the detection set-up-, $p^{(fwd)}$, depends on x_{trap}. For the $D = 3.00\,\mu$m example shown, light captured is minimal at $x_{trap} \sim D/2$, which is characteristic for bead radii larger than the wavelength (Fig. 4.15d), as discussed below.

4.3.2. Experiments

Together with the simulations, that a certain amount of light does not reach the detector can be evidenced experimentally. A straightforward check, consisting in measuring the light power captured by the detector with and without a trapped particle has been shown in [19]. Such measurement does not account for the fact that the amount of light backscattered, $p^{(bck)}$, and thereby the corresponding lost
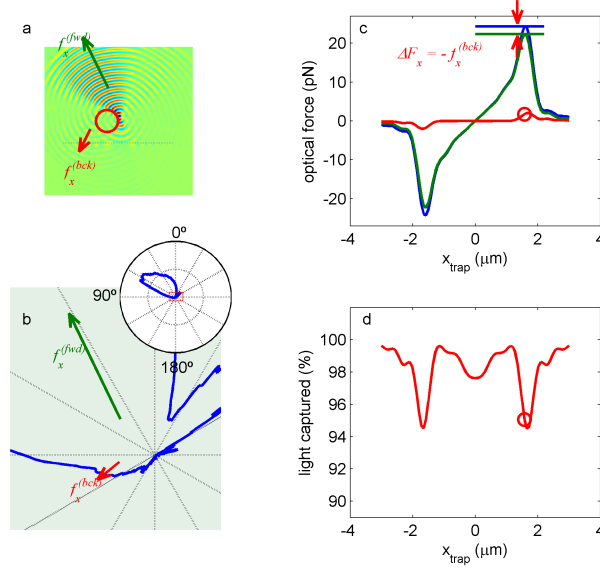
Figure 4.15.: (**a**) Instantaneous E field as a focusing, NA = 1.2 Gaussian beam pulse goes past a trapped 3.00-µm bead with $n = 1.57$, indicated by the red circle. (**b**) Angular distribution of the outgoing intensity in the far field. Forward (backward) contributions to momentum are represented by green (red) arrows (not to scale). (**c**) Optical force (F_x, blue), split into the forward ($f_x^{(fwd)}$, green) and backward ($f_x^{(bck)}$, red) contributions, as the bead is displaced laterally from the trap center. (**d**) Percentage of light captured, $p^{(fwd)}$, in the simulation in **c**. The red circle indicates the trap position in **a** and **b**.

force, $f_x^{(bck)}$, varies depending on the trapping force, i.e. the bead position with respect to the trap. In order to study the effect of $p^{(bck)}$ on force measurements, the complete force profile is measured in real time under the scheme presented in Fig. 4.16a.

The implementation of AODs on the experimental setup allows us to rapidly change the trap position, much faster than the response time of the trapped objects. This principle can be used to rapidly time-share the focus spot over a series of positions and create an effectively static series of multiple traps [7]. Similarly, one can steer the trap over a particle to assess the detection signal and determine, for example, the volt-to-nm conversion factor [52].

Here, AOD modulation is used to obtain the complete force profile by rapidly scanning the microsphere while trapped. The scanning strategy consists on two time-shared traps (at 15kHz), one of them is placed at the equilibrium position ($x_{trap} = 0$) for 0.6 ms (10 clock cycles) and the other one is swept over the scanning direction, staying 66 µs (1 clock cycle) at each position, thereby obtaining a force value each time the trap is changed. This timeframe ensures proper charging response for the PSD and the bead being virtually static at $x = 0$ (at 10-mW trapping power). Pre-
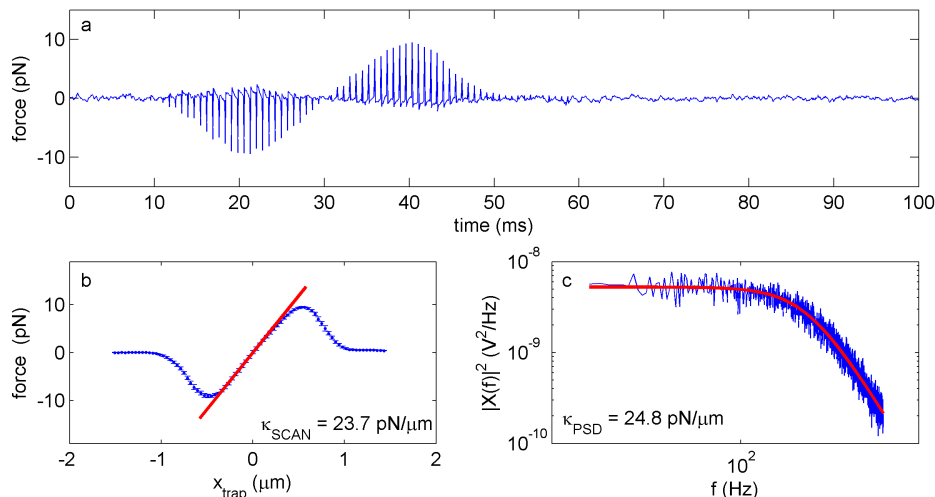
Figure 4.16.: (**a**) Typical signal obtained from the fast stepping scheme over a 1.16-µm PS bead (see text). (**b**) Mean (±s.d) force profile obtained from a series of $N = 50$ measurements performed as in **a**, from which the trapping stiffness is obtained in the linear regime, i.e around $x = 0$. (**c**) Lorentzian fit to the power spectrum.

cise synchronization of the RF signal with the force-detection instrument is carried out by means of a trigger signal via the NI-DAQ acquisition card.

Passive detection signals (1s long) are monitored after each stepping cycle is recorded in order to validate trap stiffness calibration from stepping (Fig. 4.16b) with power spectrum analysis (Fig. 4.16c) [94]. A set of 50 consecutive measurements are performed for each bead. The agreement between the stiffness measured from the force profile around $x = 0$ and the power spectrum fitting constitutes an additional confirmation of the step-profiling scheme used in the following results.

4.3.3. Analysis over samples of different size and refractive index

We next discuss the force and power profiles obtained experimentally ($\alpha_{detector} S_x$, $^1/_\psi S_{SUM}$) and through the simulations schemed above ($f_x^{(fwd)}$, $p^{(fwd)}$). First, a comparison between the profiles on microspheres of similar size and different refractive indices is presented. We used 2.32-µm silica ($n = 1.45$), 1.87-µm polystyrene (PS, $n = 1.57$) and 2.19-µm melamine resin (MR, $n = 1.68$) microbeads.

In Fig. 4.17a, we show the three experimental force profiles obtained, which exhibit the double slope (double stiffness) typical for beads approaching the geometrical optics regime. As expected from the considerably lower refractive index, silica microspheres experience much smaller optical force throughout the whole scan. The

three beads used exhibit light loss maximums at $x_{trap} \sim \pm D/2$ (Fig. 4.17b), though little leak is observed for the silica beads, which is as well understandable according to their low refractive index. In Fig. 4.17c-d, simulations of $f_x^{(fwd)}$ and $p^{(fwd)}$ are shown. The qualitative behavior of both the backscattering and the force profiles is clearly reproduced. MR and PS beads exhibit equal force in the linear regime, while silica beads behave with substantially lower trapping force. The two light loss peaks at $\pm D/2$ are as well reproduced, although experimental results for PS show much greater light loss than simulations. Meanwhile, the higher and lower backscattering, for MR and silica respectively, is likewise observed.
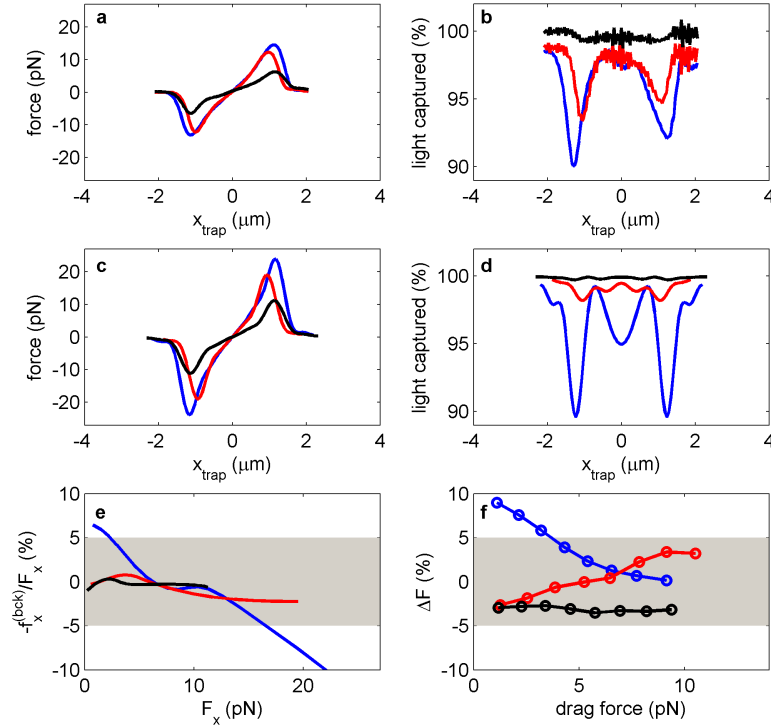
Figure 4.17.: (**a**,**b**) Force and backscattering profiles obtained from the S_x and S_{SUM} signals, measured by fast stepping the AOD-steered tweezers over silica (black), PS (red) and MR (blue) beads. (**c**,**d**) $f_x^{(fwd)}$ and $p^{(fwd)}$ curves simulated for the same series of beads. (**e**) Normalized measurement error emulated from simulations, $-f_x^{(bck)}/F_x$, against the theoretical force obtained from the whole 4π solid angle integral. (**f**) Measurement errors with respect to Stokes-drag calibration over the same series of beads.

The theoretical error for the three beads, $-f_x^{(bck)}$, normalized to the total momentum, is shown in Fig. 4.17e. Since force measurements are limited to the stable trapping range, we plot this figure up to the escape force. Interestingly, light loss does not straightly imply that forward momentum measurements will underestimate

optical forces. Yet we can observe, especially for the MR case at low forces, that the force measurement can be 7% greater than the theoretical value. Near the escape force, MR beads exhibit errors as high as –10% as the trap approaches the escape force position. Apart from this case, which is particularly extreme due to such high refractive index, the error can reach, at most, $\pm 1\%$ for silica beads or $\pm 2\%$ for PS beads.

Errors in force measurements can be assessed experimentally by comparing them to Stokes-drag forces. In a static trap, the trapped samples were applied calibrated constant flows at increasing values up to the escape velocity. In Fig. 4.17f, see the measurement deviation with respect to the theoretical values. For the three beads, note that escape forces are smaller than those obtained in the fast-stepping experiments (Fig. 4.17a) and simulations (Fig. 4.17c,e), according to the dragged bead undergoing a curved trajectory [59]. Stokes forces are measured within a $\pm 5\%$ uncertainty range if we disregard some particular positions for the highest refractive index –and hence strongly-scattering-, MR beads. A similar margin is obtained from considering the backscattering-induced error in Fig 4.17e.

Our next analysis is focused on the role of the particle size in the precision of momentum measurements accounting for backscattered light omission. In this case, we used PS microspheres sized 0.61 μm, 1.16 μm, 1.87 μm and 3.00 μm in diameter, respectively. Analogous to the previous result, we can first observe the experimental force profiles in Fig. 4.18a, which now interestingly show the transition between Rayleigh-behaved particles (0.61 μm) and the geometrical optics regime (3.00 μm). The chief difference is, as widely studied by the optical trapping community, the exhibition of a double stiffness profile in the latter case, while the former shows a single slope that extends over a larger range in relative length units. Concerning the captured light in Fig. 4.18b, note that small beads present a single centered light loss peak, while large particles show a double peak, as mentioned in the previous experiment, at $x_{trap} \sim \pm D/2$. We can imagine that, under the dipole approximation, a small bead at the trap focus, hence experiencing higher fields, will produce larger amount of scattering. On the other hand, if we consider geometrical optics to describe trapping of larger beads, rays impacting at the edge of the beads will tend to be more internally-reflected according to the Fresnel coefficients, as can be intuited from the $D = 3.00\,\mu$m simulation in Fig. 4.15a.

Fig. 4.18c-d shows the simulation results for $f_x^{(fwd)}$ and $p^{(fwd)}$ for the same series of PS beads. Notice the same change in the behavior of the force and backscattering profiles according to the optical trapping regime. We obtain, for large particles (1.87 μm and 3.00 μm), the two peaks at $\pm D/2$, though it is considerable that experimental light loss is higher. Differently, we observe, for the smallest bead (0.61 μm), a single light loss peak in the trap center, while a certain transition between the two shapes is observed in the 1.16-μm bead profile.

While we had seen, in the refractive index measurement before, that low refractive index was best to minimize light loss and thus maximize force measurement accuracy,
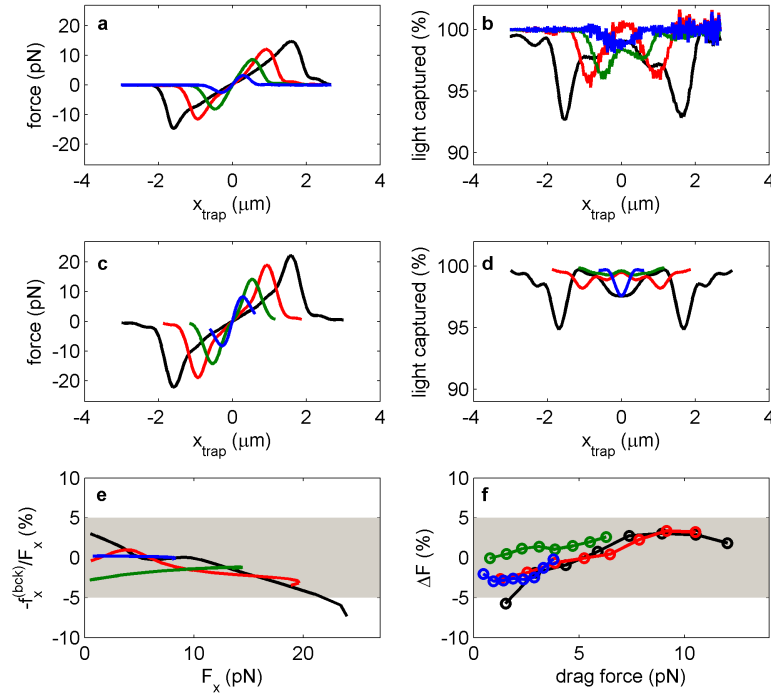
Figure 4.18.: (**a**,**b**) Force and captured light profiles obtained for 0.61-µm (blue), 1.16-µm (green), 1.87-µm (red) and 3.00-µm (black) PS beads. (**c**,**d**) $f_x^{(fwd)}$ and $p^{(fwd)}$ simulated for the same series of beads. (**e**) Normalized measurement error emulated from simulations, $-f_x^{(bck)}/F_x$. (**f**) Measurement errors with respect to Stokes-drag calibration over the same series of beads.

here we find actually null error for the smallest, 0.61-µm beads, and almost constant –2% error for 1.16-µm beads (Fig. 4.18e). Differently, for beads of increasing size, not only does the accuracy worsen, but the error is no longer constant for different bead positions. Nonetheless, it is observed to be, at most, from –4% to 1% for 1.87-µm beads and from –8% to 4% for 3.00-µm beads.

Analogous to Fig. 4.17f, Fig. 4.18f shows experimentally-obtained errors by comparing force measurements with Stokes forces. Qualitatively similar to simulation predictions in Fig. 4.18e, 0.61-µm beads exhibit constant, low deviations, while 1.16-µm beads show a slowly increasing discrepancy. In contrast, the larger, 1.87-µm and 3.00-µm beads show noticeable deviation curves, which differ from those estimated in Fig. 4.18e, but do reproduce the limits to which we can consider an *a priori* accuracy: ±5%. Finally, it is observed to be critical that light loss for large beads can achieve values of 5-10% for ∼2-µm beads (Fig. 4.17b,d) and ∼3-µm beads (Fig. 4.18b,d). It is worth noting though, that the extreme position of $x_{trap} \sim \pm D/2$ is never possible in experiments under equilibrium condition. The experiments here were performed by fast stepping the trap over the bead, which remained static (Fig.

4.16b), whereas real axial equilibrium positions are different at each lateral x_{trap} [59]. This leads to the fact that actual escape forces are much lower than these shown here, from which we can state that light loss will never be that dramatic. In fact, this is in complete accordance with real force measurements, based on Stokes drag, being measured within an accuracy of $\pm 5\%$.

4.3.4. Comment on back-scattered light for trap calibration

Information carried by back-scattered light, lost in most set-ups which perform detection from the posterior part of the optical trap, can as well be used for quantitative studies. For example, intensity of back-scattered light has been demonstrated to provide valuable information on the coalescence and equilibration process of aqueous droplets [98], as well as properties of vesicle lipid bilayers [99].

In a scheme analogous to BFP interferometry (see Section 2.2.1.2), trap calibration for force measurements from backscattering has been demonstrated numerically by G. Volpe *et al.* [100]. Similarly, J. H. G. Huisstede *et al.* [101] demonstrated the capture of the back-scattered light with the same trapping objective to calibrate the optical traps using the power-spectrum method.

On the other hand, in this chapter we have discussed on the possibility to measure beam momentum from capturing light over the forward 2π solid angle. We could therefore believe this disagrees with the fact that back-scattered light can as well be tracked for force detection.

Interestingly, when measuring axial optical forces, the amount of light back-scattered does accurately correlate with the error in force measurements [63]. Being $F_{z,m}$ the measured axial force, the following correction can be implemented:

$$F_z = F_{z,m} + k_p \frac{P_r}{c} \tag{4.11}$$

Here, P_r is the amount of light reflected backwards, which can be measured with a camera imaging the sample plane. k_p is a factor that can be eventually calibrated for a given sample. Eventually, axial force measurements can be performed within 1% accuracy using this approach.

However, we had early stated that the quantity of light lost cannot be considered to be a proper indicator of lateral force measurement accuracy. Differently, back-scattered light can have a neat lateral momentum component considerably larger than the percentage of photons it accounts for. The information from backward photons result in the average $\pm 5\%$ inaccuracy showed before, tested over samples of different sizes and materials.

The point is that this $\pm 5\%$ contribution to force from $f_x^{(bck)}$ arises from deflections in the back-scattered beam, which are related with the sample position within the trap, from which a position-conversion factor β (µm/V) can thereby be obtained.

Nevertheless, this constitutes an eventual calibration approach which uses $2-3\%$ of light and is hence strongly sensitive to the *in situ* experimental features (e.g. sample size and refractive index). Differently, in this chapter we have shown the robustness of the light-momentum invariant calibration over a wide set of samples, which is possible from the optimized collection of the 97-98%, forward-scattered light.

4.4. Conclusion

In this chapter we addressed the technical aspects necessary for absolute light momentum detection in an optimized BFP interferometry system, which directly yields trapping force measurements in optical tweezers. The amount of light collected, above 97% for all the situations analyzed, points out in some degree that trapping forces will be properly measured. However, we have shown that it is necessary to know the exact contribution of back-scattered light to the total momentum. Hence, since there is no prior indicator of the measurement accuracy, calibrated Stokes-drag force has been used as a confident reference to be compared with measurements. For the completeness of the following conclusions, the study has been undertaken over samples of different size and materials.

Erroneous positioning of the light detection instrument has been shown to produce large amount of light loss and fail of the Abbe sine condition. Reproducible positioning of the instrument using an iris conjugated at the sample plane has been confirmed to successfully correct for this effect. Importantly, this has been demonstrated in thick, 500-µm microchambers, used in Chapter 7 for optical trapping in zebrafish embryos. In turn, the high-NA collecting lens has been observed to have a non-uniform transmittance profile. Compensation by use of a mask at the BFP has been as well observed to reduce measurement inaccuracy.

After optimization of the detection of the forward-scattered light, we have dealt with the question of back-scattering as the remaining source of error in single-beam optical tweezers. AOD-based scanning has been useful for determining the trapping force and light loss profiles over the whole trapping range. Simulations of the far-field intensity distribution after scattering have been showed to provide insight in the eventual error caused by omitting the backward contribution.

The limitation due to the backscattering contribution leads to necessarily different α_{trap} calibration depending on the specific features of the experiment, such as particle size and refractive index, and trapping beam characteristics. Different to typical, non-optimized BFP interferometry though, variations have been shown to remain within a maximum $\pm10\%$ margin and $\pm5\%$ for the most common situations –avoiding the use, for example, of high refractive index melamine resin microbeads–.

Light-momentum calibration is determined through Eq. 4.1 by the sensor radius (R_D), the set-up responsivity (ψ, V/mW) and the focal length (f'). These are parameters invariant to the microscopic properties of the experiments. However,

imprecision in the determination of any of these leads to an uncertainty of $\pm 10\%$ in $\alpha_{detector}$ [62]. This is clearly compatible with the average deviation observed in the α_{trap} wide set of calibrations shown. Considering that Stokes-drag calibration is a precise reference in the case of single microspheres used in this work, it is therefore reasonable to use such number of tests to correct for the actual calibration, i.e. forcing $\alpha_{detector} = \alpha_{trap}$. As an example, we did this operation due to the uncertainty in determining ψ when using a collecting lens with a non-uniform transmittance profile (Fig. 4.12).

In Fig. 4.19, we show measurement errors in a variety of situations. In all of them, forces are calculated from positional signals of the PSD (S_x, V) through the macroscopically-determined conversion factor ($\alpha_{detector}$, pN/V). $\pm 5\%$ and $\pm 10\%$ margins are indicated. These involve diverse experimental conditions, which strongly determine trap stiffness (κ, pN/μm) calibration. Contrasted with the subsequent variability of κ, α_{trap} in a light-momentum detection scheme remains invariant within said $5\% - 10\%$, assessed against Stokes-drag calibration.
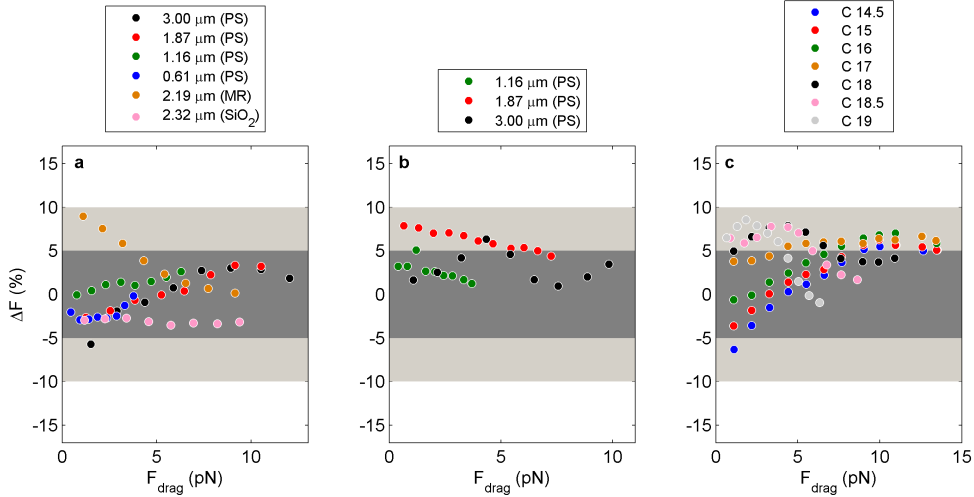
Figure 4.19.: Robustness of absolute light-momentum calibration. (**a**) Different samples trapped with a water-immersion objective. (**b**) Different samples trapped with an oil-immersion objective. (**c**) 3.00-μm PS beads trapped with a water-immersion objective with different degrees of compensation of spherical aberration, i.e. different positions for the correcting collar.

We can therefore conclude that the volt-to-picoNewton conversion is invariant in systems directly detecting light momentum changes due to optical forces in single-beam optical tweezers. We have shown the importance of not only capturing most of the light scattered forward, but as well the need to convey the beam onto a PSD accurately placed at the BFP of a high-NA ($NA > n_m$) aplanatic lens (i.e. fulfilling the Abbe sine condion) with a corrected, uniform transmittance. Deviations caused by the remaining question of backscattering have been determined to be close to

those predicted from the theoretical limit.

5. Force measurements on irregular samples

Optical trapping has become an optimal choice for biological research at the microscale due to its noninvasive performance and accessibility for quantitative studies, especially on the forces involved in biological processes. However, reliable force measurements depend on the calibration of the optical traps, which is different for each experiment and hence requires high control of the local variables, especially of the trapped object geometry. Many biological samples have an elongated, rod-like shape, such as chromosomes, intracellular organelles (e.g., peroxisomes), membrane tubules, certain microalgae, and a wide variety of bacteria and parasites. This type of samples often requires several optical traps to stabilize and orient them in the correct spatial direction, making it more difficult to determine the total force applied.

In this chapter, we manipulate glass[1] (in the 10-µm range, with high slenderness) and zeolite[2] (in the 1-µm range, with small slenderness) microcylinders with holographic optical tweezers and show the accurate measurement of drag forces by the calibration-free direct detection of beam momentum studied in this thesis. The agreement between our results and slender-body hydrodynamic theoretical calculations indicates potential for this force-sensing method in studying protracted, rod-shaped specimens.

Previous to these results, we make use of the holographic-trap layouts introduced in Section 3.3 to manipulate spherical samples, and conclude on the compatibility of object-adapted optical potentials for manipulating extended samples, with light-momentum measurements. Multiple-trap arrays (Section 3.3) will be used to trap sets of multiple beads for which the overall light momentum exchanged accurately fits the total drag force. Cogwheel beam traps (Section 3.4) will be used to trap large microspheres (3 - 8 µm) and demonstrate the measurement of light momentum on non-Gaussian beam traps.

---

[1]We thank J. Ignés-Mullol, from the group of Self-Assembled Materials and Self Organized Complexity, in *Facultat de Química*, from *Universitat de Barcelona*, for kindly providing a series of Nippon Electric Glass (PF50) cylinders.

[2]We thank T. Buscher and A. Studer, from *Westfälische Wilhelms Universität Münster*, for kindly providing a series of zeolite cylinders [71].

5.1. Optical micromanipulation for extended objects

Trap calibration has become routine in force measurement studies involving spherical objects, for which the optical restoring force is well understood [7, 6]. This method can also be applied to non-spherical specimens, with synthetic microbeads bound to the sample of interest used as force probes. This has enabled numerous investigations, such as those into biopolymer stretching [16], the assembly dynamics of microtubules [93], cell membrane mechanics [102] and parasite flagellar forces [14]. However, when it comes to the direct trapping of the sample non-invasively, light momentum transfer gives rise to trapping forces that are difficult to quantify. This, together with complicated hydrodynamic theorizing, makes force calibration for non-spherical samples a complex challenge.

Many microobjects found in nature display cylindrical symmetry, such as rod-shaped *Bacillus* bacteria, *Synedra* and *Nitzschia* diatoms, and eukaryotic nuclear chromosomes. Often, the rod-like shape confers a biological advantage over the spherical form. For example, the larger area to volume ratio of non-spherical mitochondria favors diffusion and makes aerobic respiration more efficient [103]. Likewise, light absorption is maximized in chloroplasts, favoring photosynthesis in plant palisade cells [104]. Direct trapping and measurement of optical forces on rod-shaped specimens is, thus, an important area of interest in several scientific fields.

One solution that is widely applied in bacterial swimming studies consists of monitoring the trapping laser light with a photodiode and inferring information after complex processing of the electric signals obtained. Although not strictly measuring forces, this strategy has successfully shed light on several motility parameters, such as body and flagellar rotation frequencies, velocity variations and direction reversals, cell viability, bacterial swimming patterns and bacterial chemotaxis [105, 106, 107, 108].

For quantitatively measuring trapping forces on microrods and biological rod-shaped samples, several calibration strategies have been developed, whereby force values are obtained from primary variables such as the sample escape velocity or position [8]. Escape velocity measurement, together with the trap power recording, has enabled the assessment of, for instance, trypanosome swimming forces [14] and chromosome motility [30]. Meanwhile, the force-position relationship, i.e. the trap stiffness κ, has been measured for *Escherichia coli* using Stokes' drag force calibration [15] and equipartition theorem [57].

Rod-shaped samples, even if stably trapped in a single Gaussian focus, tend to align their longest dimension with the optical axis due to the gradient force [109], thus remaining in a position that is not always helpful. To manipulate, rotate and orient them in a specific direction, several coordinated optical traps are necessary. Such multi-trap configurations have been modelled by a stiffness matrix whose calibration permit 3D force and torque measurements [110, 111]. Experimentally, the trap stiffness matrix of an elongated diatom trapped with two optical tweezers has been

obtained from thermal motion analysis for force probing purposes [31]. Likewise, synthetic microrods [33] and microdevices inducing complex force fields [32] in a double-trap configuration have been calibrated against Stokes drag. Another technique for stable trapping and orientation of anisotropic samples is the creation of object-adapted optical potentials [90, 29], which can be calibrated for force sensing through back-focal-plane interferometry [91].

In all these cases, precise measurements of the primary variable –escape velocity, trap power or sample position– is of the utmost importance, which, together with the accurate modeling of the sample hydrodynamics [112, 113], is very challenging even for regular microrods. Any deviation from the actual sample shape with respect to the geometry conceptualized, as well as uncertainties regarding model approximations or linear assumptions, will produce large inaccuracies in force measurements.

Direct detection of beam momentum enables force measurements without the need for specific trap calibration, as the force is determined directly from the light momentum exchange between the trapping beam and the sample [19, 20, 21, 67, 63, 71, 72]. Therefore, direct measurement of momentum in non-spherical samples can be performed without complex theoretical calculations. Furthermore, the individual changes in momentum exerted on several optical traps by a sample are added up automatically in the detector, thus directly providing the collective force applied to the trapped object. These advantages come at the cost of complex technical implementation, since all the light creating high-NA optical traps, and therefore contributing to the total momentum exchanged with the sample, must be captured and conveyed to the detector [62]. This is feasible with microbeads and single tweezers, as shown in Refs. [20] and [21], but this certainly cannot be taken for granted for rod-like samples or multiple light foci.

In the next sections, we measured the total drag force exerted on an arbitrary multiple-bead system trapped by several holographic optical tweezers (HOTs). The same Stokes-drag scheme was used to prove the force measurement implementation on microspheres in cogwheel beam optical traps. We then focused on optical manipulation of synthetic microcylinders in a double-trap arrangement and ensured that all the light interacting with the sample was captured. Finally, we compared the drag force measurements with theoretical predictions and discussed the trapping force profiles of dielectric microcylinders.

5.2. Multiple bead systems as early irregular objects

When it comes to measurements on directly-trapped (i.e. with no attached auxiliary microsphere) non-spherical samples, Stokes drag theoretical calculation becomes challenging and can be considerably complex even for cylinders [112]. Here we test beam momentum measurements on a system composed of multiple microspheres, analogous to the verification introduced by G. Thahammer *et al.* for momentum-based axial force measurement in Ref. [63]. For such system, an analytical expression

based on direct addition of individual forces exists and can therefore be used as a reference to which the measurements be compared. In addition, microspheres constitute by far the most used geometry in optical trapping and were the first proved to yield negligible backscattering, a *sine qua non* condition for momentum measurements on single beam optical tweezers [20].

Static trap arrays created holographically are successfully laid over the field of view with sufficient efficiency and can be changed in real time, for instance, to reduce hydrodynamic interaction between microspheres. Importantly, no light loss is appreciable from holographic trap steering over the field of view considered and the force measured is likewise insensitive to the trap position, with a standard deviation of less than 1% (see Section 4.2.1.3).

In the following experiments, multiple-bead systems behave as early irregular objects. Light emerging from all the trap spots is mixed at the back focal plane BFP (Fig. 5.4), thus giving rise to a overall momentum exchange that corresponds to the total drag force applied. It is therefore highly interesting to introduce this result as a proof-of-concept on the possibility to detect light momentum changes on samples with arbitrary shape.

5.2.1. Hydrodynamic interaction

We here explore hydrodynamic interaction as a possible source of error for the theoretical reference used in total drag force measurements. Firstly, we trap two identical 3.00-μm beads and record the total force as a function of the distance between them, D. This will help us choose an interaction-minimized six-bead system geometry, in which force additivity will be secondly checked. It is worth commenting that this verification is carried out on the largest beads used here, ensuring a top-threshold for hydrodynamic interaction for the following experiments.

In Fig. 5.1, we analyze three components for hydrodynamic interaction. First, the interaction between beads separated perpendicular to the exerted flow is measured. As expected, the total drag force equals $2F_{drag}$ when isolated, i.e. $D \to \infty$, and clearly decreases as the beads approach each other. We find less than 5% force drop beyond 20-μm separation. Second, we observe the same asymptotic tendency for the beads placed parallel to the flow, though an evident, stronger force reduction occurs. To make sure this will not modify our theoretical drag force reference, the two three-bead rows (Fig. 5.2c) are transversely shifted. This successfully minimizes hydrodynamic interaction, as shown in our third test. The two beads are separated diagonal to the flow and, similar to the first point, interaction is assessed to be less than 5% as well.

Hydrodynamic coupling between two identical beads has been measured by Crocker through video tracking of their Brownian motion [114]. Compared to the single sphere with drag coefficient $\gamma = 6\pi\eta R$, the two-bead-system drag coefficient is described by four components: two components for the center-of-mass coefficients
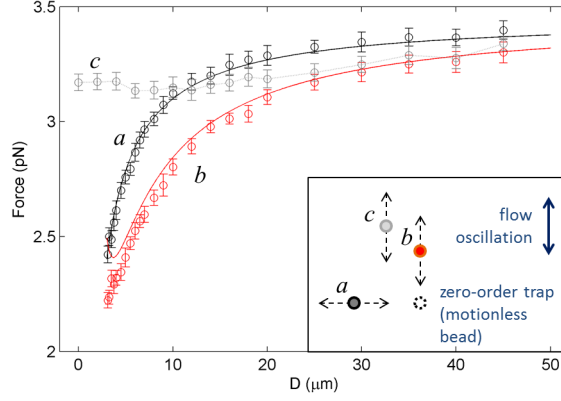
Figure 5.1.: Drag force measured on a 3.00-µm polystyrene bead system at a 60-µm/s flow against the separation distance, D. The theoretical, individual Stokes force is $F_{drag}^{individual} = 1.6\,\text{pN}$. Both traps have a power of 10 mW. The black and red lines show results from the beads separated perpendicularly and parallel to the flow, respectively. Theoretical curves inferred from Ref. [114] are superimposed as continuous lines. ...

and two more for the relative coefficients. Our global force measurement corresponds to the coupled center-of-mass drag force:

$$\gamma_{CM}^{\parallel} = \frac{2\gamma}{1 + \frac{3}{2\rho} - \frac{1}{\rho^3} - \frac{15}{4\rho^4}} \tag{5.1a}$$

$$\gamma_{CM}^{\perp} = \frac{2\gamma}{1 + \frac{3}{4\rho} + \frac{1}{2\rho^3}} \tag{5.1b}$$

These expressions describe with amazing accuracy our experimental results in Fig. 5.1, though a small correction must be considered in relation to momentum-based force measurements. As has been discussed in Chapter 4, a certain deviation exists between ideal lateral forces and measurements of the forward-scattered light momentum, hence the curves from Eqs. 5.1 have been multiplied by 1.065.

From these results we can consider that force is additive for the six-bead system geometry described next. An example for the trapping sequence used is depicted in Fig. 5.2a. As a new bead is trapped in the array, the force increases the amount corresponding to $F_{drag}^{individual}$, in accordance with the fact that the total force is proportional to the number of beads. The descending tendency in Fig. 5.2a-right shows that a certain interaction of 5% still occurs, which is more visible with the trapping of the fourth bead for this specific sequence (Fig. 5.2b). The final geometry of the optical trap array is depicted in Fig. 5.2c.
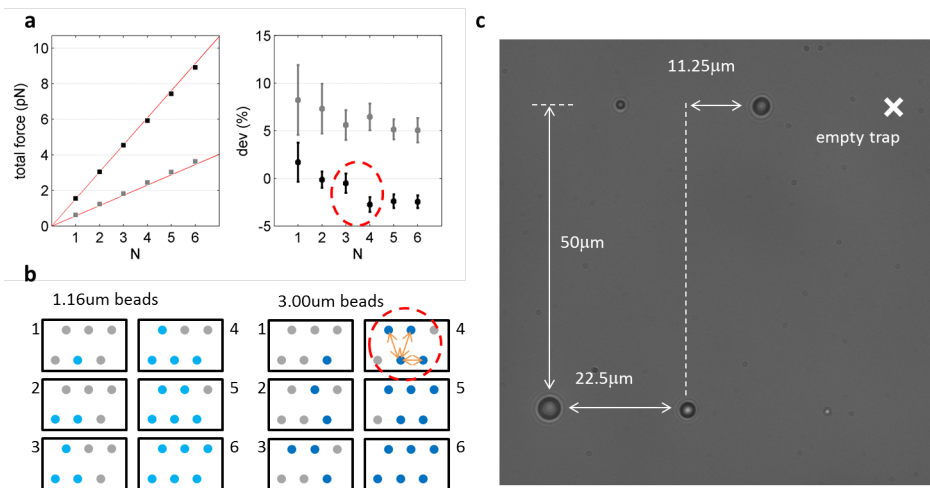
Figure 5.2.: Trapping sequence of six beads in the six-trap holographic array. (**a**) Force measurements on a system of identical 3.00-µm (black) and 1.16-µm (gray) microbeads in a medium flowing at 60 µm/s (left). The red lines correspond to the theoretical drag forces. Force measurement deviation with respect to $N \cdot F_{drag}^{individual}$ (right). (**b**) Sequence in which the different beads were trapped in the array. (**c**) Layout of the six-trap array.

5.2.2. Measurements of global momentum on arbitrary multiple bead systems

The use of microspheres allows the comparison of our direct force measurements with theoretical values derived from adding all the individual Stokes' forces together as follows:

$$F_{total} = \sum_i \frac{6\pi\eta R_i}{1 - \frac{9R_i}{16h} + \left(\frac{R_i}{2h}\right)^3} v \tag{5.2}$$

where R_i are the different radii of the microbeads, v is the flow velocity, η the fluid viscosity whose dependence on temperature is taken into account (Eq. 6.3), and h the distance to the upper surface to include Faxén's effect (Eq. 2.11). In this equation, inter-particle hydrodynamic interactions are not considered and the total drag force on a set of several samples is simply the total sum of single-bead drag forces, according to our previous checking on force additivity (Figs. 5.1 and 5.2).

We performed a similar experiment using the same array of six optical traps, but with microbeads of different sizes and materials. The theoretical drag forces were now different for each type of microbead. The measurements, represented against the theoretical values for twenty-four different combinations of microbeads, settle along a straight line with a slope of one (Fig. 5.3).

These results demonstrate that the light emanating from a set of optical traps can be completely captured and analyzed to determine the total momentum change giv-
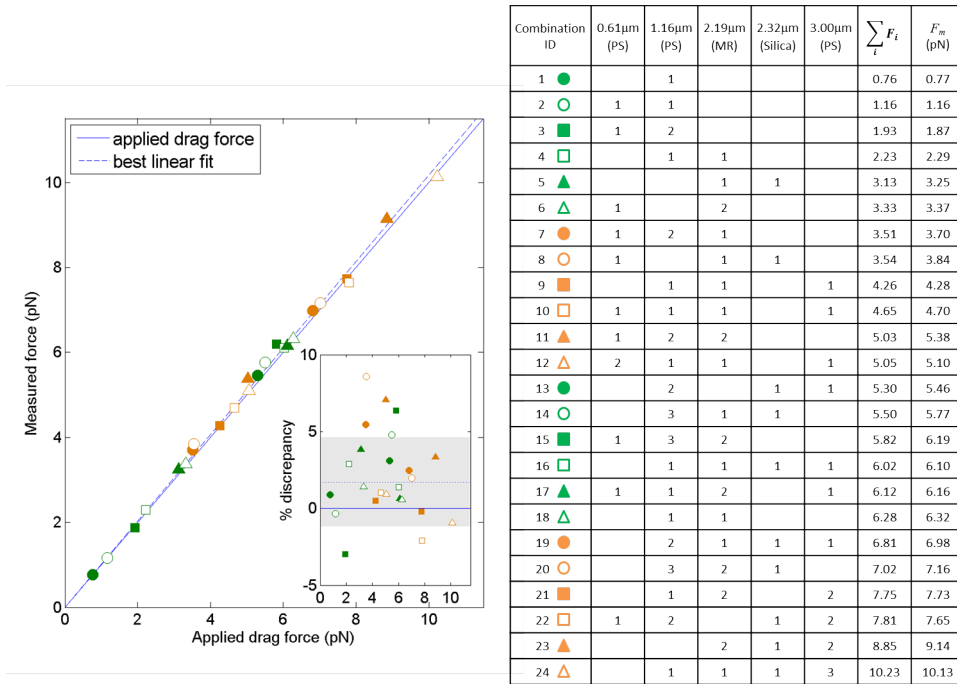
Combination ID	0.61µm (PS)	1.16µm (PS)	2.19µm (MR)	2.32µm (Silica)	3.00µm (PS)	$\sum_i F_i$	F_m (pN)
1 ●		1				0.76	0.77
2 ○	1	1				1.16	1.16
3 ■	1	2				1.93	1.87
4 □		1	1			2.23	2.29
5 ▲			1	1		3.13	3.25
6 △	1		2			3.33	3.37
7 ●	1	2	1			3.51	3.70
8 ○	1		1	1		3.54	3.84
9 ■		1	1		1	4.26	4.28
10 □	1	1	1		1	4.65	4.70
11 ▲	1	2	2			5.03	5.38
12 △	2	1	1		1	5.05	5.10
13 ●		2		1	1	5.30	5.46
14 ○		3	1	1		5.50	5.77
15 ■	1	3	2			5.82	6.19
16 □		1	1	1	1	6.02	6.10
17 ▲	1	1	2		1	6.12	6.16
18 △		1	1			6.28	6.32
19 ●		2	1	1	1	6.81	6.98
20 ○		3	2	1		7.02	7.16
21 ■		1	2		2	7.75	7.73
22 □	1	2		1	2	7.81	7.65
23 ▲			2	1	2	8.85	9.14
24 △		1	1	1	3	10.23	10.13

Figure 5.3.: Measurements on twenty-four combinations of beads immersed in a medium flowing at 80 µm/s. The solid blue line is a curve with a slope of one. The dashed blue line is the best linear fit to the data, with a slope of 1.017 and a normalized root mean square error (NRMSE) of 2.9% (shadowed area in the inset). The table indicates the amount of beads of each kind trapped in the array, as well as theoretical and measured drag forces.

ing rise to trapping forces. The measurement of momentum was not subject to the specific characteristics of the sample under study – bead sizes and refractive indices – but was defined by a persistent macroscopic calibration, represented by the equivalence factor $\alpha_{detector}$. It should be noted that a global optical potential describing each of these situations, from which position measurements could hypothetically lead to indirect force calculations, is non-existent if based on the detection of the trapping laser light. The trapping stiffness corresponding to every bead-trap pair should be calibrated separately, for example, by fitting the power spectrum obtained from high-rate video tracking [46].

Under a certain interpretation, a system of multiple microspheres handled as a whole can also be considered an early irregular object. Light arrives at the detector scattered from different particles at different spatial locations to generate a complicated pattern at the BPF (Fig. 5.4). Moreover, the holographically modulated laser beam focusing at six different positions at the sample plane stops being purely Gaussian, but can still be collected in its entirety and the overall interchange in momentum measured.
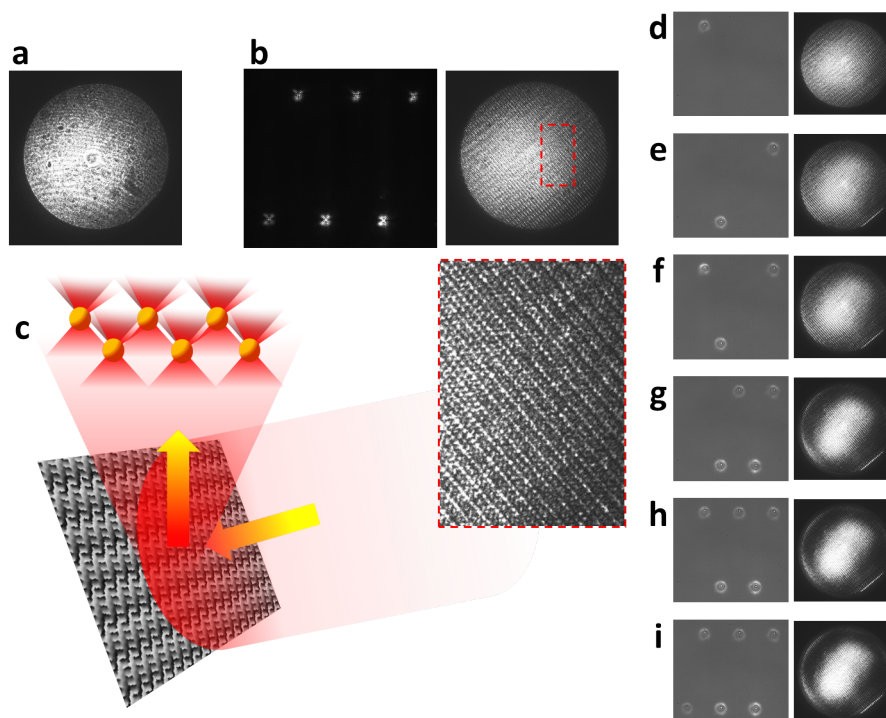
Figure 5.4.: (a) BFP image for a single trap with no bead trapped. (b) Sample
image (traps reflected at coverslip) and BFP image for the six-trap array with
no beads trapped. (c) Holographic scheme generating the six-trap array. (d-i)
Sample and BFP images as one to six beads are trapped in the array.

In Fig. 5.4, we illustrate how the six-spot trapping beam is created through Gerchberg-
Saxton-algorithm hologram (Section 3.3.3) and captured -and finally conveyed to the
PSD- by the force detection system. Beam profile images have been taken with a
CCD camera placed at the BFP (PSD plane). Compared to the single-trap, Gaus-
sian beam case (Fig. 5.4a), in the six-trap situation, a fringe pattern arising from
the complex phase hologram appears, according to this plane being conjugated with
the SLM plane through telescope 2, the microscope objective and the force detection
system (see Figs. 2.4 and 3.1). Despite it being a phase-only hologram, sort of a
Gerchberg-Saxton pattern appears to be visible at the BFP (see Fig. 5.4b - inset
and the discussion in Section 4.2.1).

When sequentially trapping microspheres at the different optical traps, the beam
profile modifies from the Gaussian profile, cropped at NA = 1.2, to the one-microbead
(1.16-µm, polystyrene in this example), in which the NA = 1.32 ring arising from
scattering becomes visible (forward 2π square radians cone). See this effect in Fig.
5.4d-i and compare with Figs. 2.4 and 2.4.

5.3. Force measurements in cogwheel beam optical traps

The next experiment targets the robustness of light-momentum force detection when using exotic, explicitly non-Gaussian beams that might be a need in certain optical trapping situations. As discussed in Chapter 1, there has been an increasing interest on creating structured trapping beams, e.g. in an object-adapted wise, to enhance the possibilities of optical trapping on complex-shaped samples.

Due to the generally complex interaction of the trapping beam with the sample, trap calibration and position detection will deviate from the ideal spring, $F = -\kappa\,x$, and linear BFP interferometry, $x = \beta\,S_x$, approaches. Differently, the $F = \alpha\,S_x$ approach proves consistent with the cogwheel beam traps used here. Again, the same macoscopically-determined $\alpha_{dectector}$ factor yields trapping force measurements that match theoretical drag forces within the same accuracy presented previously (Chapter 4). We use this result to confirm the possibility to implement light-momentum force detection onto non-Gaussian beams, indicating that this is applicable to arbitrary, exotic beams.

As a final result, cogwheel beam trapping force profiles are obtained by sweeping a bead stuck onto the surface over the optical trap. Curiously, a linear region is observed, in which our measurements on trap stiffness are compared with those reported by A. Jesacher *et al.* in Ref. [27].

5.3.1. Drag force measurements on microspheres in a cogwheel beam trap

Within the same strategy used previously, the trapped particles were applied constant drag forces by inducing triangular flows by means of the piezo-electric stage. The square-shaped voltage signals provided by the PSD yield the applied force after the invariant conversion factor $\alpha_{detector}$. Alongside with the Gaussian cases, two cogwheel modes were considered for each bead. For each combination, we applied ten equidistant force values up to the escape force which, in turn, was observed to decrease with higher l-index. As mentioned in Section 3.1, 8.06-µm polymethacrylate (PM) beads were observed to easily stuck to the lower surface after fast sedimenting. For precise force measurements, we tried 3.00-µm and 4.94-µm polystyrene (PS) microbeads. The measured forces are represented against the theoretical values in Figs. 5.5a,c.

As thoroughly discussed in Chapter 4, force measurement deviations are mainly due to light loss through backscattering. The specific shape of the deviation curves shown in Fig. 5.5b,d (left sides), for a given combination of bead and trapping beam, corresponds to the momentum transferred by lost photons. We can notice clear difference with respect to the Gaussian cases mainly due to the strong differences
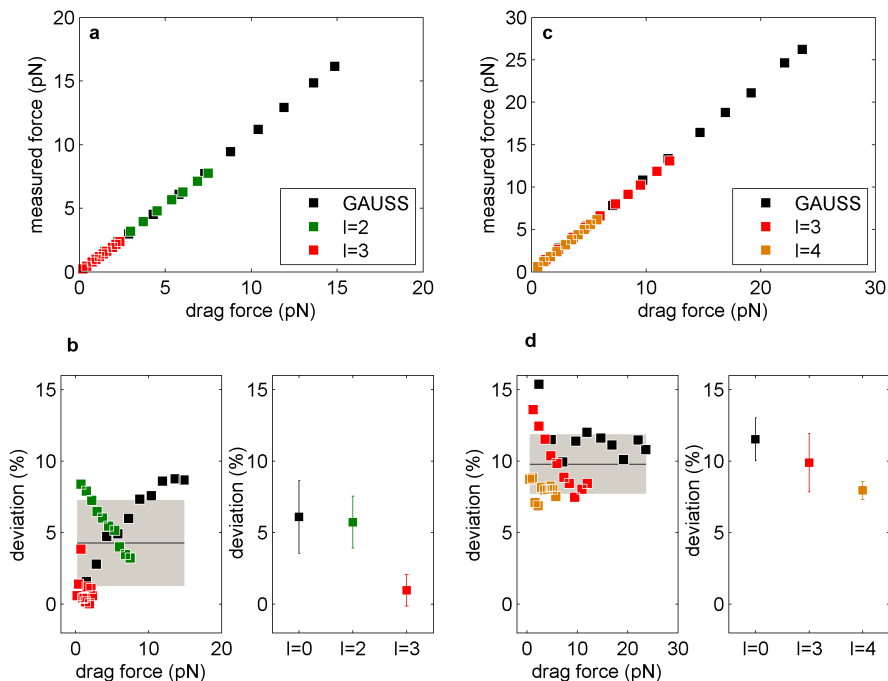
Figure 5.5.: Drag force measurements on microbeads trapped in cogwheel beam optical tweezers. (**a**) Measurements on 3.00-μm PS beads. (**b**) Overall deviations with respect to theoretical drag forces (left side) and deviations for each l mode analyzed (right side). (**c**) and (**d**) show the same results for the 4.96-μm PS bead case.

in the beam structure. Nonetheless, the accuracy for cogwheel beam traps is of the same average magnitude as Gaussian beam traps, which is of high importance bearing in mind that force measurements were obtained from the same volt-to-picoNewton conversion factor, $\alpha_{detector}$. The overall deviation is $+4.3 \pm 3\%$ for the 3.00-μm bead case, which is comparable to that reported in Fig. 4.18. We found higher, $+9.8 \pm 2\%$ average deviation for the 4.94-μm bead case, which might be attributable to such large samples being affected by critical interaction with the surface. Yet theoretical forces were corrected through Faxén's coefficients (Eq. 2.11).

In Section 3.4.1 we described the generation of cogwheel beam traps through wave-front modulation by means of an SLM. Especially when closely observing Fig. 3.11d, one can notice that the beam structure at the BFP is considerably different from the Gaussian beam case. We thereby consider the measurements in Fig. 5.5 a clear proof-of-concept for the accuracy of force measurements through the detection of beam momentum changes in non-Gaussian traps. As we have discussed, capturing all the light interacting with trapped specimens makes possible to implement such calibration-free approach.

5.3.2. Cogwheel beam trapping force profiles

An 8.06-μm PM bead was stuck at the upper surface of the micro-chamber and the force signal was recorded as the piezo-electric stage swept positions continuously. For the cogwheel trapping beams, the force profiles turned out to be linear in a region comparable to that of the Gaussian traps (Fig. 5.6). This makes possible to perform trap stiffness calibration if precise position measurements are possible [27, 115].
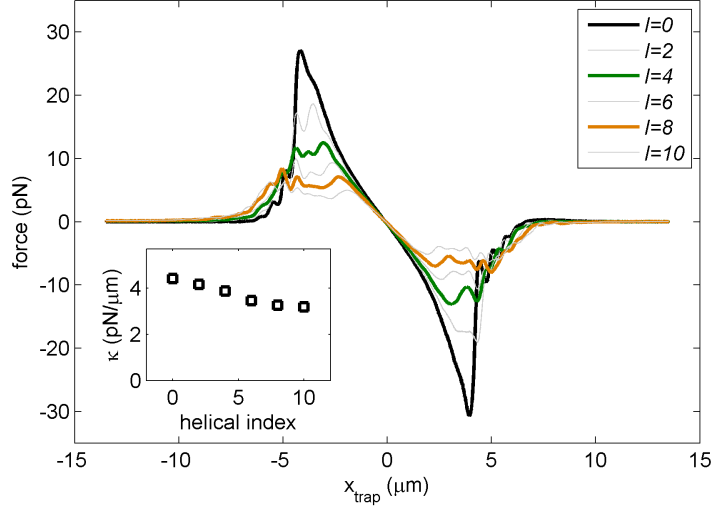

Figure 5.6.: Trapping force profiles on an 8.06-μm bead in a 20-mW cogwheel beam trap with helical index of $l = 0, 2, ..., 10$. In the inset, we plot the trapping stiffness obtained from a linear fit around $x = 0$.

We do observe a decreasing trapping stiffness as the helical index, l, is increased. A. Jesacher *et al.* [27] report that the optical trap stiffness remains constant for a given microbead, regardless of the l-index, if the bead is sized far larger than the ring spot. They suggest that this might be due to the photon momentum being chiefly determined by the numerical aperture of the beam. On the other hand, they specify that smaller beads actually exhibit changes in the stiffness and, eventually, can no longer get trapped, as mentioned in Section 3.4.1.

Both results may be compatible if a list of issues is taken into account. First, our 8.06-μm-sized samples are quite smaller than the 10-μm and 15-μm ones for which they reported constant stiffness. Second, their determining the trap stiffness from trajectory measurements lead to intrinsically noisier measurements. Last and more importantly, our measuring the stiffness on stuck beads does not guarantee the same axial position as in A. Jesacher *et al.*'s set-up due to their actually optically-trapping the samples (axial trapping equilibrium position).

Finally, Fig. 5.6 confirms as well our previous observation that the escape force

decreases with higher l numbers. At an extreme point, the particle would not remain statically in the optical trap.

5.4. Force measurements on microrods

Beam momentum detection can be applied to measure forces on optically trapped cylinders, without the need for previous trap calibration or complete description of the trapping dynamics. As has been discussed in Chapter 4, once the light collecting system has been set up, accurate measurement depends on the capture of all the light interacting with the specimen. In our drag experiments, two traps were required to hold the cylinders on a plane perpendicular to the optical axis [69]. Therefore, we first studied if nearly all the light creating the two traps would leave the sample and penetrate the collecting lens. Positioning the traps far from the optical axis did not produce significant light loss *per se* (Fig. 4.10), leading to the question of whether the particular cylindrical shape contributed to a substantial drop in the captured light due to unfavorable backscattering.

In this section, we start by analyzing optical trapping and force measurements on large glass microcylinders, in the order of tens of microns, with slenderness coefficients, $s = {}^{L}/{2a}$ (L and $2a$ are the cylinder length and diameter, respectively) of approximately 5 - 10. Slender-body hydrodynamic theory [112] describes well the drag forces measured for these samples.

Since the microcylinders were far larger than the laser wavelength (20 to 50 μm in length and 5 μm in width), ray optics was used to describe their interaction with the trapping beam. We used the Optical Tweezers in Geometrical Optics (OTGO) package in Matlab [40], which computes optical trapping forces and torques from a ray-optics perspective. Interestingly, the user can split the beam resulting from the interaction with the sample into rays travelling forwards and backwards, hence providing an immediate means for determining the amount of light captured by our beam momentum detection instrument. For an objective numerical aperture NA = 1.2, more than 97.5% of light propagated towards the positive axial direction, slightly decreasing to 96.4% for NA = 1.3. These results were consistent with our subsequent measurements.

On the other hand, we considered using shorter microcylinders (2 to 6 μm in length and 1 to 3 μm in width) with the aim of extending the conclusion of accurate force measurements to the case of biological samples. For example, *Escherichia coli* bacteria are around 2 to 3 μm in length and 0.5 to 1 μm in diameter [116]. Chromosomes isolated from chinese hamster ovary (CHO) cells are 6 μm in length and 0.5 μm in diameter [30]. Force modeling for these cylinders starts failing for their lower slenderness ($s \sim 2 - 3$), besides the fact that two-trap manipulation requires more careful application of the holograms described in Section 3.3.1. In Ref. [116], P. Y. Liu *et al.* introduce a method to determine the size and refractive index of

a single bacterium. We finally complement our conclusions with their results and others in the literature to envisage that light-momentum detection will be a strong strategy to perform mechanical measurements on rod-shaped biological samples.

5.4.1. Force measurements on 10-μm scale, slender cylinders

We performed a Stokes' drag force experiment for a cylinder trapped in a two-tweezer set-up with a water immersion objective of NA = 1.2, and then with an oil immersion objective of NA = 1.3. Different flow rates were applied until the cylinder escaped from the traps, both along the transverse and longitudinal directions. Experiments were also carried out for both p and s light polarizations. We determined for each applied flow the amount of light collected in sync with the optical force experienced by the cylinder so as to counteract the drag force (Fig. 5.7b,c). Backscattering was observed to account for, at most, 3% of the trapping beam intensity, which was measured by removing the cylinder from the traps to avoid obstruction of the laser beam.

Since the light interacting with the cylinders was almost entirely captured, we expected the beam momentum measurements to accurately coincide with the lateral trapping forces. In Fig. 5.7c, we compare the measured forces with the drag forces applied, which were calculated from slender-body theory [112]:

$$\gamma_\perp = \frac{4\pi\eta L}{\ln\frac{L}{a} + C_1 - \frac{3L}{8h}} \tag{5.3a}$$

$$\gamma_\parallel = \frac{2\pi\eta L}{\ln\frac{L}{a} + C_2 - \frac{3L}{16h}} \tag{5.3b}$$

Here, $\gamma_\perp$ and $\gamma_\parallel$ are the transverse and longitudinal drag coefficients of the cylinder, such that, at flow velocity v, $F = \gamma_{\perp,\parallel} v$. The parameter η is the liquid viscosity, h is the distance to the upper surface, $a = 2.5\,\mu m$ is the cylinder radius and L its length, which were determined by analyzing bright-field images (Section 2.2.1.1). Parameters C_1 and C_2 for slender cylinders are defined as: $C_1 = \ln 2 - 1/2$ and $C_2 = C_1 - 1$.

During the course of these studies, we observed greater variation in force measurements compared to similar experiments with microspheres, which might be attributable to a number of issues. First, most of the cylinders we used had coarse and sharp borders, thus affecting the viscous force. Second, the hydrodynamic model considered assumed high slenderness of the objects under study, which might not be true for the shorter cylinders. Finally, although the cylinders were stably trapped with two optical tweezers, vibration could still occur, thus producing some noise.

We further determined the transverse and longitudinal drag coefficients for a variety of cylinders of different lengths, dividing the force values measured by the applied
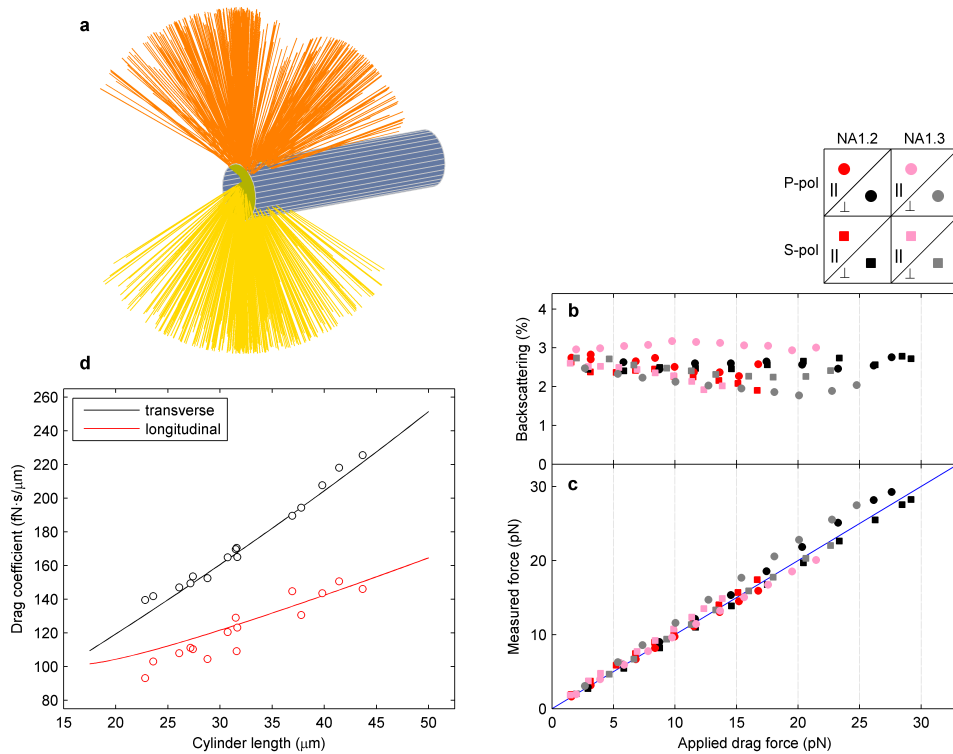
Figure 5.7.: Force measurements on 10-µm scale cylinders. (**a**) Ray optics OTGO modeling of the trapping beam acting on the cylinder edge. (**b**) Light scattered backwards for a 33-µm cylinder trapped with two 20-mW optical tweezers, dragged at several flow velocities up to the escape force. The eight data series correspond to p and s polarizations, water and oil immersion objectives, and transverse and longitudinal drag. (**c**) Forces determined through beam momentum detection over the same data series in **b** matched with theoretical Stokes' values (solid line), with an NRMSE of $\pm 8\%$. (**d**) Longitudinal and transverse drag coefficients determined by force measurements on a variety of cylinders, compared with the theoretical values (NRMSE is $\pm$ 2.6 and $\pm$ 6.6% for transverse and longitudinal drag experiments, respectively).

flow velocity that was now constant for all the samples (Fig. 5.7d). For both directions, our results and theoretical curves overlapped, with a maximum deviation of $\pm 10\%$. It should be noted that, again, the same macroscopically determined conversion factor $\alpha_{detector}$ yielded accurate force values from the signals provided by the PSD.

5.4.2. Force measurements on 1-μm scale, non-slender cylinders

We have carried out drag force measurements on a series of cylinders of sizes from 1 μm to 3 μm in diameter and 2 μm to 6 μm in length. The results, compared to Stokes formulae for slender cylinders, are plotted in Fig. 5.8a, where the horizontal error bars stem from the uncertainty in determining the theoretical Stokes force applied. This error is associated with the uncertainty in determining the cylinder size from bright-field images.

Vertical error bars, calculated from the standard deviation of 20 measurements repeated for each point, were not plotted as they ranged from 20 fN to 50 fN (Section 4.1.1). See the length and diameter distributions of the cylinders used in Fig. 5.8b. While transverse drag measurements remain within a normalized root mean square error (NRMSE) of $\pm 5\%$, longitudinal drag measurements deviate considerably from the theoretical values, especially for cylinders of lower slenderness. In fact, we have found a clear correlation between the deviation from Brennen and Winet's model [112] and the slenderness of the cylinders analyzed (Fig. 5.8c).

We can state, from these results, that light-momentum-based measurements are as well valid for this series of shorter cylinders, yet the use of a Stokes reference fails, especially, for the longitudinal drag case. We envision that a more complex theoretical hydrodynamic description [117] could be used to reinforce the conclusion on force measurement accuracy.

As a second confirmation of the measurement operation, backscattering of the cylinders used here was observed to be $2.1 \pm 0.6\%$, slightly lower than the value obtained for larger cylinders (Fig. 5.7b), hence the beam momentum will be measured with a similar accuracy. The refractive index of biological samples is notably lower, leading to smaller backscattering and making the light momentum measurable from capturing the light scattered in the forward direction.

5.4.3. Optical manipulation of microrods

As has been discussed, elongated objects tend to align parallel to the optical axis when trapped [109], hence some technical tricks need to be undertaken if one needs to manipulate a rod-shaped sample in a perpendicular orientation. S. Chattopadhyay *et al.* [15] reported that *E. coli* bacteria can be stably trapped horizontally if the working plane is set near the coverslip surface or, on the other hand, a constant
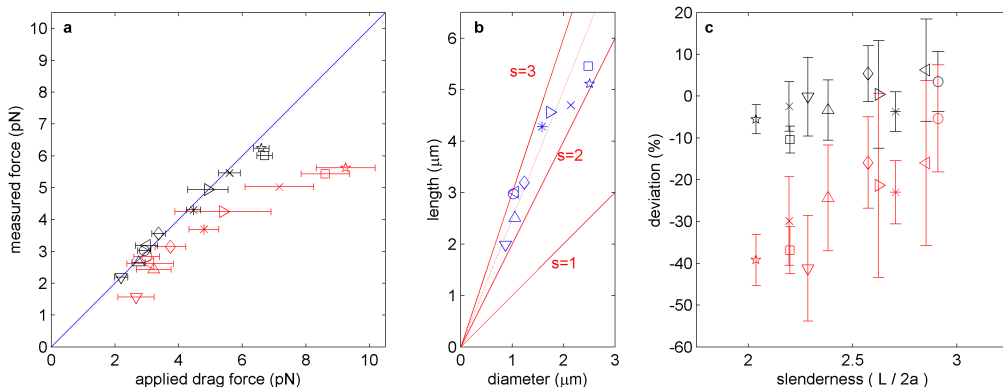
Figure 5.8.: Force measurements on 1-μm scale cylinders. (**a**) Drag forces measured along the transverse (black) and longitudinal (red) directions against theoretical values from slender-body theory [112]. The blue line is a $y = x$ curve. Each symbol corresponds to a different cylinder. (**b**) Length against diameter for the cylinders used (blue symbols) and constant-slenderness curves (in red). (**c**) Deviation from slender-body calculations with respect to the slenderness (s) of the cylinders. Black (red) symbols are transverse (longitudinal) drag measurements.

flow is applied. E. Stellamanns *et al.* [14] used as well a calibrated flow to study propulsion forces of the rod-shaped *Trypanosoma brucei brucei* bateria, whereas N. Khatibzadeh *et al.* [30] used the same approach to calibrate chromosome trapping forces through escape velocity measurements. Differently, only-optical solutions can be applied by considering light shaping. Object-adapted potentials [90, 91] and *tug-of-war* [29] optical tweezers can be used for accurate orientation, as well as multiple-trap systems to trap extended objects [34].

In the experiments shown before, we used a double-trap holographic scheme that permitted stably trapping the two kind of microcylinders. This approach has been used in a number of laboratories [33, 31, 32, 110, 69]. The hologams we used are described in Section 3.3.1 and can be generated in real time to comfortably set the distance between the two traps, D, and the relative power between them.

We next describe some of the optical manipulation properties of the samples used. Large cylinders were tracked from bright-field images with sufficient precision to assess the trapping force profiles and study the effect of different D-values. For the smaller cylinders, less stable trapping was observed, as will be discussed.

5.4.3.1. Manipulation of 10-μm scale microcylinders

For the 10-μm scale glass microcylinders, we noticed that a certain trap power threshold was required to counteract weight. We estimate that a 20-μm long, 5-μm

in diameter microcylinder weighs around 10 pN[3], hence two traps powered above 10-mW were needed for stable trapping, otherwise the microcylinders could not be raised above the chamber surface. In this case, we believe that the two traps were needed to counteract weight torque, rather optical torque, to avoid trapping along the optical axis of one of the traps, i.e. being held by one of the cylinder edges.

Force measurements enabled the assessment of the trapping force profiles, i.e. versus lateral displacement. We determined the longitudinal force profile by combining force detection with position measurements based on video tracking (Section 2.2.1.1). Analogous to the experiments described above, we dragged a given cylinder ($L = 32.7\,\mu\text{m}$) by applying a triangular flow oscillation along its longitudinal axis. Force profiles were determined in two different regimes. First, the distance between the traps was smaller than the cylinder length ($D < L$), so that only one trap exerted an optical force counteracting the drag flow (see Fig. 5.9a). Under this regime, the posterior trap exerts no force unbalancing the restoring force exerted by the anterior trap, hence the microcylinder escape force is higher. Second, the effect arisen from the $D \sim L$ situation was assessed: escape forces were observed to decrease as D approached L ($D \to L$), due to both traps competing towards opposite directions; but, on the other hand, a linear region with increasing trap stiffness appeared.

In the $D < L$ case, consistent with the fact that the optical traps only exert significant longitudinal forces when interacting with the cylinder ends, we recorded a zero-force plateau for displacements smaller than $\Delta x_0 = {}^{(L-D)}/2$ (Fig. 5.9b). The force rapidly increases when the first trap reaches the end of the cylinder. The force profile against the trap position with respect to the cylinder edge, x_{trap}, indicates that the optical force profile is independent of D.

The time force signals are shown in Fig. 5.9c. The top and bottom plateaus correspond to the force exerted by one of the traps on their respective cylinder end, whereas the central plateau (when reducing the distance between the traps) corresponds to the time during which the cylinder slides before its rear edge reaches the other trap. The central plateau coincides with the initial momentum of the beam, confirming that the cylinder is experiencing no trapping force during this time.

In Fig. 5.9b, Δx was calculated as half the difference between the two extreme cylinder positions when being dragged back and forth, in a way analogous to force measurements with respect to the initial beam momentum (Section 4.1.1). These two positions were determined by averaging the corresponding half oscillation period. We then duplicated and used the force measurements to plot the restoring optical force for both positive and negative Δx values. In the inset, the position of the left trap with respect to the left cylinder edge was calculated as $x_{trap} = {}^{(L-D)}/2 - \Delta x$. As shown, the four curves –corresponding to different D values– overlapped after this transformation. This is due to the fact that only one of the optical traps balances the drag flow, since $D < L$, i.e. the posterior trap is in a flat position regarding the cylinder (far from the edge), hence applying no longitudinal force to the cylinder.

---

[3]Glass Micro Rod PF50 density: $2.6{\cdot}10^3\,\text{kg}\,\text{m}^{-3}$ (Nippon Electric Glass).
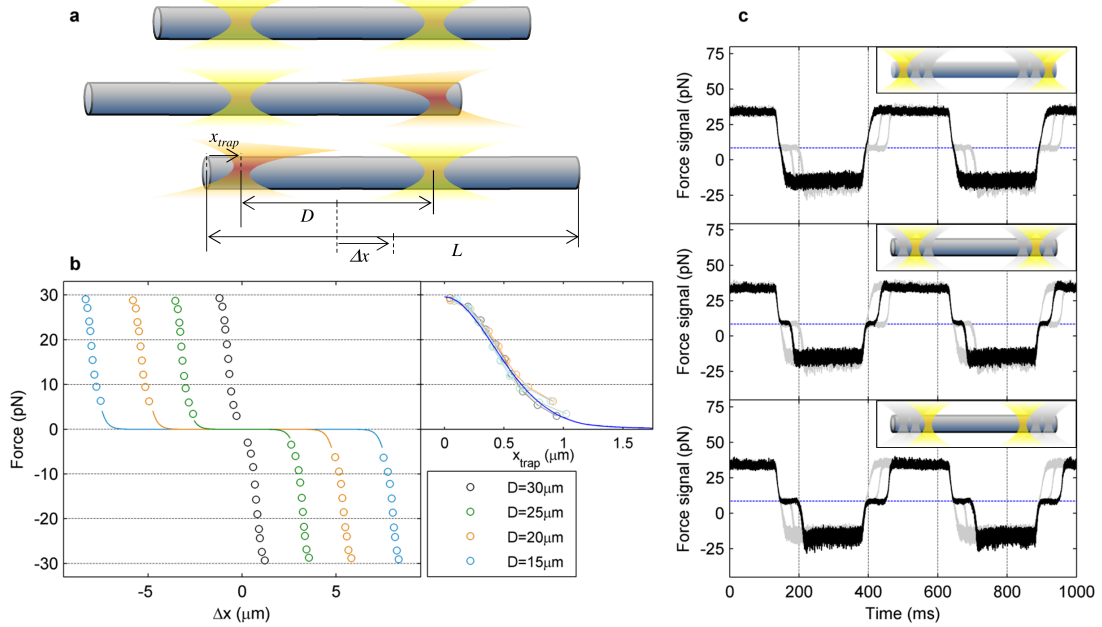
Figure 5.9.: Trapping dynamics of 10-µm scale cylinders. (**a**) Schematic of the trapping dynamics of a cylinder with two holographic optical tweezers. L is the cylinder length; D is the distance between the two traps. The optical traps exert longitudinal forces only (in orange) when they are close to one of the cylinder edges. (**b**) Experimental force-position curves up to the escape force for a cylinder with $L = 32.7\,\mu$m trapped with two 25-mW optical tweezers and different D values. Measured forces are represented against the distance between the cylinder center and the intermediate point between the two traps, Δx. Inset - optical force against the trap position with respect to the cylinder edge, x_{trap}, for the four D values. The blue line is the theoretical momentum balance inferred from ray optics. (**c**) Force signals for $D = 30\,\mu$m (top), $D = 25\,\mu$m (center) and $D = 20\,\mu$m (bottom), for $L = 32.7\,\mu$m. Traces for the other two values of D are also plotted in light gray for comparison. The dashed blue line indicates the initial momentum of the trapping beam.

We next approached the $D \to L$ situation. In Fig. 5.10a, the two traps simultaneously exerting opposite optical forces are schemed. While the anterior trap exerts an optical force pointing against the flow (F_+), the posterior trap does interact with the corresponding microcylinder end and exerts a certain optical force (F_-) favoring the drag force. To counterbalance the drag force, optical forces arising from both traps should fulfill $F_+ - F_- = F_{drag} = \gamma_{\parallel} v_{flow}$, which makes the microcylinder actually having a rapidly-decreasing escape force down to the situation in which it can no longer be stably trapped ($F_+ \sim F_-$), as shown in Fig. 5.10b.

Concerning the force profiles, in Fig. 5.10c we show measurements analogous with those in Fig. 5.9b. Differently, the zero-force plateau disappears and a linear region, $F = -\kappa x$, becomes visible. Importantly, OTGO simulations accurately overlap with the measurements, reinforcing the geometrical optics description of these samples according to their dimensions $L, D \gg \lambda$. Here, the code was modified to include the second optical trap, which was not a need in Fig. 5.9b due to this exerting no force along the cylinder axis[4].
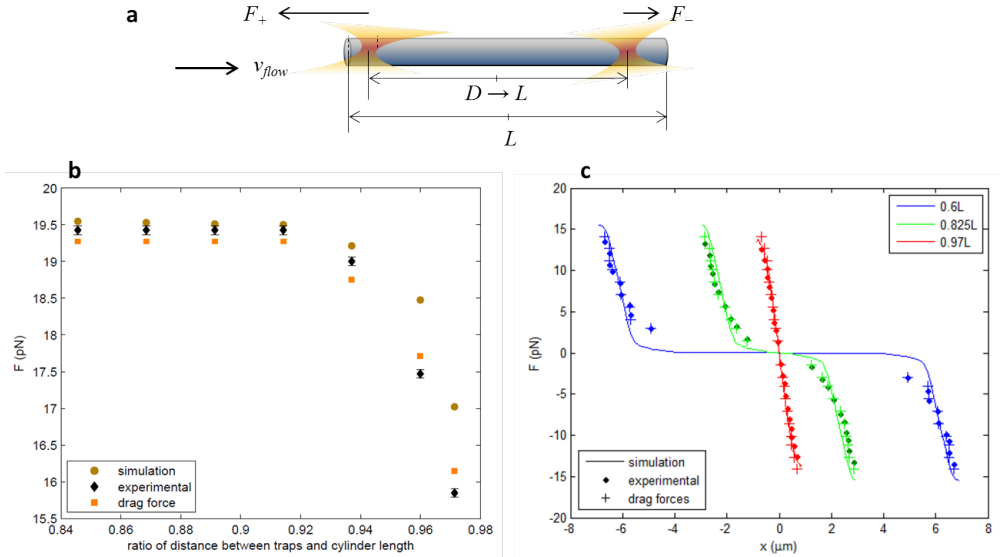

Figure 5.10.: (**a**) See Fig. 5.9a. (**b**) Escape force values versus the distance between the traps, D Experimental results (mean $\pm$ s.d.) match the simulation results computed with the OTGO package and the drag forces applied with the piezostage-induced flow. (**c**) Force profiles for three different D-values. The continuous lines show the theoretical forces computed with OTGO, which again overlap the experimental data and drag forces.

The fact that a linear restoring force appears in this situation (with no zero-force range) could be eventually used for calibrating the trap stiffness for indirect force measurements, such as the methods described in Section 2.2. However, it is worth

---

[4]We thank Neus Allande's for writing the software for the trapping force simulations shown in Fig. 5.10b.

noticing the high variability due to a slight change in D, hence we would rather recommend the escape force method in combination with video tracking.

In either case, regardless of the D value, neither the measured back-and-forth forces nor the initial momentum –corresponding to null force– changed (Fig. 5.9b-c and Fig. 5.10). Therefore, the measured force only depended on the external drag force applied, which was optically counterbalanced regardless of the trapping beam structure. This reinforces the idea that the direct detection of beam momentum facilitates the optimal choice of the trapping beam or multiple-trap arrangement to manipulate a given sample, providing accurate force measurements without the need for previous *in situ* trap calibration. In addition, the non-linear response of the force profile –or the strongly-varying linear response in Fig. 5.10b– did not impede the measurement of optical forces, as they were obtained directly from the detection of changes in the beam momentum.

5.4.3.2. Manipulation of 1-μm scale microcylinders

When trapping the shorter cylinders, in the 1-μm scale, we found that the choice of D became quite critical for horizontal trapping, especially for the shorter ones. Usually, slight changes in D, of tens of nanometers, could eventually lead to unexpected collapse of the microcylinder into one of the traps. Something similar happened at the point the piezostage-induced flow started. To avoid this and ensure horizontal trapping, we assayed trapping over a series of D values, as well as the relative power between the traps through parameter M (Section 3.3.1), and set the most stable configuration. We envision that another solution could be implemented by generating complex force fields, such as those proposed by Bezryadina *et al.* with high transverse momentum transfer [29]. As discussed in Section 5.5, optical force can still be measured through light-momentum detection on non-Gaussian beam traps.

5.4.4. Discussion on the applicability on biological samples

Direct detection of beam momentum differs from other force-sensing methods in optical micromanipulation, in that force measurements can be obtained directly instead of being inferred from an intricate relationship with the position and orientation of the trapped specimen. Thus, this enables accurate force measurements without the need for specific trap calibration or linearity between the position and orientation of the trapped sample and the optical force.

Accurate measurement requires the capture of all the light interacting with the sample; a condition which is fulfilled as long as light losses are negligible. This has been previously demonstrated for micro-spheres trapped on-axis [20], as well as in the present chapter for multiple holographic traps spread over the sample field of view and optical manipulation of cylindrical objects. In the multiple-bead experiment,

we demonstrated that the high-NA collecting lens captured all the light from off-axis traps, and that the force was independent of the trap position. Backscattered light for 10-µm scale, glass cylinders was assessed to be 3% of the incoming light, despite their particular symmetry.

The macroscopic calibration of the set-up, represented by the volt-to-picoNewton parameter $\alpha_{detector}$ introduced in Section 2.3, is not affected by local variables necessary to calibrate traps *in situ*, such as temperature, viscosity and trapped object geometry. Likewise, it does not depend on other key parameters determining optical trapping dynamics: laser power, trapping beam NA and structure, and medium and sample refractive indices, among others. Furthermore, force measurements can be undertaken on non-spherical samples [110, 111] and non-viscous media [118], for which calibration is considerably complex.

In this chapter, we have shown that the measurement of the total drag force exerted on a multiple-bead system can be addressed by analyzing the total momentum exchanged between the multiple-spot trapping beam and the several trapped beads. An indirect calibration-based method is not applicable here, as individual bead-trap calibration is inaccessible at the BFP. The system collects all the light creating the different optical traps and measures the change in the transverse component of the beam momentum, which is equivalent to the entire lateral drag force applied. Multiple-spot optical tweezers have been widely used for stable trapping of extended objects and calibrated for force measurements [110, 111, 31, 33, 32, 34]. However, the independence of the *in situ* experimental conditions permits the creation of arbitrary trap patterns adapted to a particular situation without the need of a new calibration.

We have demonstrated the accurate measurement of hydrodynamic forces on glass microcylinders trapped with pairs of optical tweezers and shown that most light was eventually forward-scattered, which permitted beam momentum measurements. For micro-rods in the same order of magnitude of biological specimens, i.e. in the micron range, we measured $2.1 \pm 0.6\%$ backscattering. For microorganisms trapped in watery solutions, the relative refractive index, n_{rel}, is substantially smaller than that of the samples used here. For example, for an *E. coli* bacterium with refractive index $n_{EC} = 1.388$ [116], we expect $n_{rel} = 1.04$. For chromosomes with $n_{Chrom} = 1.36-1.4$ [30], the refractive index will be $n_{rel} = 1.05$ at highest. In this kind of samples, there will hence be negligible backscattering and the light-momentum detection principle can be applied. Therefore, the results here are applicable to precise measurements on rod-shaped organisms in microbiological studies, which constitutes a primary concern in microbiology as they are widely found in nature. For example, in experiments analyzing hydrodynamic properties of biological swimmers, a given microorganism can be trapped with pairs of optical tweezers that can be used for controlled alignment and orientation.

As will be discussed in Chapter 7, in addition to rod-shaped samples, the method described here can be undertaken in non-viscous media, such as the interior of a cell.

Biological cargoes driven by molecular motors can be directly trapped without the aid of spherical probes, and the pulling forces measured under strict physiological conditions. Importantly, many of these cargoes have an elongated, rod-like shape (e.g., chromosomes, mitochondria, peroxisome peroxules, etc.). Even vesicles that are frequently targeted in cellular experiments for their appropriate characteristics, such as lipid droplets, can change from their rigid homogeneous sphere when they increase in size, posing difficulties for the calibration even in controlled conditions *ex vivo* [17].

The necessity for capturing a significant fraction of the scattered light is not more limiting in biological studies than in the experiments we carried out here. For example, inside a cell, backscattering is reduced as the relative refractive index of intracellular organelles (i.e., with respect to that of the cytoplasm) barely reaches $n_{rel} = 1.1$ (e.g., lipid droplet refractive index $n_{LD} = 1.48 - 1.53$ [119], cytoplasm refractive index $n_c = 1.36 - 1.375$ [120]), whereas for glass microcylinders in water, $n_{rel} = 1.17$. Angular light-scattering studies show that even in organelles with complex internal structure, such as mitochondria, scattering predominantly occurs in the forward direction [121].

Direct detection of beam momentum can also be used for synthetic objects with interesting trapping properties. As an example, elaborate microprobes exhibiting specifically engineered force fields can be manipulated and quantitatively analyzed, with possible applications for photonic force microscopy [32]. As previously mentioned, the tendency for elongated objects to align parallel to the optical axis, as observed both in biological and synthetic samples, can be easily resolved by using pairs of optical traps without impeding the measurement of global optical forces. Moreover, the arbitrariness of the HOTs array used in the multiple-bead experiment strongly suggests that direct detection of beam momentum is suitable for quantitative experiments with complex, non-Gaussian trapping beams creating adapted optical potentials [90, 91, 29].

6. Determination of heating due to IR light absorption in the optical trap

In optical tweezers, heating of the sample due to absorption of the laser light is a major concern as temperature plays an important role at microscopic scale. A popular rule of thumb is to consider that, at the typical wavelength of 1064 nm, the focused laser induces a heating rate of $B = 1$ °C/100 mW [8]. We analyzed this effect under different routine experimental conditions and found a remarkable variability in the temperature increase. Importantly, we determined that temperature can easily rise by as much as 4 °C at a relatively low power of 100 mW, for dielectric, non-absorbing particles with certain sets of specific, but common, parameters. Heating was determined from measurements of light momentum changes under drag forces at different powers, which proved to provide precise and robust results in watery buffers. We contrasted the experiments with computer simulations and obtained good agreement. These results suggest that this remarkable heating could be responsible for changes in the sample under study and could lead to serious damage of live specimens. It is therefore advisable to determine the temperature increase in each specific experiment and avoid the use of a universal rule that could inadvertently lead to critical changes in the sample.

6.1. Heating in optical traps

Optical tweezers have been proven to be a powerful microtool for biological studies since their inception, pioneered by Arthur Ashkin [5]. This non-invasive technique exhibits some advantageous features including non-contact forces in the range 0.1–100 pN and compatibility with liquid medium environments which make it highly suitable for application in biological studies. However, even at the innocuous laser wavelength of 1064 nm used in our experiments, light absorption in water is not negligible; so localized heating at the focus of the optical trap and heat transfer to the immediate surroundings could produce small but significant thermal effects.

Different methods have been used to determine temperature increases due to the use of optical tweezers (see Fig. 6.1 and Table 6.1). By means of the fluorescence emission shifts of a temperature-sensitive Laurdan dye probe, Liu *et al.* [122, 123]

measured temperature increases of 1 °C/100 mW, 1.15 °C/100 mW and 1.45 °C/100 mW for trapped live human sperm cells, hamster ovary cells and liposomes, respectively. Haro-González *et al.* [38] found an increase of 9.9 °C/100 mW for a 980-nm laser trap, using quantum dot luminescence thermometry. Ebert *et al.* [124] developed a fluorescence ratio technique using the temperature sensitive dye Rhodamine B and the temperature-independent reference dye Rhodamine 110, and obtained a heating rate of 1.3 °C/100 mW. The same method was used by Wetzel *et al.*, who determined an increase of 2.3 °C/100 mW [125]. Kuo [126] used an adaptation of the wax-melting method to estimate the temperature increase, which was found to be 1.7 °C/100 mW. The changes induced by temperature in the refractive index of water were monitored by Celliers and Conia [36], who measured a 4 °C temperature increase in a 55-mW, 985-nm laser trap (7.3 °C/100 mW).
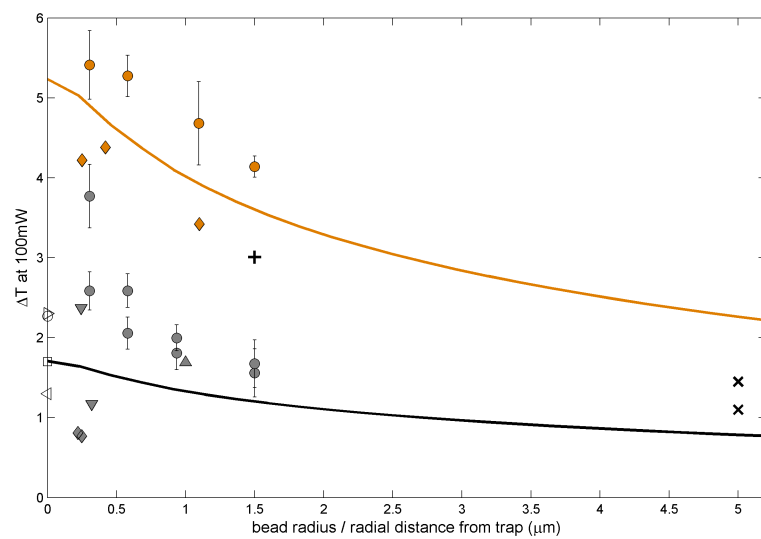

Figure 6.1.: Compilation of sample heating measurements in the literature obtained via a number of different methods. The black (orange) line corresponds to the simulations in water (glycerol) discussed in Section 6.5. Each symbol is described in Table 6.1.

Following a completely different approach, Peterman *et al.* [35] introduced a technique based on the analysis of the thermal motion of a trapped bead and measured a temperature increase of 3 °C - 4 °C/100 mW for different sizes of polystyrene beads diluted in glycerol and around 0.8 °C/100 mW for silica beads diluted in water. With the same method, Abbondanzieri *et al.* [128], using a system based on a dual-beam optical trap, measured a heating of 0.4 °C every 100 mW of laser power at the back of the objective. Similarly, Jun *et al.* [67] compared the active and passive calibration of an optical trap and inferred heating rates of 2.4 °C/100 mW and 1.2 °C/100 mW for 0.49-μm polystyrene and 0.64-μm silica beads, respectively, in a 980-nm laser trap. Finally, for a 975-nm low-NA laser trap, Mao et al.

[37] obtained 5.6 ℃/100 mW by measuring the temperature-dependent viscosity of water in a Stokes drag experiment from direct force measurements based on light momentum.

Despite this variation in reported results, temperature increase at 1064 nm is often assumed, as a rule of thumb, to be approximately 1 ℃/100 mW [8]. This small heating is then frequently used to argue for the relative innocuousness of laser traps, especially when used with live samples, such as cells. However, as discussed in Ref. [35], laser heating is directly dependent on the intensity distribution of the trapping laser and is therefore sensitive to changes in experimental conditions which could give rise to particularly unfavourable cases with considerably larger temperature increases. For example, Peterman et al. [35] showed the increase in heating with the axial position of the trap in glycerol. Unfortunately, to the best of our knowledge, that is the only work in which the variability of the heating rate, B, is analysed with respect to some parameters.

To fill this gap, we assessed the change in B under different experimental conditions. Heating was measured while changing the numerical aperture of the objective, the suspension liquid, the material and size of the trapped particle, and the position of the trap. We found a remarkable dependence on some of the parameters and, more importantly, temperature increases as large as 4.0 ℃/100 mW in water. The experimental scheme was based on the analysis of the variation in measured drag forces on trapped particles under different laser powers, similar to that adopted in Refs. [35, 37]. The force was determined through measurement of the change in light momentum [19, 20, 21]. This method is independent of the specific properties of the sample; and particularly, it does not depend on the laser power or the chamber temperature. This allowed us to directly infer variations in the measured force as changes in the medium viscosity caused by the temperature rise. Our experiments were complemented with computer simulations of the heating produced by an optical trap. We used the model proposed by Peterman et al. [35], which provided an accurate description of the experimental data.

6.2. Heating-induced calibration deviation

In previous work [21], we showed the validity of interpreting, under certain strict conditions, back focal plane (BFP) interferometry signals as measurements of light momentum changes; that is, as direct readings of the trapping force. The most significant requirements for such an interpretation are: 1) the use of a high-NA, aplanatic collecting lens that captures all the light from the optical traps; and 2) to track the light intensity distribution at the BFP of the collecting lens with a position sensitive detector (PSD). The usual approach to measuring forces in optical tweezers consists of calibrating the trap stiffness κ (pN/μm), in accordance with: $F = -\kappa \cdot x$, and the position sensitivity β (μm/V), such that: $x = \beta \cdot S_x$ (where S_x is the sensor positional voltage signal). In particular, we proved that if the

aforementioned conditions hold, the product $\alpha_{trap} = \kappa \cdot \beta$ (pN/V) is invariant and equal to the constant and permanent momentum calibration of the sensor, $\alpha_{detector} = \frac{R_D}{\psi f' c}$ (see Section 2.3), where R_D is the detector radius, f' and ψ (V/W) are the focal length and the responsivity of the instrument, respectively, and c the speed of light:

$$\alpha_{trap} \equiv \kappa \cdot \beta = \frac{R_D}{\psi f' c} \equiv \alpha_{detector} \tag{6.1}$$

In contrast to α_{trap}, which must be calibrated, for example using the power spectrum method [94], $\alpha_{detector}$ is obtained from first principles and is determined by the optical parameters of the beam detection system alone. This suggests that, if the required instrument design conditions are fulfilled, no new *in situ* trap calibration is necessary when the experiment changes [20, 21] and force can be directly obtained as: $F_{x,y} = -\alpha_{detector} F_{x,y}$. The momentum calibration of the force sensor, $\alpha_{detector}$, is independent of the geometry of the trapped object and of the structure of the trapping beam [69]; moreover, and importantly for the purpose of this paper, it is not dependent on laser power or chamber temperature.

In Fig. 6.2, we used the discrepancy between the two schemes to determine changes in sample temperature. A close look at the results for $\alpha_{trap} = \kappa \cdot \beta$ reveals that the equivalence $\alpha_{trap} = \alpha_{detector}$ starts to fail when the laser power is increased, with α_{trap} deviating from the constant value $\frac{R_D}{\psi f' c}$. This is indicative of a local temperature increase due to laser absorption (of 4 °C/100 mW in Fig. 6.2), which leads to incorrect κ and β calibration if overlooked. As discussed by Peterman *et al.* [35], temperature affects the power spectra of optically trapped microspheres, both as a thermal variable governing Brownian motion and through the viscosity of the solvent, which importantly is dependent on it.

6.3. Measurement of temperature increase

In this work, determination of local temperature in an optical trap is based on the measurement of the viscosity of the solvent, which is accessible in a single step from Stokes-drag force measurements. As described previous chapters, drag forces are assessed from light-momentum measurements, such that: $F_{drag} = -\alpha_{detector} S_x$, where S_x is the position sensitive detector (PSD) signal. The light-momentum calibration parameter, $\alpha_{detector}$, has been demonstrated to be independent of the geometry of the trapped object and of the structure of the trapping beam [19, 20, 21, 69], and importantly, it is not dependent on the laser power or sample temperature. In this way, changes in the measured drag force when incrementing the trap power, and therefore increasing the sample temperature, are directly caused by the variation in the medium viscosity, given as follows:

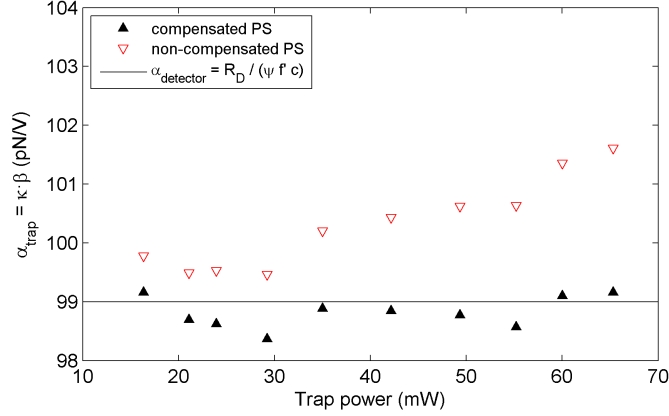$$\eta(T) = \frac{\alpha_{detector} S_x}{6\pi R v b} \tag{6.2}$$

Figure 6.2.: Discrepancies between $\alpha_{detector}$ and $\alpha_{trap} = \kappa\cdot\beta$, obtained from the power spectrum analysis, provide evidence of change in the sample when the laser power is increased. When the temperature increase is considered in the power spectrum (PS) fitting [94], the calibration is compensated and α_{trap} is constant.

where R is the radius of the trapped microsphere, v is the flow velocity and b is the Faxén correction due to the sphere-to-surface interaction [6, 7]. With this intention, we used a piezoelectric stage to produce constant drag forces (see Section 3.1.3). In Fig. 6.3a (top), we show the sudden drop in the force reading when the trap power is switched from 20 mW to 200 mW. As all the other variables are fixed, this is indicative of a change in the water viscosity that arises from the temperature increase induced by laser heating. When the intensity is decreased back to its original value, the original force is reversibly recovered. Laser heating at and around the focus of an optical trap is due to absorption of the NIR laser light, primarily by the solvent [122, 36, 35, 37], as we discuss below. The dynamic viscosity thus becomes a natural vehicle to connect force readings and sample temperature. Variations in force readings can be translated into changes in the viscosity of the medium, which we can directly convert into changes of sample temperature (see Fig. 6.3a, bottom). For water and glycerol, the relation between viscosity and temperature is given by [35]:

$$\log \eta_{water}\left(T\right) = \frac{1.3272\cdot\left(293.15 - T\right) - 0.001053\cdot\left(T - 293.15\right)^2}{T - 168.15} - 2.999$$

$$\text{(6.3a)}$$

$$\eta_{glyc}\left(T\right) = T^{31.734}\cdot e^{\left(-237.03 + \frac{16739}{T}\right)}$$

$$\text{(6.3b)}$$

In agreement with previous results [122], in all our experiments we found a linear relation between the trap power, P_{trap}, and the temperature, T, in the range 20 °C – 30 °C: $T = T_{room} + B\cdot P_{trap}$ (see Fig. 6.3b). Trap power was monitored from the S_{SUM} signal of the PSD: $P_{trap} = \frac{1}{\psi}S_{SUM}$ (see Section 2.3). In all the experiments,
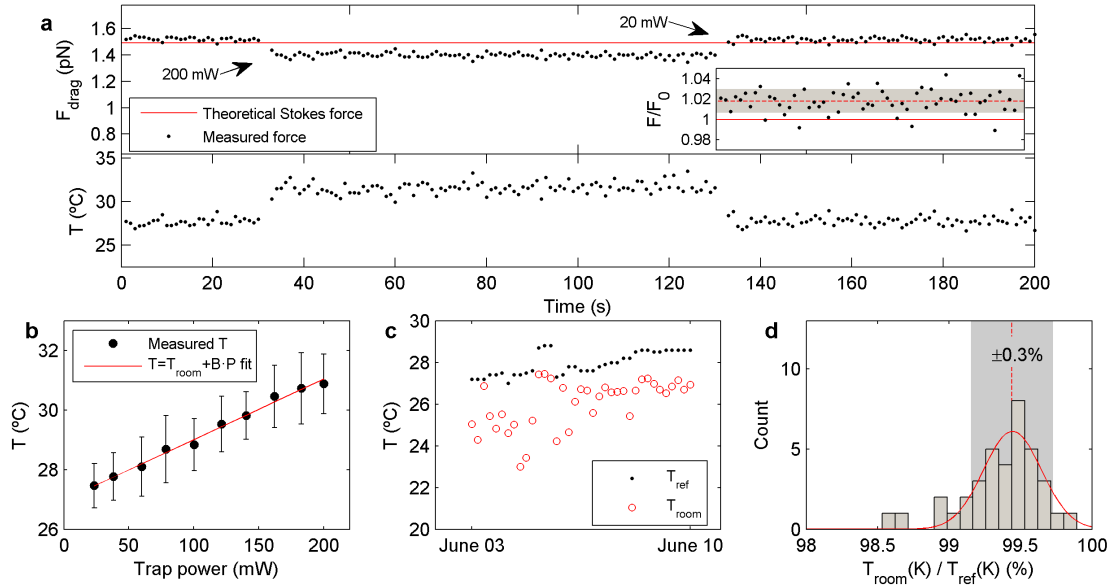
Figure 6.3.: Determination of temperature through measurements of light momen-
tum. (**a**) Top: Drag force measured on a 1.16-µm bead for 200 seconds. Each
dot is the mean drag force obtained from the square force signal over one cycle,
which is produced by the piezoelectric stage continuously applying a triangular
oscillation. Power is switched from 20 mW to 200 mW at second 30 and back to
20 mW after 100 seconds. Bottom: Temperature obtained from the force mea-
surement depicted in the top panel, through Eqs. 6.2 and 6.3. (**b**) Both the
heating rate, B, and room temperature, T_{room}, were determined from the linear
fit to measurements of temperature at 10 different laser powers between 20 and
200 mW. (**c**) Temperature values obtained from all the experiments on 1.16-µm
beads in water (red circles) compared with independent measurements with a pre-
cision thermometer (black dots). (**d**) The ratio $\frac{T_{room}}{T_{ref}}$ showed a standard deviation
similar to that expected from the ±2–3% of the diameter of the beads used.

ten temperature measurements, T_i, at trapping powers, $P_{trap,i}$, of 20 mW, 40 mW,
..., 200 mW, were linearly fitted by $T = T_{room} + B \cdot P_{trap}$, from which we could
obtain the heating rate, B, with an estimated precision of 10–15%, and the room
temperature, T_{room}. Final heating rates (Fig. 6.5) were calculated from the mean of
3–5 measurements. Along the measurement procedure schemed in Section 4.1.1, each
force value used for sample temperature calculations was taken as the mean over 20
consecutive cycles; and the corresponding standard deviation, typically in the range
±1–3%, was considered to be the associated error bar. Such standard deviation
resulted in an uncertainty of ±0.5 °C–1.5 °C in temperature measurements.

We compared T_{room} with an independent measurement obtained with a precision
thermometer (±0.1 °C), T_{ref}, and observed clear correspondence between the mea-
surements (Fig. 6.3c), with an average deviation of −1.5 °C (−0.5%) due to a slight

discrepancy between the measured and the theoretical drag force (+2%). When normalized by T_{ref}, the room temperature measurements exhibited a $\pm 0.3\%$ standard deviation (Fig. 6.3d), which mainly comes from the $\pm$ 2–3% standard deviation of the diameter of the monodisperse polystyrene microspheres we used (see Table 6.2).

Bead (µm)	Velocity in water				Force at 25°C (pN)	Velocity in glycerol (µm/s)	Force at 25°C (pN)
	A (µm)	f (Hz)	target (µm/s)	actual (µm/s)			
0.610 ± 0.014 (PS)	40	2	320	323.1	1.68	0.4	2.14
1.16 ± 0.04 (PS)	40	1	160	160.6	1.62	0.2	2.05
1.87 (PS)	25	1	100	100.8	1.67	-	-
2.19 ± 0.05 (MR)	21	1	84	84.7	1.66	0.16	3.15
2.32 (Si)	20	1	80	80.7	1.68	-	-
3.00 ± 0.07 (PS)	16	1	64	64.6	1.78	0.12	3.27

Table 6.2.: Actual flow velocities applied to the different microspheres used in our drag experiments, measured via the piezoelectric stage output reading (see Section 3.1.3), and theoretical Stokes drag forces applied.

In Section 6.5, the temporal evolution of heating is discussed from a numerical point of view to ensure that it is factually instantaneous. In experiments, we analyzed the variability of the measured viscosity with the stage velocity and found no significant change, which indicated that the dissipation of heat was faster than the motion of the fluid, so the temperature "experienced" by the particle was constant (Fig. 6.4).

To conclude, the oscillation parameters were chosen so that they produced similar drag forces on the microspheres used, which had different radii and were given by their corresponding manufacturers (Table 6.2). The diameter of the smallest microspheres (0.61 µm) was also confirmed using dynamic light scattering (DLS, data not shown[1]).

6.4. Variability under experimental parameters

Measurements of B, carried out as described in Section 6.3 and shown in Fig. 6.3b, had a reproducibility of approximately $\pm 10\%$ (compatible with that estimated from the linear fit), as shown in the experiment in Fig. 6.5a, which was repeated 10 times. Here, a 1.16-µm polystyrene microbead trapped at $z_{trap} = 10\,\mu m$ from the lower coverslip of the microchamber experienced a heating rate of 1.9 °C $\pm$ 0.2 °C/100 mW ($\pm 11\%$); similar to previous results in the literature (see Fig. 6.1 and Table 6.1).

---

[1]We thank A. Farré for this measurement at IDAEA - *Institut de Diagnosi Ambiental i Estudis de l'Aigua* (CSIC - *Consejo Superior de Investigaciones Científicas*).
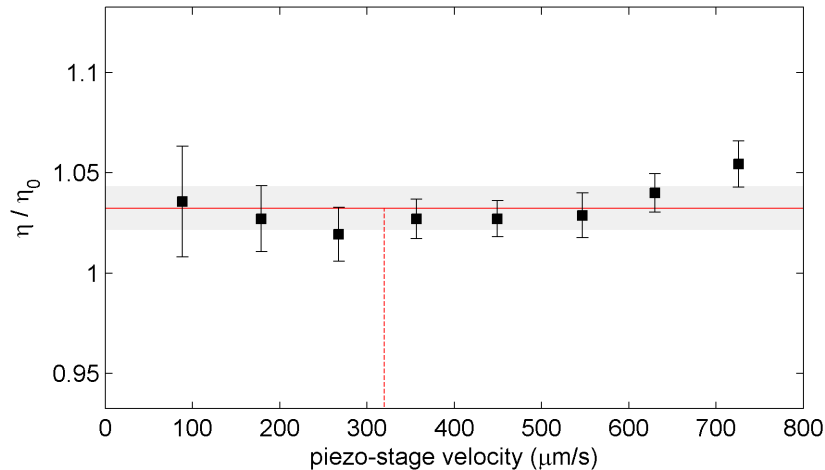
Figure 6.4.: Water viscosity measured with a 0.61-µm bead at different flow velocities. The vertical dashed red line indicates the velocity of 320 µm/s applied for this kind of beads in our study (Table 6.2). The solid red line and the gray shadow are the mean and standard deviation of the quotient η/η_0.

The first parameter analysed that affects trap heating was the axial position of the trap (Fig. 6.5b): a response previously measured and modelled in glycerol [35]. As discussed in the Section 6.5, the higher heat conductivity of the coverslip means that it acts as a heat sink, cooling the trap more as it is placed closer to the interface. Similarly to previous findings [35], heating was observed to increase rapidly in the first 10 µm above the lower glass surface, though in our case it saturated at approximately 1.9 °C/100 mW (the same value obtained in Fig. 6.5a) in the range 10–30 µm. The temperature increase is chiefly concentrated in a region ~10–15 µm around the trap position, z_{trap}, so that heat dissipation by the coverslip is actually sufficient to cool down the trap only below $z_{trap} = 10 - 15\,\mu\text{m}$. For this experiment, the water-immersion, NA = 1.2 objective was used, which avoids spherical aberration and permits efficient trapping over the whole microchamber axial range.

We then analysed the effect of particle size. Despite it having been suggested that this parameter has only a small influence on the final result, we observed a difference of over twofold in B for particles with diameters from 0.61 µm to 3.00 µm (see Fig. 6.5c): much greater than the error associated with the determination of B (10–15%, see Fig. 6.5a). The larger the particle, the lower the heating was. As discussed in Section 6.5, this result can be directly connected to the radial temperature profile caused by the optical trap. This was reproduced by both the water-immersion NA = 1.2 and the oil-immersion NA = 1.3 objectives, though greater heating was observed with the latter, especially for smaller beads.

In addition, we studied the effect of reducing the effective numerical aperture, NA_{eff}, of the trapping beam. A diaphragm was placed at an optical equivalent to the entrance pupil of the NA = 1.3 objective (of focal length f'_{obj}) to modify the diameter
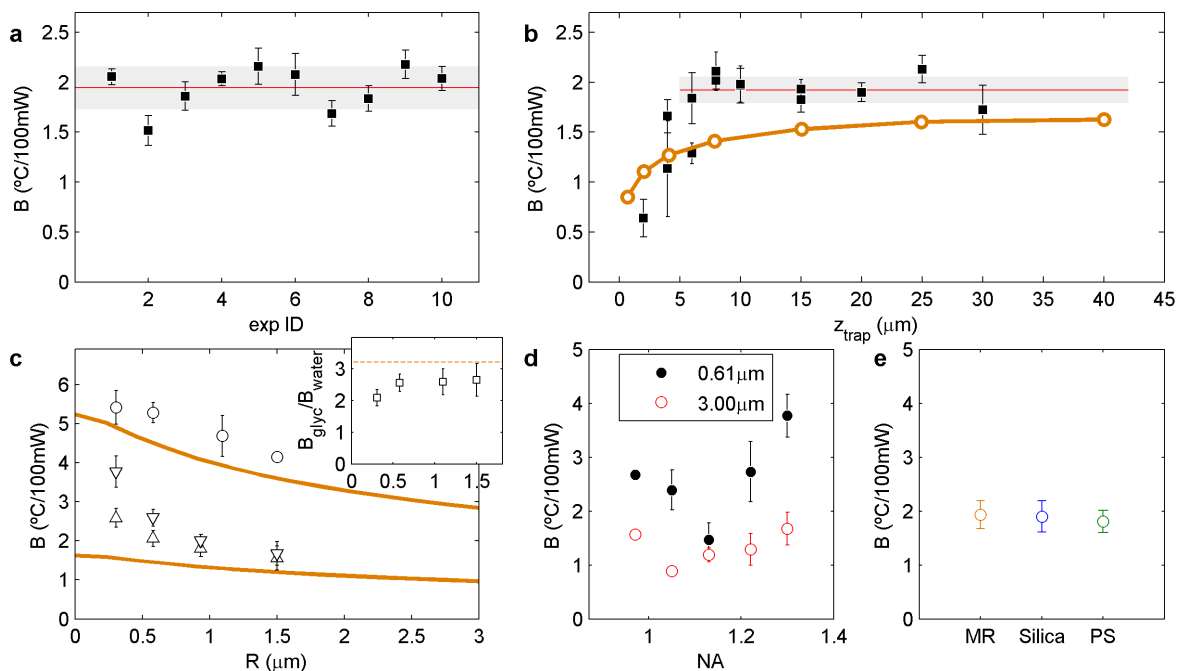
Figure 6.5.: Variability of B under different experimental conditions. (**a**) Systematic measurements of the heating rate with the same sample showed a standard deviation of 11%, confirming the error estimation of 10–15% in our measurements. (**b**) Variation of B for different axial positions of the trap with a 1.16-μm polystyrene microbead (squares). The mean and standard deviation of the measured B values beyond $z_{trap} = 10\,\mu m$, equal to the independent measurement shown in **a**, are indicated by the red line and the grey area, respectively. Results from the simulations described in section 6.5 are superimposed (orange trace). (**c**) Heating for particles of different radius, R, and the same material (polystyrene). Upward (downward) triangles correspond to particles trapped with the water-(oil-) immersion NA = 1.2 (NA = 1.3) objective in water, while circles correspond to the particles trapped with the NA = 1.2 objective in glycerol. The solid lines are radial temperature distributions obtained from simulations in water ($\alpha/\kappa = 23.7\,^{\circ}C/W$) and glycerol ($\alpha/\kappa = 76.4\,^{\circ}C/W$) respectively, both for the NA = 1.2 objective. The inset shows the experimental ratio B_{glyc}/B_{water} (squares), which is similar to the nominal ratio: 3.2 (dashed line). (**d**) Heating for 0.61-μm and 3.00-μm polystyrene microbeads in water, trapped with the oil-immersion objective with different values of NA_{eff}. (**e**) B was found to be equal for three 2-μm particles of different materials (MR: melamine resin, PS: polystyrene).

of the beam, D_{beam}, such that: $\text{NA}_{\text{eff}} = \frac{D_{beam}}{2} f'_{obj}$. The measurements were critically dependent on NA_{eff}, exhibiting variations as large as ± 2 °C/100 mW and ± 1 °C/100 mW for 0.61-µm and 3.00-µm polystyrene beads, respectively (see Fig. 6.5d). For the case of 0.61-µm beads, our experimental results did not exhibit a monotonic trend; whereas they revealed an ascending pattern for 3.00-µm beads. The output laser power was set to produce a similar range for the trap power (20 mW to 200 mW) when reducing NA_{eff}, as commented in Section 6.3.

As reported by Peterman *et al.* [35], B also depends on the suspension medium. The variation in temperature found when we changed water for glycerol was similar to the quotient between the ratio of light absorption, α (m^{-1}), to thermal conductivity, K, between the two liquids, $\frac{(\alpha/K)_{glyc}}{(\alpha/K)_{water}} = 3.2$ (see Fig. 6.5c, inset). This result suggests that, as assumed by different models [122, 36, 35, 37], the temperature increase depends linearly on α/K.

In contrast, heating seemed to be independent of the material the trapped particle was made of. Fig. 6.5e shows the results for microspheres of similar sizes (2.19 µm, 2.32 µm and 1.87 µm) but different dielectric materials (melamine resin, silica and polystyrene, respectively). Despite the ratio α/K for the three beads differing by 4 orders of magnitude (13.8 °C/W, $3.6 \cdot 10-3$ °C/W, 50 °C/W, respectively), B was found to change by only 0.1 °C/100 mW ($\pm 4\%$), in accordance with the fact that trap heating is mainly governed by laser absorption in the surrounding buffer.

6.5. Heat transport simulations

Temperature, T, is in general terms governed by the heat equation:

$$\nabla^2 T = \frac{1}{k}\frac{\partial T}{\partial t} - \frac{q}{K} \tag{6.4}$$

where $k = K/c \cdot d$ is the thermal diffusivity, c is the specific heat, d is the density, K is the thermal conductivity and q the energy absorbed per unit of volume and unit of time. Eq. 6.4 describes how energy transferred by the laser is diffused throughout the surrounding space.

To solve this equation, we need to specify both the function q and the boundary conditions. We used the absorption proposed by Peterman *et al.* [35], which is an improved version of the spherical model of Liu *et al.* [122], taking into account the finite volume of the focus:

$$q = \frac{1}{2\pi}\frac{\alpha P}{r^2 + \left(\lambda/2\pi\text{NA}^2\right)^2} \tag{6.5}$$

Here, we used $f(\theta) = 1/2\pi$ (see Section "Theoretical model" in Ref. [35]) and we included the explicit dependence on the NA. In the equation, α (m^{-1}) corresponds to the optical absorption and P to the incident laser power. Considering the

geometry of the problem, defined by the flat parallel coverslips, with higher conductivity ($K_{glass} = 1.4\,\mathrm{W/m/K}$) and lower absorption ($\alpha_{glass} = 0.005\,\mathrm{m^{-1}}$) than water, acting as heat sinks, we alternatively chose boundary conditions with cylindrical coordinates, in which the spherical radial coordinate in Eq. 6.5 is expressed as $r^2 = \rho^2 + (z - z_{trap})^2$. We set the Dirichlet boundary conditions: $\Delta T = 0$ at $\rho = 80$ μm and $z = 80$ μm; whereas a real water-glass interface was simulated at $z = 0$, which is the surface closest to the optical trap in all the experiments. The trap height, z_{trap}, was 10 μm in all the experiments, unless otherwise stated.

The evaluation of the temporal part of the equation shows that after 1 ms the temperature reaches 90% of the steady-state value (Fig. 6.6a). For the highest flow velocity applied in our experiments (320 μm/s for 0.61-μm beads in water; see Table 6.2), such a characteristic heating time is still faster than the fluid displacement time around the focal region. Sample heating of more than 90% is thereby ensured and a steady-state situation can be considered due to our precision in temperature measurements, which was around 10–15%. This agrees with the results in Fig. 6.4, which show no substantial variation in the measured viscosity for flow velocities up to 700 μm/s. For the lower flow rates applied to larger microbeads, the rate of heat diffusion is even faster compared with the velocity of the medium (Table 6.2).

In Fig. 6.6b, we represent a typical $\rho - z$ section of the temperature distribution around the trap (NA = 1.2) for three different axial positions of the focus. This shows that sample warming decreases as the trap approaches the water-glass interface, due to heat dissipation into the coverslip becoming more efficient. The axial and radial profiles for the trap at $z_{trap} = 10\,\mu m$ μm shown in Fig. 6.6c reproduce the characteristic $\ln(1/r)$ decay proposed by Mao *et al.* [37], whose solution had been empirically found by Celliers and Conia [36] some years before, $\Delta T = a - b\ln(r)$, and experimentally proved by Haro-González *et al.* [38].

We can observe how the distance to the closest glass surface governs the heating produced by the laser (Fig. 6.6d). This is due to the low α/K of glass, which dissipates the heat produced by the laser, keeping the water-glass interface almost at room temperature. Unlike the result found by Peterman *et al.* [35] obtained assuming spherical symmetry (see Fig. 6.8a and Table 6.3), temperature was found to increase only over the first 0–10 μm from the bottom surface of the chamber, where the heat dissipated by the glass coverslip was significant enough to cool down the focus. After this, B becomes almost constant as the distance increases across the rest of the chamber. As mentioned above, the temperature profile decaying sufficiently beyond 10 μm from the trap centre (Fig. 6.6c) leads to the cooling by heat dissipation through the coverslip being unnoticeable for z_{trap} values of more than 10 μm.

In contrast, the boundary in the radial coordinate, ρ, seems to have little impact on the value of the temperature near the focus. In Fig. 6.6c, inset ii, we show three temperature distributions simulated with the Dirichlet $\Delta T = 0$ °C condition fixed at different distances, which collapse into a single curve, i.e., maintaining the same
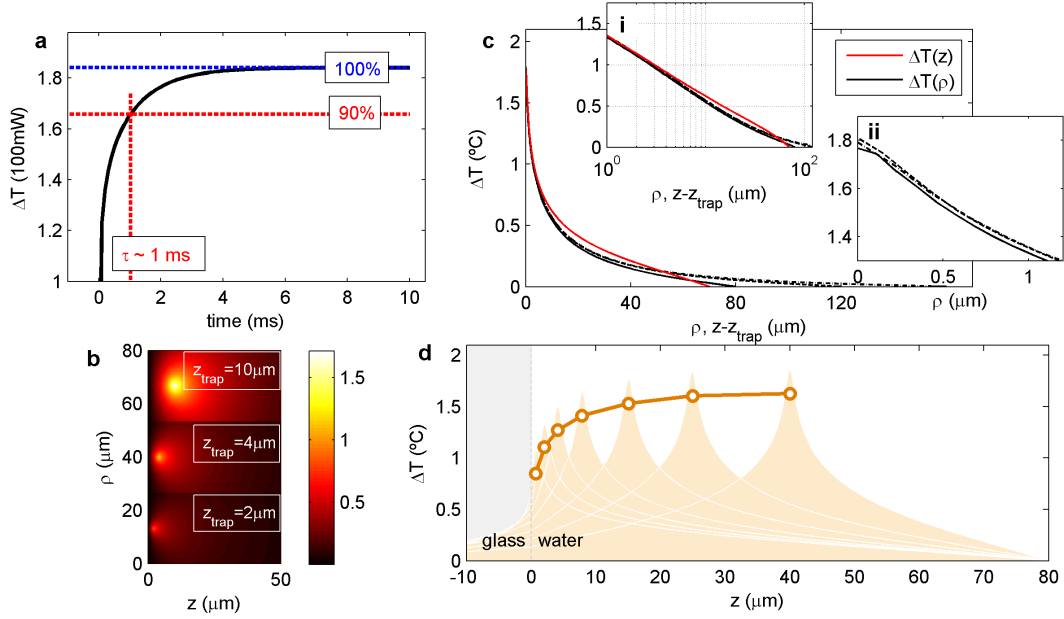
Figure 6.6.: Simulation of temperature distribution inside the microchamber. (**a**) Temporal evolution of heating. The simulation shows that the temperature reaches 90% of its steady-state value after 1 ms. (**b**) Temperature distribution for three different axial positions of the trap. $z = 0$ represents the bottom surface of the chamber and ρ has been shifted appropriately for visualization. (**c**) Radial (black) and axial (red) temperature distributions following the $\ln(1/r)$ decay (log scale plot in inset **i**). Radial temperature distributions for the $\Delta T = 0$ boundary condition at $\rho = 80$, 120 and 160 μm (solid, dashed and dot-dashed black lines) converge to the same value at short distances (inset **ii**). (**d**) Simulations of the temperature distribution at different heights (shadowed areas). The circles correspond to estimations of B for a 1.16-μm bead according to $B_{bead} = \Delta T(\rho = R_{bead})$.

maximum heating in the vicinity of the trap. Interestingly, this profile describes the temperature increase measured for microspheres of different radii, R_{bead}, as shown in Fig. 6.5c. We found a certain connection between the temperature at distance R_{bead} and the heating of a particle with that radius, i.e. between B_{bead} and $\Delta T(\rho = R_{bead})$ at $P_{trap} = 100$ mW (Fig. 6.7a). This is consistent with the fact that our method, based on drag force measurements, detects viscosity changes at the interface between the bead and the medium.

Concerning the effect of the NA, we had observed (Fig. 6.5c) considerably higher heating rates for the oil-immersion, NA = 1.3 objective, particularly on the smallest, 0.61-μm beads. Likewise, Fig. 6.5d showed large variations in B when modifying NA_{eff}. The heat source in our simulations, q, includes the dependence on the NA and also yields greater heating for higher NA; though the resulting difference is one order of magnitude smaller than in the experiments. We believe that the model
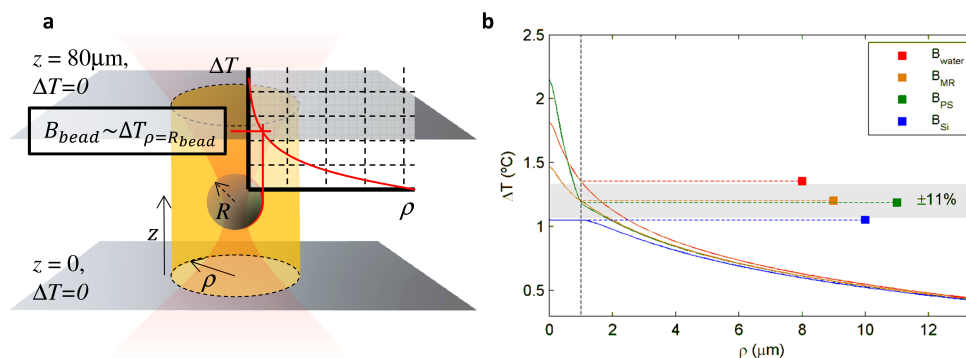
Figure 6.7.: Simulation of temperature distribution inside the microchamber. (**a**) Relation between the heating rate for a given bead, B_{bead}, and the temperature distribution produced by the trap. (**b**) Simulated temperature profile introducing a 2-μm microsphere at the focus of the trap. The gray area corresponds to the reproducibility of our measurements, shown in Fig. 6.5a. (MR: melamine resin, PS: polystyrene, Si: silica).

does not accurately describe the temperature increase at distances comparable to the beam waist, $r \sim \omega_0$, as the result depends on the shape of the beam, which is not correctly modeled in this region. Additionally, experimental modification of the effective NA was achieved by reducing the beam diameter with an iris placed at an optical equivalent of the entrance pupil of the objective. This, at the same time, modifies the overfilling, which affects additional variables that govern the optical field at the focus and hence may also introduce some deviations from the simulations. For 3.00-μm beads, alternative model approaches [36, 37] qualitatively describe the heating–NA relationship (see Section 6.5.1). The fact that these beads are far larger than the beam waist, and that the optical field at R_{bead} is hence described more precisely, is the reason why the heating predicted through simulations is closer to the experimental results.

Finally, we checked the impact of the particle material on temperature. We incorporated into the simulations a second material with a spherical shape, corresponding to the particle, at the focus of the trap. We analyzed the temperature distribution for three different dielectric materials (melamine resin, silica and polystyrene) and verified that the temperature over the particle surface, i.e. at a distance R_{bead}, was

almost independent of the material of which the microsphere was made within our experimental errors (Fig. 6.7b). Therefore, only the optical absorption and the thermal conductivity of the suspension medium seemed to play a role in the heating (see the ratio α/K for water and glycerol in Fig. 6.5c, inset). To a first approximation, an intuitive interpretation of these results is that the particle "experiences" on average the temperature of the surrounding solvent which is independent of the particle itself and is thereby given by the decreasing temperature profile produced by the trap alone, making the temperature increase lower for larger particles. Note that for absorbing particles, such as semiconductor or metallic particles, heating would be qualitatively higher since the energy transferred to the medium would be sufficient to alter the temperature distribution.

6.5.1. Model discussion

We made use of the MathWorks Partial Differential Equation (PDE) Toolbox to simulate the heating of the sample due to a laser trap. Given that the geometry we used exhibits cylindrical symmetry, we adapted the heat equation to include the Jacobian along the radial component and solved the problem on a 2D surface.

As mentioned above, the modeling adopted by Peterman *et al.* of $B(z)$ [35], which was conceived in spherical geometry in which the trap is created at $r = 0$ and the $\Delta T = 0$ condition is fixed at $r = z$, exhibits a non-stopping increase (Fig. 6.8a). In contrast, the choice of cylindrical symmetry and the Dirichlet boundary conditions at two parallel surfaces corresponding to the coverslips yields a constant B value after an abrupt rise over the first 10 μm (Fig. 6.8b). This is especially evident in the real sink case with thermal conductivity K_{glass} (Fig. 6.8c), due to the coverslip only being capable of cooling the sample sufficiently when the trap is placed very close to the interface.

In Fig. 6.8d and Table 6.3, we show two models in the literature that describe the radial temperature profile with similar accuracy. The model of Celliers and Conia [36] was simulated in the same cylindrical geometry and coincided closely with our simulations, with a slightly greater temperature increase, $\Delta T(\rho)$, for the NA = 1.3 objective than for the NA = 1.2 objective. The analytical expression provided by Mao *et al.* [37] also coincides with our measurements and exhibits an even greater difference between the two objectives.

Finally, we simulated the effect of reducing the effective NA of the trap (Fig. 6.5d and Fig. 6.8e). Although expressed in terms of the trap power, the heating rate, B ($^{\mathrm{o}}$C/100 mW), is more related to the local irradiance, which eventually explains the observed variation. Irradiance is contained in the shape of the heating source, $q(r)$, in models of Peterman *et al.* [35] and Celliers and Conia [36], as well in the R factor in that of Mao *et al* [37] (see Table 6.3).

Models in Refs. [36] and [37] seem to capture the main behaviour of the heating dependence on NA$_{\mathrm{eff}}$ for the 3.00-μm beads. As compared with the experimental
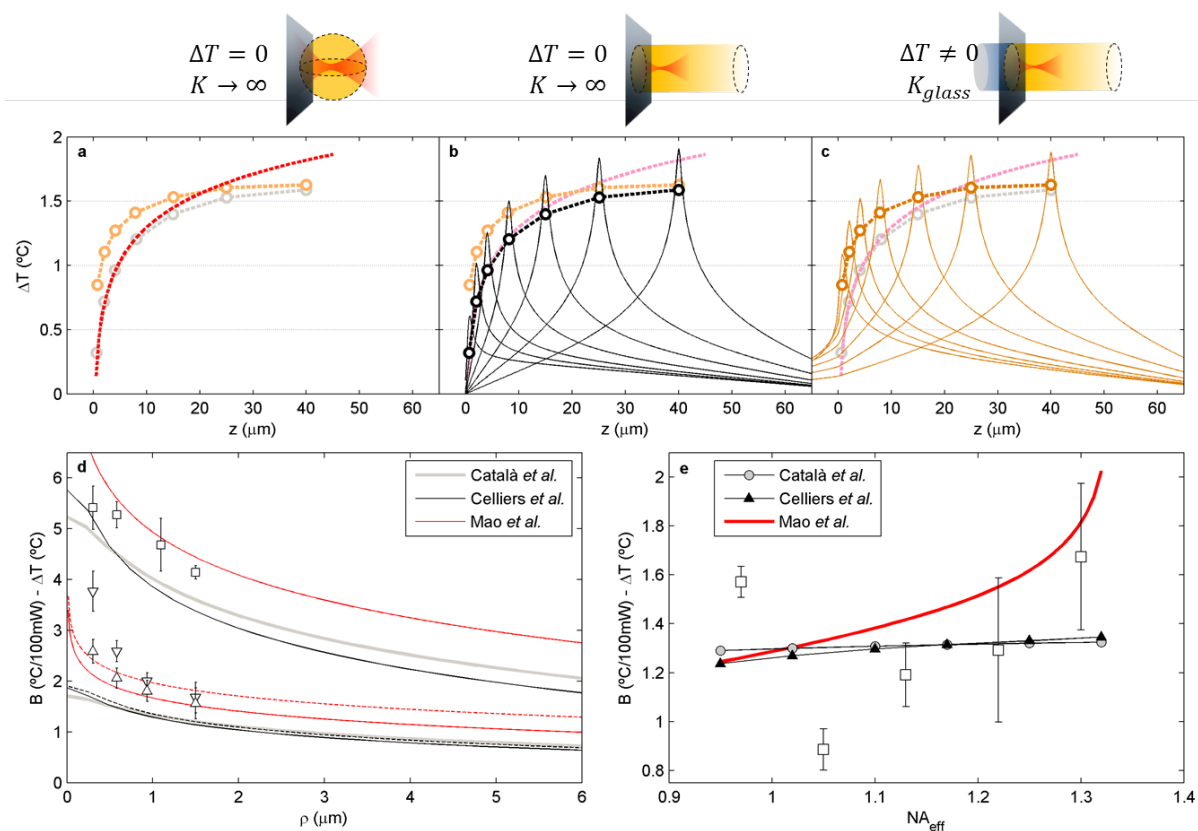
Figure 6.8.: Heat transport simulations. (**a**) The model of Peterman *et al.* [35] of $B(z)$ simulated in spherical coordinates (red dashed line). (**b**) $\Delta T(z)$ distributions in cylindrical geometry with $\Delta T = 0$ at $z = 0$ and 80 μm (solid lines correspond to $\Delta T(z)$ curves and circles are estimations of B for a 1.16-μm microbead). (**c**) Real sink at $z = 0$ and $\Delta T = 0$ at $z = 80$ μm. In **a-c**, the other two curves are superimposed in a light color for comparison. (**d**) Models in Refs. [35] (grey), [36] (black) and [37] (red) simulated in our cylindrical geometry. Solid (dashed) lines are simulations with NA = 1.2 (NA = 1.3). (**e**) Simulation of the dependence of B on the NA for the three models as in **d**, for 3.00-μm microbeads.

measurements, they reveal an ascending pattern that can be directly connected to the wider light cone illuminated, i.e. wider heat source. For the smaller, 0.61-μm beads, one could think of the smaller beam waist created with higher NA_{eff} to conclude that the therefore higher irradiance leads to greater heating as well. However, as mentioned in the previous sections, the optical field at the bead-medium interface is here bound to a number of aberrations and deviates from an ideal Gaussian shape, which leads to the measurements notably deviating from the simulations. Besides, our reducing NA_{eff} by means of a diaphragm at the back of the trapping objective leads to a different overfilling, thereby producing higher variations in the local optical field.

6.6. Discussion on laser-induced heating in optical tweezers

We demonstrated that the direct determination of viscosity changes caused by increasing laser powers is a robust strategy for obtaining local temperatures, i.e. the heating rate B. This was possible due to our force calibration being based on the detection of the trapping beam momentum (which is independent of the sample temperature and trapping power, among other features) which was compared to the temperature-dependent Stokes drag calibration. In this way, we could directly interpret changes in the measured force as variations in the sample temperature. Importantly, the method is precise enough to assess trap heating in watery buffers and makes it unnecessary to carry out experiments in media with higher α/K values.

The agreement between our results and simulations allows us to extract some interesting conclusions concerning the process of sample heating in an optical trap. The model proposed in Ref. [35] seems to capture the main elements necessary for the description of the behavior of the temperature inside the chamber under different conditions. Simulations showed that the temperature distribution originated by an optical trap followed the typical $\ln\left(1/r\right)$ decay reported in other papers [38, 36, 37]. This decay describes the heating experienced by microspheres of increasing radii, which was observed to change by a factor of 2 and 3 from 0.61- to 3.00-μm beads, trapped with an NA = 1.2 and an NA = 1.3 objective, respectively. Such variation was considerably greater than the measurement precision, which was assessed to be of the order of 10–15%. In contrast, the material of the tweezed dielectric microspheres did not affect the measurement of B, which was also confirmed by simulations including the presence of the bead. Finally, the trap height played an important role in sample heating, as the coverslip acts as a sink, dissipating heat and maintaining the interface nearly at room temperature. When the trap was created below 10 μm, it was efficiently cooled down; whereas beyond that distance, B remained almost constant, due to the temperature increase being concentrated mainly within the 10 μm surrounding the trap focus.

The results of this work demonstrate the substantial variability in laser-induced trap heating, depending on the multiple experimental conditions examined. Temperature control is of the utmost importance in precise experiments in biophysics and other applications of optical trapping. This makes it highly necessary to perform *in situ* heating calibration, instead of applying the straightforward rule of thumb of 1 °C/100 mW. Large measurement inaccuracies, e.g. derived from erroneous thermal trap calibration, as well as changes in the activity of biological parameters [128] could arise if the actual trap temperature is omitted. As a critical example, samples of a size similar to the beam waist, $R \sim \omega_0$, showed a ± 2 °C/100 mW variation in B by only changing the effective NA of the trapping beam (Fig. 6.5d). Moreover, trap heating studied by other research groups with manifold techniques (see Fig. 6.1 and Table 6.1) have demonstrated this variability. In conclusion, each experimental optical trap configuration leads to different heating performance due to several aspects, such as sample size, beam structure, microchamber dimensions and buffer specifications.

The remarkable heating observed under certain conditions could have an impact on experiments with cells. In such samples, laser radiation is absorbed by the intracellular medium, the cytosol, which is a complex and highly crowded compound. However, because cells and their components present weak absorbance in the NIR range, we can assume that absorption of laser radiation is dominated by water. Typical laser powers required to manipulate intracellular organelles are of the order of 200 mW. Natural structures inside cells are usually smaller than ˜1 μm. In addition, high-NA (phase-contrast) oil-immersion objectives are normally preferred for the visualization of cells. Therefore, in general terms, heating will tend to be particularly large in this kind of experiments. Assuming that the heating of the cell is similar to that of water, and using the result for B for the smallest microsphere of diameter 0.61 μm and for NA = 1.3, we can estimate that the local temperature will rise by approximately 8 °C.

In fact, the large attainable temperature increase that 1064 nm lasers can produce could induce serious damage that one should assess beforehand. Although photodamage due, among other possibilities, to the generation of singlet oxygen is accepted to be the main source of damage upon live cells [129], thermal heating should be reconsidered as a feasible origin of cell damage/death as well.

As we have shown, heating can be reduced by the use of trapping objectives of different NA or by creating the traps close to the coverslip. Furthermore, the use of laser wavelengths with lower optical absorption [127], such as 820 nm, as proposed by Haro-González *et al.* [38, 130], appears to be a good choice for reducing photodamage and cell heating. In fact, those authors found that temperature increase at this wavelength was close to zero at 300 mW.

Author		Technique	λ_{trap} (nm)	Target	B measurements (°C/100 mW)			B value at $\lambda=1064$ nm
					H$_2$O		Glyc	
					NA1.2	NA1.3	NA1.2	
Català	●○	Light momentum & Stokes drag	1064	0.61 µm PS 1.16 µm PS 1.87 µm PS 2.19 µm MR 2.32 µm Si 3.00 µm PS	**2.59** **2.06** **1.81** 1.93 1.90 **1.56**	**3.77** **2.59** **2.00** -- -- **1.67**	**5.41** **5.27** -- 4.68 -- **4.14**	--
Peterman[9]	◆◇	Power spectrum & Stokes drag	1064	0.444 µm Si 0.500 µm Si 0.502 µm PS 0.840 µm PS 2.200 µm PS	**0.81** **0.77** -- -- --		-- -- **4.22** **4.38** 3.42	--
Mao[12]	▲	Light momentum & Stokes drag	975	2 µm Si	5.6		--	**1.69**
Jun[11]	▼	Active-Passive	980	490 nm PS 642 nm Si	7.8 3.8		--	**2.37** **1.17**
Haro-González[4]	✚	Quantum dot luminescence thermometry	750 808 920 980 1090	3 µm PS	0 0 5 9.9 4.9		--	0 0 8.26 **3.01** 4.30
Liu[2,3]	✕	Temperature-dependent luminescence (Laurdan)	1064	sperm cells CHO cells (10 µm) liposomes (10 µm)	1 **1.15** **1.45**		--	--
Celliers[8]	○	Refractive index	985	--	4 K/55 mW		--	**2.27**
Kuo[7]	□	Wax melting	1064	--	**1.7**		--	--
Ebert[5]	◁	Temperature-dependent luminescence (Rhodamine B & 110)	1064	--	**1.3**		--	--
Wetzel[6]	▷	Temperature-dependent luminescence (Rhodamine B & 110)	1064	--	**2.3**		--	--

Table 6.1.: Assorted studies of laser heating in optical traps. From left to right, we indicate: the first author of the publications reporting the results, the symbol used in Fig. 6.1, the method used to assess trap temperature, the laser wavelength used, the sample trapped (size and material), the values reported (subsections NA = 1.2 and NA = 1.3 for the present study, and measurements in glycerol buffer as well for measurements by Peterman *et al.* [35]). In the last column, we indicate the equivalent B factor obtained by applying the Beer-Lambert law [8] with spectral attenuation $\alpha(\lambda)$ reported by Kedenburg *et al* [127]. Values represented in Fig. 6.1 are in bold typography. PS: polystyrene, MR: melamine resin, Si: silica, CHO: Chinese hamster ovary.
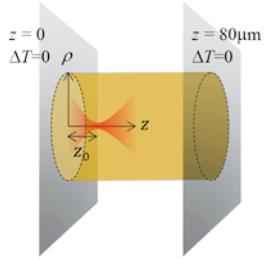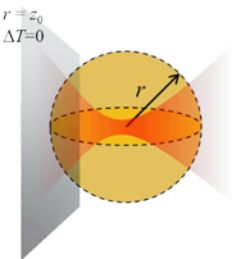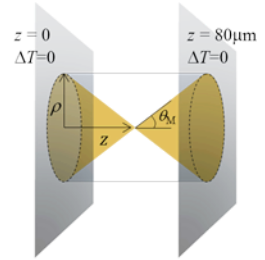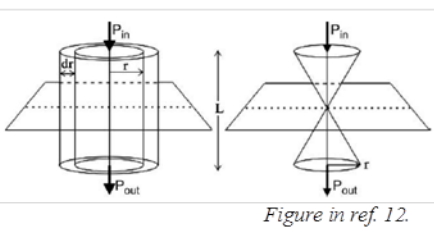
Català		$$q_{Peterman} = \frac{\alpha P}{2\pi}\frac{1}{\rho^2 + \left(z - z_{trap}\right)^2 + a^2}$$
Peterman[9]		$$q_{Peterman} = \frac{\alpha P}{2\pi}\frac{1}{r^2 + a^2}$$
Celliers[8]		$$q_{Celliers} = \begin{cases} \dfrac{\alpha P}{2\pi(1 - \cos\theta_M)}\dfrac{1}{\rho^2 + z^2}; \dfrac{\rho}{z} < \tan^{-1}\theta_M \\ 0 \qquad\qquad ; \dfrac{\rho}{z} > \tan^{-1}\theta_M \end{cases}$$
Mao[12]	 *Figure in ref. 12.*	$$\Delta T(\rho) = \frac{\alpha P}{2\pi K}\ln\frac{R}{\rho}$$

Table 6.3.: Laser heating models and geometries. Different geometries and mathematical models have been used for laser heating simulations. The finite volume of the of the focus is represented by the parameter $a = \frac{\lambda}{2\pi\mathrm{NA}}$ [35].

113

7. Optical trapping and light-momentum detection in embryonic tissue

The possibility to penetrate non-invasively into tissue makes optical tweezers a promising tool for quantitative studies in cellular mechanics, among others. Regulation of many processes during embryo development, such as mechanically-induced shape changes or collective cell migration, can be accessed by the use of optical tweezers. Most studies targeting developmental biology have been carried out with simplified models, such as fruit flies (*Drosophila melanogaster*), *Caenorhabditis elegans* nematodes and zebrafish (*Danio rerio*).

M. Welte *et al.* used optical micromanipulation to trap lipid droplets moving along microtubules in living Drosophila embryos and measured stall forces of molecular motors [119]. Recently, in combination with light-sheet microscopy, K. Bambardekar *et al.* demonstrated the use of optical traps to deform epithelial cell junctions and measured tensions in the order of 100 pN [9, 2]. *C. elegans* were used by G. Leitz *et al.* to analyze photothermal and photochemical effects induced by the trapping laser light [131].

Zebrafish embryos have been widely used as a model for developmental biology [132]. Recently, collective cell migration has been modeled using the wetting approach to describe the early embryogenesis stage, named epiboly [133]. At a similar stage, around 7 hours-post-fertilization (hpf), F. Hörner *et al.* studied different mechanobiological properties by trapping microbeads injected into the cells in a holographic optical tweezers (HOTs) set-up [134]. Similarly, J. Staunton *et al.* injected microbeads into the yolk of living zebrafish to introduce a position-sensing calibration method for microrheology based on optical trapping [53].

Other optical trapping experiments without synthetic microbeads have been carried out, using optical micromanipulation in a strictly non-invasive manner. For example, P. Johansen *et al.* trapped red blood cells, macrophages and injected bacteria in the caudal vein of 2-day old zebrafish larvae [135]. Using similar samples, S. Harlepp *et al.* characterized hemodynamic forces after calibrating the optical traps [136]. In older, 6-day old zebrafish, I. Favre-Bulle *et al.* induced vestibular responses onto the ear otoliths [137].

From the technical point of view, optical transparency has powered zebrafish samples as good embryo models, both regarding imaging techniques and efficient optical

trapping. On the other hand, quantitative force measurements, which have been discussed to be challenging for irregular samples and non-homogeneous media, becomes especially demanding in embryonic tissue.

In this chapter, we address the possibility to use the direct force measurement method as a standard approach in such samples. The invariant calibration of the method, $F_{measured} = \alpha_{detector}\, S_x$, will probably solve most of the issues impeding accurate *in situ* calibration, such as irregularities in the trapped samples and inhomogeneity. Also, the standard active-passive calibration method, used in the viscoelastic cytoplasm of cells [118, 67], is likely to fail in live embryos due to the violation of the fluctuation-dissipation theorem [138].

Here we present a preliminary demonstration of the accurate detection of light momentum through tissue. Our approach is based on the measurement of trapping force profiles on microbeads injected into the embryos. Similar to the recent work by W. Ahmed *et al.* in mouse oocytes [139], these are then compared with measurements in water to confirm that light-momentum calibration is maintained.

7.1. Light momentum detection through zebrafish tissue

7.1.1. Zebrafish sample preparation

Zebrafish wild type animals and embryos were maintained under the European Union and German animal welfare protocols [134]. After fertilization, eggs were gently laid in agarose ramps for comfortable orientation of the cell. In Fig. 7.1a, a 2-nanoliter drop containing a highly concentrated solution of 1-μm latex beads was injected at 1-cell stage. These do not affect embryo development and spread uniformly over the whole specimen, as demonstrated by F. Hörner *et al.* in Ref. [134]. As shown in Fig. 7.1b, beads spread over the cells after first divisions, and eventually appear over the whole embryo (Fig. 7.1c).

At approximately 5 hours-post-fertilization (hpf), embryos were dechorionated and immersed and fixed in a low melting agarose solution. Light momentum detection requires the collection of the whole beam emerging from the optical traps, for which the samples need to be sandwiched between two thin coverslips. The use of two thin coverslips, instead of a lower coverslip and an upper thicker slide, is necessary due to zebrafish samples being approximately 500 μm thick. In this way, the collecting lens working plane can be located deeper in the chamber. The animal pole faced the water-immersion, trapping objective, for efficient trapping of the injected microbeads.
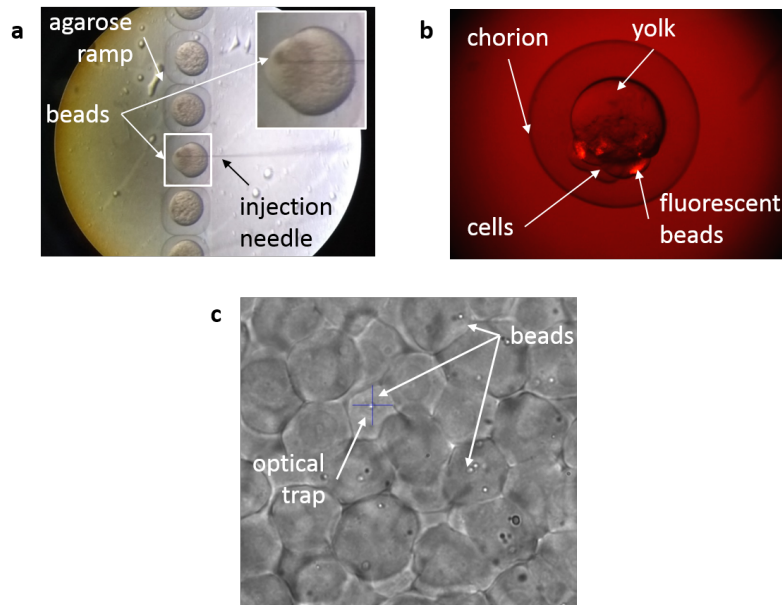
Figure 7.1.: Embryo injection and sample trapping. (**a**) 1-nL drop injection at 1-cell stage. (**b**) Parts of the embryo after two cell divisions. (**c**) Bright-field image of an embryo at 6 hpf while one of the beads injected is trapped.

7.1.2. Scattering and initial momentum variation

Different structures in the embryonic tissue affect the trapping beam propagation and induce evident changes in light momentum and eventual trapping light loss. Refractive index mismatches between different cells, as well as scattering structures such as different sorts of vesicles, cell membranes or nuclei, are elements that affect free propagation of light in *in-vivo* experiments. It is therefore necessary to quantify to what extent light emerging from the optical traps is still captured by the collection system, as well as in which degree the main contribution to the light momentum change is induced at the trapping plane, i.e. between the optical trap and the trapped sample.

We use a CCD camera at the BFP of the light momentum detection system to observe light scattering through different parts of the embryonic tissue, as illustrated in Fig. 7.2a-c. The beam appears similar to the typical Gaussian profile shown in previous analysis (see examples in Figs. 3.1 and 5.4). However, in this case an underlying structure arising from scattering becomes clear, especially when the beam propagates through the cells (Fig. 7.2a). When the trap is focused at the edges of the embryo, the two parts of the beam –that freely propagated through agarose and that scattered through the embryo– are visibly separated by a surface diffraction pattern (Fig. 7.2b). For experiments in the cells, it is therefore needed that the embryos be accurately oriented such that the animal pole faces the objective and the traps are created far from the external walls of the embryos. On the other hand,

the yolk is observed to induce weaker scattering (Fig. 7.2c). Figs. 7.2a-c illustrate light trajectories through the different parts of the embryo.
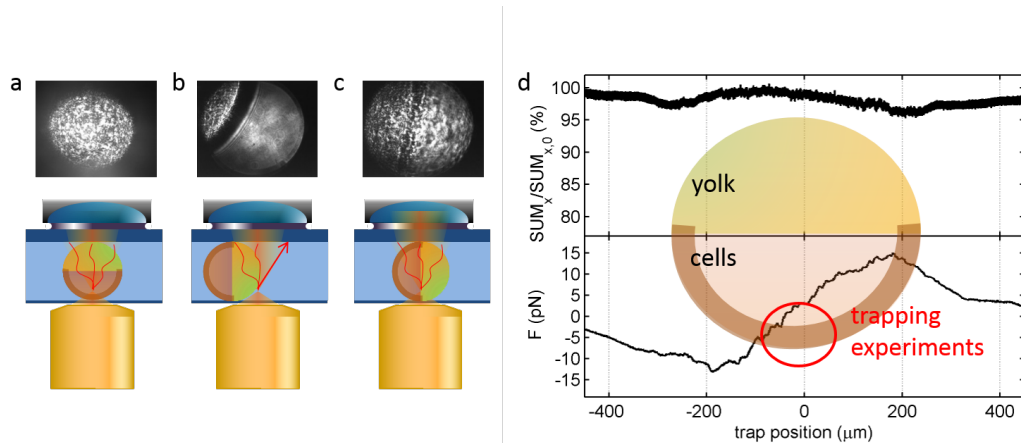

Figure 7.2.: Light scattering through the embryo. BFP images of (**a**) the beam after propagating through the cells and yolk; (**b**) half the beam propagating through the yolk and the other half though agarose; (**c**) half the beam propagating through the cells and the other half through the yolk. (**d**) Power captured and initial beam momentum variation across the embryo. Yolk and cell parts are indicated, as well as the region chosen from trapping experiments.

Light creating the optical traps efficiently leaves the embryo and gets captured by the collecting lens. Observe that more than 95% of light reaches the detector at the BFP in Fig. 7.2d - top. The captured light profile is notably similar to that of a homogeneous bead with diameter larger than the trapping wavelength ($D > \lambda$, see Section 4.3.3). Under a ray-optics picture, it makes sense that light will be more reflected backwards for greater incident angles as the trap leaves the center of the embryo, which explains the drop in the captured light intensity for $x_{trap} \sim D/2$.

The variation for the initial light momentum across the embryo exhibits two main features (Fig. 7.2d - bottom). At a large scale, it clearly follows the trapping force profile of a 500-µm sphere, i.e of a size similar to that of the embryo. However, a random variation in the momentum is observed at a micron scale. We hypothesize this to be in close connection with the scattering structure appearing beneath the Gaussian envelope profile in Fig. 7.2a.

Typical trap displacements giving rise to optical forces of interest are on the order of tens to hundreds of nanometers. For example, cell interfaces in Drosophila embryos have been deflected approximately $\pm 0.5\,\mu$m by oscillating the optical trap at $\pm 1\,\mu$m [9]. In 5 to 7 hours-post-fertilization zebrafish embryos, injected beads have been oscillated by means of an optical trap around ± 220 nm, in order to study the viscoelastic properties of different cellular structures, such as cell organelles or cell nuclei [134]. We can thereby consider our further measurements to be insensitive

to the large scale, 500-µm sphere force profile envelope. The direct force measurement method operates over changes in light momentum, for which a different –but constant– initial momentum will not perturb force readings.

In contrast, the latter mentioned effect (1-µm scale oscillations in light momentum) will somewhat add a certain noise to the measurements. For example, if a membrane or a vesicle is to be applied a certain stress for viscoelastic response studies, accidental light momentum variation will affect the precision of the measurements. This is due to the typical trap oscillation amplitudes being in the same order of magnitude that the scattering-induced, small-range changes in light momentum. It is therefore necessary to quantify the magnitude of such momentum variations and ensure that light momentum changes detected in the direct force measurement method occur primarily in the optically-trapped sample of interest.

7.1.3. Measurements on injected beads

In this section, we evaluate the measurement deviations due to light scattering through tissue. PS beads injected at 1-cell stage are present over the embryo region of interest. They are manipulated with an AOD-driven optical trap from which we can obtain the trapping force profile, as has been used in Chapter 4. In the same set-up, beads are trapped in a water solution to obtain a reference to be compared with the measurements *in vivo*.

Forces in water and in the cytoplasm of embryo cells differ according to the higher medium refractive index in the latter case. We took this into account by scaling the measurements such that they could actually be compared. According to the optical trapping theory of Y. Harada and T. Asakura (Ref. [10], see Eq. 2.1), measurements in water, with respect to cytoplasm, will scale as follows:

$$C = \frac{\left(n_{rel}^w\right)^2 - 1}{\left(n_{rel}^w\right)^2 + 2} \bigg/ \frac{\left(n_{rel}^e\right)^2 - 1}{\left(n_{rel}^e\right)^2 + 2} \tag{7.1}$$

where $n_w^{rel} = 1.18$ and $n_e^{rel} = 1.15$ are the relative refractive index for polystyrene beads ($n_{PS} = 1.57$) in water and in the embryo, respectively. Refractive index of the cell cytoplasm was approached to be $n_e = 1.37$ according to observations by C. López-Quesada *et al.* on the refractive index of different elements within live cells [140]. Similarly, this assumption is compatible with refractive index measurements by C. Curl et al. [120].

The scale factor through Eq. 7.1 is 1.23. A similar check, using the Optical Tweezers Computational Toolbox [12] to simulate a 1-µm polystyrene sphere in water and in an $n = 1.37$ medium yields a scaling factor of 1.20. In Fig. 7.3, we show simulations in water and cytoplasm and the latter multiplied by the scaling factor.

An example of force profile measurement set over a series of eleven beads in the same embryo is shown in Fig. 7.4. The embryo region in which these measurements were
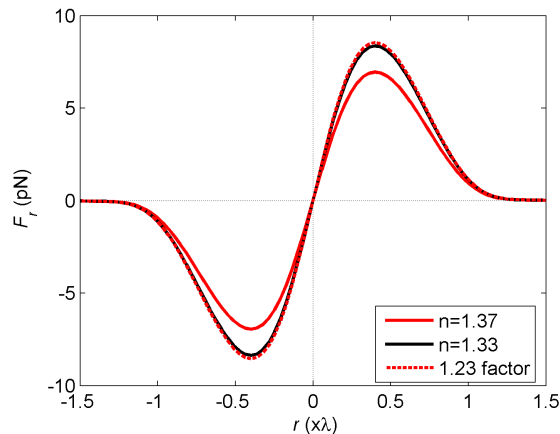
Figure 7.3.: Relative refractive index scaling.

carried out is indicated in Fig. 7.4a, which reproduces the overall initial momentum variation curve of Fig. 7.2d. As visible in Fig. 7.4b, the force profile directly obtained from injected microbeads is affected in two ways. As mentioned before, the overall change in the initial momentum, due to the trapping experiment being undertaken at a certain position within the embryo, offsets the measurement. Nevertheless, this does not affect the relative change in momentum due to the trapping of the microsphere. In Fig. 7.4c, it is clear that the measurements on the several beads mostly overlap after removing said offset.

On the other hand, the aforementioned 1-μm scale noise produced by smaller scattering structures adds up to the measurements. This will induce increasing errors, for instance, in eventual trap stiffness calibration and escape force measurements. In Fig. 7.4d, the mean and standard deviation of the force profile measurement are represented for the measurement set after removing the overall offset. The averaged profile measurement exhibits a neater shape that becomes closer to the ideal optical force response of a microsphere. Finally, it is important that the average profile matches that obtained from water after the latter is applied the $^1/_{1.20}$ factor discussed above. In turn, observe that force profile measurements in water exhibit, as expected, smaller standard deviation.

As quantitative indicators for the measurement accuracy, we used trap stiffness evaluated from linear fits around $x_{trap} = 0$ and maximum forces (Fig. 7.5). Scattering-induced noise in force profile measurements translate here in larger standard deviations in the determination of these quantities. Measurements in water show a mean stiffness of $9.1\,{}^{pN}/_{\mu m}$ ($\pm7\%$) and a mean maximum trapping force of $2.3\,\mathrm{pN}$ ($\pm7\%$). Results for the embryos in which we obtained more data (samples #1 and #4) appear in Table. 7.1.

As expected, measurements in embryos exhibit less reproducibility than those in water. However, the average values inside the embryos match very reasonably those
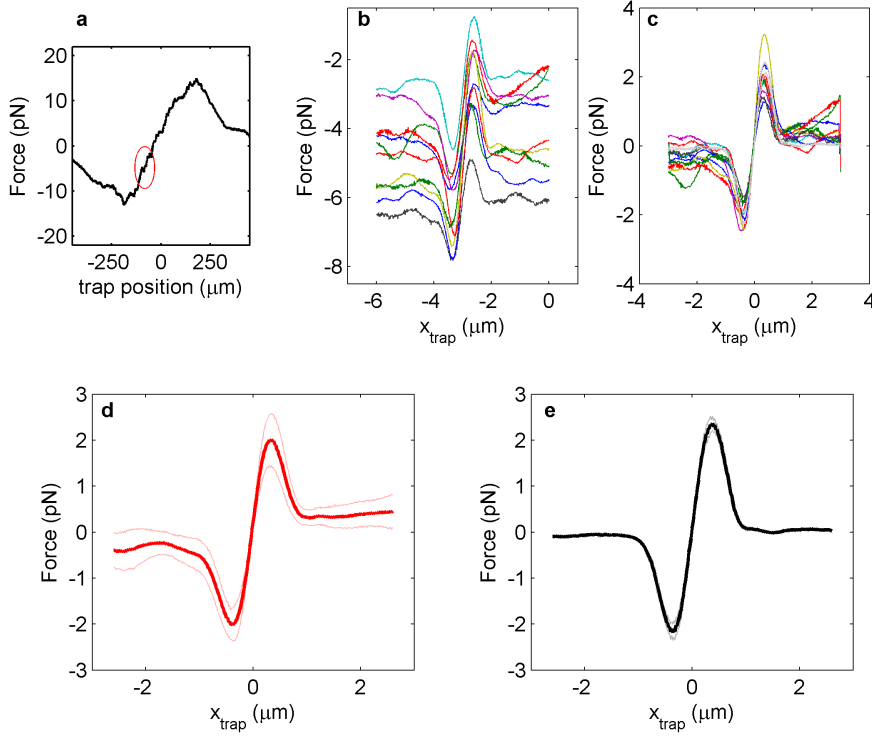
Figure 7.4.: Force profile measurements in embryos. (**a**) Embryo region in which the measurement set was carried out in this example. (**b**) Force profiles directly obtained from eleven different microbeads. (**c**) Force profiles obtained after removal of the overall initial light momentum. (**d-e**) Mean (±s.d.) profile measurement in the embryo and in water. $^1/_{1.20}$ factor is applied in the latter case.

obtained in water. In fact, we can assume that tissue-induced scattering will affect light momentum in an *a priori* random fashion. This enlarges the standard deviation of measurements but still yields correct values for measurements averaged over an increasing number of micro-spheres.

	embryo 1	embryo 4	water
trap stiffness (pN/μm)	8.9 (±21%)	11.6 (±22%)	9.1 (±7%)
maximum trapping force (pN)	2.1 (±20%)	2.6 (±22%)	2.3 (±7%)

Table 7.1.: Trap stiffness and maximum trapping forces in embryos and water.

We also noticed that the standard deviation of the measurements in water was yet higher than those we had obtained in previous chapters. This was likely due to the trapping beam being not perfectly optimized for stably trapping samples of decreasing size. In fact, we noticed that effective trapping of 1-μm beads was critically dependent on the objective compensation ring (Nikon Plan Apo, 60x, NA=1.2) and
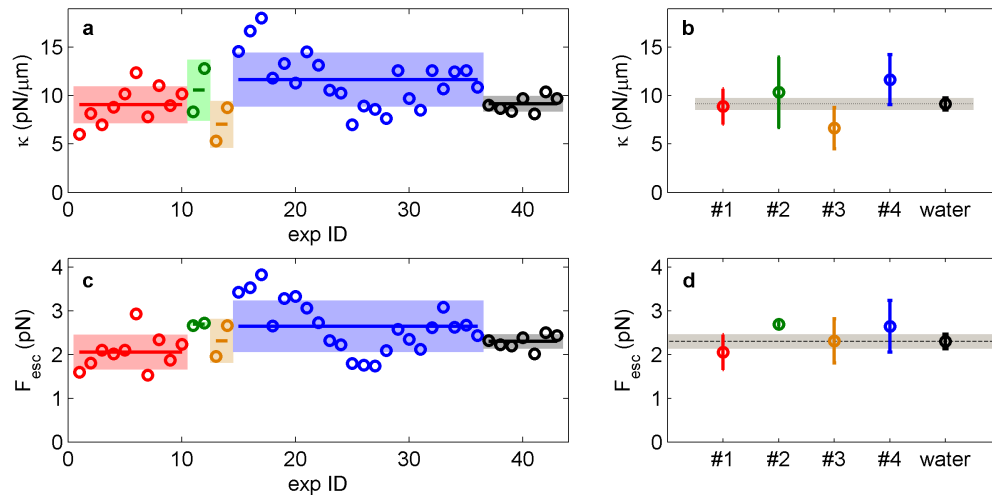
Figure 7.5.: Trap stiffness and maximum trapping force measurements in different embryos. (**a**) Trap stiffness values over a series of different beads in four different embryos (red, green, orange, blue) and in water (black). Shaded areas and flat lines indicate average ($\pm$ s.d.). (**b**) Mean stiffness ($\pm$ s.d.) for the same series of measurements. The shaded area and the flat, dashed line indicates the measurement in water for comparison. (**c-d**) Measurements of maximum trapping forces with the same color code.

cover glass thickness. Similarly, note the lower maximum trapping force in these measurements, around 2 pN, whereas we had observed from 7 to 8 pN, with the same trapping power, in Fig. 4.18. This fact may also explain for the high, $\pm20\%$ reproducibility inside tissue and suggests therefore that more accurate measurements would be performed in a more optically stable trapping set-up.

To conclude, we confirm that the light momentum change primarily occurs at the trapping plane, which ensures the implementation force measurements. Interestingly, trapping of cellular structures has been widely reported in zebrafish [135, 136, 137] and Drosophila [9, 119], among others. Hence, the injection of auxiliary beads for precise force calibration can be in principle avoided. With this preliminary results, we envision that force measurement experiments with optical tweezers inside tissue can be carried out by means of the direct force measurement method.

8. Conclusions

I hereby depict the main conclusions I have reached during my PhD thesis, regarding the different topics I have studied:

Holographic optical tweezers set-up

- Different components of our holographic optical tweezers (HOTs) set-up have been thoroughly studied for ensuring that the experiments were carried out in a highly controlled manner. Laser fluctuations have been stabilized using NI-DAQ-controlled (power monitoring) and RS-232-controlled (power modulating) interfaces.

- Spatial light modulator (SLM) phase response (look-up-table, LUT) has been studied using an ellipsometric approach. Correlation with incident light power has been observed in relation with total laser power and with the Gaussian beam profile.

- Piezo-electric platform characterization has enabled generation of flows for controlled hydrodynamic tests, i.e. drag force trap calibration.

- Two of sources of inaccuracy for single-trap positioning in holographic optical tweezers (HOTs) have been studied and corrected for. Phase quantization produces positioning deviations in the order of 2 nm, in a range of approximately 5 nm around the so-called M-positions, $d_M^{(n)} \sim 1\,\mu\mathrm{m}\cdot n$. LUT mismatch results in 2-nm oscillations with a characteristic distance, the so-called L-distance, $d_L \sim 0.5\,\mu\mathrm{m}$.

Robustness of light-momentum force measurements

- Controlled drag force as a calibration reference has been shown more reliable than passive power spectrum calibration for testing light-momentum detection accuracy. Moreover, this has allowed for analyzing accuracy over the whole trapping range of forces, i.e. up to the escape force. The results have evidenced different deviations for each force applied, especially for larger, ray-optics-behaving microbeads.

- Experimental sources of error for light-momentum detection performance have been discussed, analyzed and corrected for. As a result, the invariant property of light-momentum force measurements has been proved within a $\pm 5\%$ variation.

- This brings to the direct force measurement method being only limited by the effect of back-scattered light loss. This has been confirmed through scattering simulations over the far field, as well as proved experimentally in relation to to Stokes-forces and force and captured light profiles by means of AOD-driven optical tweezers.

Force measurements on irregular samples

- Holographic optical tweezers (HOTs) has allowed for stable manipulation of multiple-bead systems. These have been used as early irregular objects to test for the robustness of the direct force measurement method on arbitrary samples. Studies of hydrodynamic interactions have been undertaken. The use of several optical traps has been proved robust for collective force measurements on extended objects.

- Micro-cylinders in a wide range of dimensions, from 2 μm to 50 μm, have been manipulated with pairs of HOTs. It has been shown that light creating the traps is efficiently captured by the detection system to perform force measurements. These have been confirmed to be accurate compared to slender-body hydrodynamic theory.

- Drag forces on large microspheres trapped in cogwheel beam traps have been measured with similar accuracy compared to the standard Gaussian beam trap.

- We envision the use of the direct force measurement method for studies in rod-shaped biological samples, e.g. bacteria and chromosomes, which can be manipulated in sets of multiple optical traps. The fact that biological samples have a considerably lower relative refractive index than the objects used here makes us consider that the accuracy found here is an upper threshold for measurements on such samples.

Determination of heating due to IR light absorption in the optical trap

- Controlled drag forces have been used for fast characterization of sample heating due to absorption of the trapping laser light. Sample heating has been confirmed linear against the trapping power: $T = T_{room} + B\,P$.

- We have found large variability in the heating occasioned in different experimental situations, e.g. involving particles of different size, distance to microchamber walls and trapping beam NA. It is important that heating has been assessed as high as 4 ⁰C/100 mW for certain, but common cases, such as 0.5-μm beads in NA = 1.3, oil-immersion objectives.

- Experimental analysis has been complemented with heat transport simulations. From that, we can conclude that laser heating occurs in the medium immediately surrounding the trapped sample and that the glass surface acts as a heat sink cooling the sample.

- Solutions we envision for sample heating consist in using larger particles as force probes if possible, performing optical trapping near the chamber surfaces, or using trapping lasers of wavelengths with smaller absorption coefficients in water.

Optical trapping and light-momentum detection in embryonic tissue

- Tissue-induced scattering in zebrafish has been shown to alter light momentum detection. First, we have observed that the initial momentum of the trapping beam is similar to the trapping force profile for a 500-µm sphere. From a close look into the measurements, we have noticed 1-µm scale signal oscillations due to the scattering structures of tissue.

- Measurements of trap stiffness and maximum trapping forces on injected microbeads have been proved to coincide with the same kind of microbeads in water after scaling the correspondig relative refractive index, n_{rel}. Force measurements in zebrafish tissue have been performed within $\pm 20\%$ standard deviation.

A. Appendix. Trap steering efficiency and positioning accuracy calculations from Fourier optics

In this appendix, we derive the expressions in Chapter 3 that describe trap efficiency affected by hologram pixelation and positioning inaccuracy produced by look-up-table (LUT) mismatch. First, we will use Fourier optics to describe scalar field propagation between the SLM plane and the trapping plane [24, 25].

In our set-up (Section 3.1), the SLM plane is conjugated onto the objective front focal plane through telescope 2 (4f configuration, lenses f_3 and f_4, see Fig. A.1)[1]. Assuming 1D holograms, the scalar field at the SLM (plane A), $U(x)$, becomes thereby $U\left(-\frac{f_3}{f_4}x\right)$ at the objective front focal plane (plane B). Its Fourier transform, scaled $\lambda f'$, yields the scalar field at the trapping plane (*Fourier plane*, plane C) [82]:

$$\mathcal{FT}_{\lambda f'}\left[U\left(-\frac{f_3}{f_4}x\right)\right] = \frac{f_4}{f_3}\tilde{U}\left(-\frac{f_4}{f_3}\frac{x}{\lambda f'}\right) = \frac{f_4}{f_3}\mathcal{FT}_{-\frac{f_3}{f_4}\lambda f'}\left[U(x)\right] \tag{A.1}$$

where we used the Fourier transform scaling property: $\mathcal{FT}\left[f(ax)\right] = \frac{1}{|a|}\tilde{f}(\frac{x}{a})$ ($\tilde{f}$ and $\tilde{U}$ are the Fourier transforms of f and U, respectively). The scalar field at the trapping plane (C) is hence the Fourier transform of the field at the SLM plane (A) through a scaling factor $-\frac{f_3}{f_4}\lambda f'$. In other words, we can compute the light distribution as $\left|\tilde{U}(u)\right|^2$ evaluating the spatial frequencies as follows:

$$u = -\frac{f_4}{f_3}\frac{x'}{\lambda f'} \tag{A.2}$$

where x' is the spatial coordinate at the trapping plane.

---

[1]For simpler notation, f_3 and f_4 express the image focal lengths of the lenses of telescope 2.
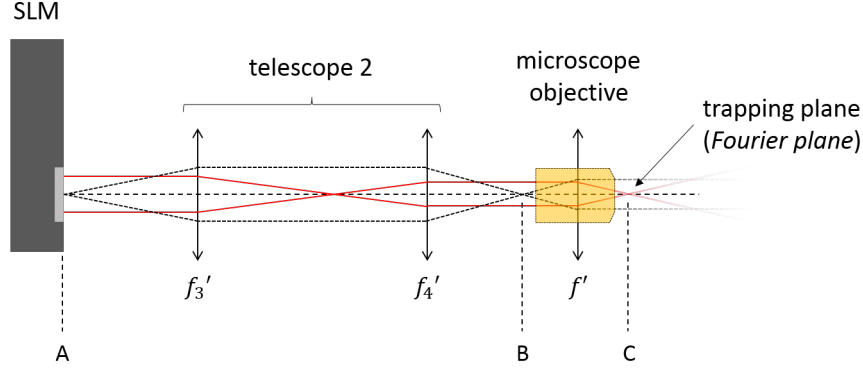
Figure A.1.: Optical Fourier transform.

In the following calculations, we use the convolution theorem. Being $\tilde{f}$, $\tilde{g}$ and $\tilde{h}$ the Fourier transforms of f, g and h, respectively [82]:

$$
\begin{cases}
h = f \cdot g & \rightarrow \quad \tilde{h} = \tilde{f} * \tilde{g} \\
h = f * g & \rightarrow \quad \tilde{h} = \tilde{f} \cdot \tilde{g}
\end{cases}
\tag{A.3}
$$

Likewise, we are considering the following Dirac function properties:

$$
f(x) \cdot \delta(x - a) = f(a) \cdot \delta(x - a)
\tag{A.4a}
$$
$$
f(x) * \delta(x - a) = f(x - a)
\tag{A.4b}
$$

The Fourier transforms of the terms appearing in Eqs. A.6 and A.10 are:

Function	Fourier Transform
$\operatorname{rect}\frac{x}{\xi}$	$\lvert\xi\rvert \operatorname{sinc}(\xi\,u)$
$\sum_{n=-\infty}^{\infty} \delta(x - n\,\xi)$	$\frac{1}{\lvert\xi\rvert} \sum_{n=-\infty}^{\infty} \delta\left(x - \frac{n}{\xi}\right)$
$e^{i\frac{2\pi}{\xi}x}$	$\delta\left(u - \frac{1}{\xi}\right)$

A.1. Trap steering efficiency

An ideal, continuous phase-only modulation of the form[2] $e^{i\frac{2\pi}{T}x}$ will position the trap at the desired position $d = \frac{f_3}{f_4}\frac{\lambda f'}{T}$. The discretization of the SLM can be expressed

---

[2]We consider no phase quantization or LUT mismatches in this section.

in terms of a Dirac comb function:

$$\sum_{n=-\infty}^{\infty} \delta\left(x - np\right) \cdot e^{i\frac{2\pi}{T}x} \tag{A.5}$$

If, in addition, we express the pixel (p) and SLM (L) finite sizes with the corresponding rectangular functions, the hologram at the SLM reads as follows (see Eq. 3.4):

$$U\left(x\right) = A \cdot \text{rect}\left(\frac{x}{L}\right) \cdot \left\{ \text{rect}\left(\frac{x}{p}\right) * \left[\sum_{n=-\infty}^{\infty} \delta\left(x - np\right) \cdot e^{i\frac{2\pi}{T}x} \right] \right\} \tag{A.6}$$

The term in Eq. A.5 Fourier-transforms, omitting constant factors, as follows:

$$\sum_{n=-\infty}^{\infty} \delta\left(u - \frac{n}{p}\right) * \delta\left(u - \frac{1}{T}\right) = \sum_{n=-\infty}^{\infty}\left(u - \frac{1}{T} - \frac{n}{p}\right) \tag{A.7}$$

After omitting some phase terms irrelevant for the light intensity distribution at the trapping plane, we thereby obtain Eq. 3.6:

$$\left|\tilde{U}\left(u\right)\right|^2 \propto \left| \text{sinc}\left(Lu\right) * \left[\text{sinc}\left(pu\right) \cdot \sum_{n=-\infty}^{\infty} \delta\left(u - \frac{1}{T} - \frac{n}{p}\right) \right] \right|^2$$

$$\propto \left| \text{sinc}\left(Lu\right) * \sum_{n=-\infty}^{\infty} \text{sinc}\left[p\left(\frac{1}{T} + \frac{n}{p}\right) \right] \delta\left(u - \frac{1}{T} - \frac{n}{p}\right) \right|^2$$

$$\propto \left| \sum_{n=-\infty}^{\infty} \text{sinc}\left[p\left(\frac{1}{T} + \frac{n}{p}\right) \right] \text{sinc}\left[L\left(u - \frac{1}{T} - \frac{n}{p}\right) \right] \right|^2 \tag{A.8}$$

A.2. LUT-induced positioning deviations

As discussed in section 3.2.2.3, the actual phase introduced by the SLM scales linearly as $\phi^{actual} = a\,\phi^{ideal}$. The linear phase profile to place the trap at $d = \frac{f_3}{f_4}\frac{\lambda f'}{T}$ will accidentally be $e^{i\frac{2\pi a}{T}x}$. Each period of the phase phase grating resulting from the *mod 2π* function can be expressed as follows:

$$e^{i\frac{2\pi a}{T}x} \cdot \text{rect}\left[\frac{x - \frac{T}{2}}{T}\right] \tag{A.9}$$

Appendix. Trap steering efficiency and positioning accuracy calculations from Fourier optics

The entire hologram, obtained by replicating Eq. A.9 with a comb function with period T and defining the finite size of the SLM, L, becomes (Fig. A.2, see Eq. 3.9):

$$U(x) = A \cdot \text{rect}\left(\frac{x - x_0}{L}\right) \cdot \left[\sum_{n=-\infty}^{\infty} \delta(x - nT) * \left(e^{i\frac{2\pi a}{T}x} \cdot \text{rect}\left[\frac{x - \frac{T}{2}}{T}\right]\right)\right] \quad \text{(A.10)}$$

where L is the SLM size and T is the phase grating period. Parameter x_0 expresses a hologram shift that can be implemented through the addition of a constant phase term, so-called ψ_0 (see Section 3.2.2.3): $x_0 = \frac{L}{2} - \frac{\psi_0}{2\pi}T$.
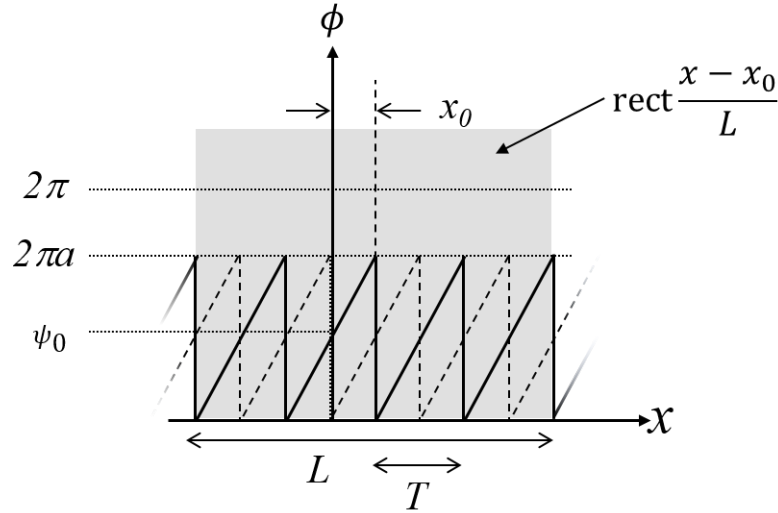
Figure A.2.: Hologram.

Eq. A.9 Fourier-transforms as:

$$\delta\left(u - \frac{a}{T}\right) * \text{sinc}(Tu)\, e^{-i2\pi\frac{T}{2}u} = \text{sinc}\left[T\left(u - \frac{a}{T}\right)\right] e^{-2\pi\left(u - \frac{a}{T}\right)T} \quad \text{(A.11)}$$

The light intensity at the trapping plane will be (see Eq. 3.10):

130

$$\left| \tilde{U}\left(u\right) \right|^2 \propto \left| \left[\mathrm{sinc}\left(Lu\right)e^{-i2\pi x_0 u}\right] * \left[\sum_{n=-\infty}^{\infty} \delta\left(u - \frac{n}{T}\right) \cdot \mathrm{sinc}\left[T\left(u - \frac{a}{T}\right)\right] e^{-i\pi\left(u - \frac{a}{T}\right)T} \right] \right|^2$$

$$\propto \left| \sum_{n=-\infty}^{\infty} \left\{ \left[\mathrm{sinc}\left(Lu\right)e^{-i2\pi x_0 u}\right] * \left[\delta\left(u - \frac{n}{T}\right) \cdot \mathrm{sinc}\left(n - a\right)e^{-i\pi(n-a)} \right] \right\} \right|^2$$

$$\propto \left| \sum_{n=-\infty}^{\infty} \mathrm{sinc}\left(n - a\right)e^{-i\pi(n-a)} \, \mathrm{sinc}\left[L\left(u - \frac{n}{T}\right)\right] e^{-i2\pi x_0\left(u - \frac{n}{T}\right)} \right|^2$$

$$\propto \left| \sum_{n=-\infty}^{\infty} \mathrm{sinc}\left(n - a\right)e^{i\pi\left(\frac{2x_0}{T} - 1\right)n} \, \mathrm{sinc}\left[L\left(u - \frac{n}{T}\right)\right] \right|^2 \qquad (A.12)$$

List of contributions

Publications:

1. F. Català, F. Marsà, M. Montes-Usategui, A. Farré, E. Martín-Badosa, "Extending calibration-free force measurements to optically-trapped rod-shaped samples", Sci. Rep. 7, 42960 (2017).

2. F. Català, F. Marsà, M. Montes-Usategui, A. Farré, E. Martín-Badosa, "Influence of experimental parameters on the laser heating of an optical trap", Sci. Rep. 7(1), 16052 (2017).

Conference proceedings:

1. F. Català, F. Marsà, A. Farré, M. Montes-Usategui, E. Martín-Badosa, "Momentum measurements with holographic optical tweezers for exploring force detection capabilities on irregular samples", SPIE Optics+Photonics, 9164-9, San Diego, August 2014.

2. A. Farré, J. Mas, F. Marsà, F. Català, J. Sancho-Parramon, E. Martín-Badosa, and M. Montes-Usategui, "Force measurements in complex samples with optical tweezers", 2015 OSA Biomedical Optics & Photonics Congress: Optics in the Life Sciences (Optical Trapping Applications), Vancouver, April 2015.

3. R. Bola, F. Català, M. Montes-Usategui, E. Martín Badosa, "Optical tweezers for force measurements and rheological studies on biological samples", 15th Workshop on Information Optics, Barcelona, July 2016.

4. E. Martín-Badosa, F. Català, J. Mas, M. Montes-Usategui, "Force measurement in the manipulation of complex samples with holographic optical tweezers", 15th Workshop on Information Optics, Barcelona, July 2016.

Other contributions:

1. F. Català, E. Martín-Badosa, "Beam steering accuracy in holographic optical tweezers" (oral), 7th International Nanoscience Student Conference, University College London, August 2013.

2. F. Català, A. Farré, F. Marsà, M. Montes-Usategui, E. Martín-Badosa, "Force measurements on irregular samples with holographic optical tweezers" (poster), VI Jornada IN2UB, Barcelona, June 2014.

3. F. Català, F. Marsà, M. Montes-Usategui, <u>A. Farré</u>, and E. Martín-Badosa, "Measurement of forces on non-spherical particles with holographic optical tweezers" (oral), 23rd Congress of the International Commission for Optics (ICO-23, Enlightening the Future), Santiago de Compostela, August 2014.

4. F. Català, F. Marsà, M. Montes-Usategui, A. Farré, and <u>E. Martín-Badosa</u>, "Force detection on non-spherical samples with holographic optical tweezers" (oral), Trends in Optical Micromanipulation III, Obergurgl, January 2015.

5. <u>F. Català</u>, F. Marsà, M. Montes-Usategui, A. Farré, E. Martín-Badosa, "Medida directa de fuerzas en pinzas ópticas holográficas y muestras irregulares" (oral), XI Reunión Nacional de Óptica, Salamanca, September 2015.

6. <u>E. Martín-Badosa</u>, A. Farré, J. Mas, F. Català, F. Marsà, J. Sancho-Parramon, M. Montes-Usategui, "Nuevas perspectivas en la medida de fuerzas ópticas" (oral), XI Reunión Nacional de Óptica, Salamanca, September 2015.

7. <u>F. Català</u>, F. Marsà, M. Montes-Usategui, A. Farré, E. Martín-Badosa, "Direct force measurements on irregular samples in a holographic optical tweezers set-up" (oral), XXXI Trobades científiques de la Mediterrània Josep Miquel Vidal, Maó, October 2015.

8. <u>F. Català</u>, F. Marsà, M. Montes-Usategui, A. Farré, E. Martín-Badosa, "Sample heating in optical tweezers" (poster), 1st Biology for Physics Conference: is there new physics in living matter?, Barcelona, January 2017.

9. <u>F. Català</u>, F. Marsà, M. Montes-Usategui, A. Farré, E. Martín-Badosa, "Direct drag force measurements to detect local sample heating in optical tweezers" (poster), 10th Anniversary IN2UB, Barcelona, January 2017.

10. <u>R. Bola</u>, <u>F. Català</u>, <u>R. Serrano</u>, E. Martín-Badosa, M. Montes-Usategui, "Light momentum measurements for force profile determination in an optical trap" (poster), New frontiers in optical trapping and optical manipulation, Institut de Ciències Fotòniques (ICFO), Castelldefels (Barcelona), July 2017.

11. <u>F. Català</u>, M. Montes-Usategui, T. Betz, A. Farré, "Optical trapping and light-momentum force detection in embryonic tissue" (oral), in XII Reunión Nacional de Óptica, Castelló, July 2018.

Acknowledgements

Bibliography

[1] K. C. Neuman and A. Nagy, "Single-molecule force spectroscopy: Optical tweezers, magnetic tweezers and atomic force microscopy," Nature Methods **5**, 491–505 (2008).

[2] K. Sugimura, P.-F. Lenne, and F. Graner, "Measuring forces and stresses in situ in living tissues," Development **143**, 186–196 (2016).

[3] L. Valon, A. Marín-Llauradó, T. Wyatt, G. Charras, and X. Trepat, "Optogenetic control of cellular forces and mechanotransduction," Nature Communications **8**, 14396 (2017).

[4] A. Ashkin, "Acceleration and Trapping of Particles by Radiation Pressure," Physical Review Letters **24**, 156–159 (1970).

[5] A. Ashkin, J. M. Dziedzic, J. E. Bjorkholm, and S. Chu, "Observation of a single-beam gradient force optical trap for dielectric particles," Optics Letters **11**, 288–290 (1986).

[6] K. Svoboda and S. M. Block, "Biological Applications of Optical Forces," Annual Review of Biophysics and Biomolecular Structure **23**, 247–285 (1994).

[7] K. C. Neuman and S. M. Block, "Optical trapping," Review of Scientific Instruments **75**, 2787–2809 (2006).

[8] S. P. Gross, "Application of optical traps in vivo," Methods in Enzymology **361**, 162–174 (2003).

[9] K. Bambardekar, R. Clément, O. Blanc, C. Chardès, and P.-F. Lenne, "Direct laser manipulation reveals the mechanics of cell contacts in vivo," Proceedings of the National Academy of Sciences **112**, 1416–1421 (2015).

[10] Y. Harada and T. Asakura, "Radiation forces on a dielectric sphere in the Rayleigh scattering regime," Optics Communications **124**, 529–541 (1996).

[11] R. C. Gauthier, "Computation of the optical trapping force using an FDTD based technique," Optics Express **13**, 3707–3718 (2005).

[12] T. A. Nieminen, V. L. Y. Loke, A. B. Stilgoe, G. Knöner, A. M. Brańczyk, N. R. Heckenberg, and H. Rubinsztein-Dunlop, "Optical tweezers computational toolbox," Journal of Optics A: Pure and Applied Optics **9**, 196–203 (2007).

[13] K. Svoboda and S. M. Block, "Force and velocity measured for single kinesin molecules," Cell **77**, 773–784 (1994).

[14] E. Stellamanns, S. Uppaluri, A. Hochstetter, N. Heddergott, M. Engstler, and T. Pfohl, "Optical trapping reveals propulsion forces, power generation and motility efficiency of the unicellular parasites Trypanosoma brucei brucei," Scientific Reports **4**, 6515 (2014).

[15] S. Chattopadhyay, R. Moldovan, C. Yeung, and X.-L. Wu, "Swimming efficiency of bacterium Escherichia coli," Proceedings of the National Academy of Sciences **103**, 13712–13717 (2006).

[16] C. Bustamante, Z. Bryant, and S. B. Smith, "Ten years of tension: single molecule DNA mechanics," Nature **421**, 423–427 (2003).

[17] T. F. Bartsch, R. A. Longoria, E.-L. Florin, and G. T. Shubeita, "Lipid droplets purified from drosophila embryos as an endogenous handle for precise motor transport measurements," Biophysical Journal **105**, 1182–1191 (2013).

[18] B. H. Blehm, T. A. Schroer, K. M. Trybus, Y. R. Chemla, and P. R. Selvin, "In vivo optical trapping indicates kinesin's stall force is reduced by dynein during intracellular transport," Proceedings of the National Academy of Sciences **110**, 3381–3386 (2013).

[19] S. B. Smith, Y. Cui, C. Bustamante, C. B. M. in Enzymology, and U. 2003, "Optical-Trap Force transducer that operates by direct measurement of light momentum," Methods in enzymology. **361**, 124–162 (2003).

[20] A. Farré and M. Montes-Usategui, "A force detection technique for single-beam optical traps based on direct measurement of light momentum changes," Optics Express **18**, 11955–11968 (2010).

[21] A. Farré, F. Marsà, and M. Montes-Usategui, "Optimized back-focal-plane interferometry directly measures forces of optically trapped particles," Optics Express **20**, 12270–12291 (2012).

[22] J. E. Curtis, B. A. Koss, and D. G. Grier, "Dynamic holographic optical tweezers," Optics Communications **207**, 169–175 (2002).

[23] C. Schmitz, J. Spatz, and J. E. Curtis, "High-precision steering of multiple holographic optical traps," Optics Express **13**, 8678–8685 (2005).

[24] R. Di Leonardo, F. Ianni, and G. Ruocco, "Computer generation of optimal holograms for optical trap arrays," Optics Express **15**, 1913–1922 (2007).

[25] E. Martín-Badosa, M. Montes-Usategui, A. Carnicer, J. Andilla, E. Pleguezuelos, and I. Juvells, "Design strategies for optimizing holographic optical tweezers set-ups," Journal of Optics A: Pure and Applied Optics **9**, 267–277 (2007).

[26] D. Engström, J. Bengtsson, E. Eriksson, and M. Goksör, "Improved beam steering accuracy of a single beam with a 1D phase-only spatial light modulator," Optics Express **16**, 18275–18287 (2008).

[27] A. Jesacher, S. Fürhapter, S. Bernet, and M. Ritsch-Marte, "Size selective trapping with optical "cogwheel" tweezers," Optics Express **12**, 4129–4135 (2004).

[28] M. J. Padgett and R. Bowman, "Tweezers with a twist," Nature Photonics **5**, 343–348 (2011).

[29] A. S. Bezryadina, D. C. Preece, J. C. Chen, and Z. Chen, "Optical disassembly of cellular clusters by tunable "tug-of-war" tweezers," Light: Science and Applications **5**, 16158 (2016).

[30] N. Khatibzadeh, A. B. Stilgoe, A. A. M. Bui, Y. Rocha, G. M. Cruz, V. Loke, L. Z. Shi, T. A. Nieminen, H. Rubinsztein-Dunlop, and M. W. Berns, "Determination of motility forces on isolated chromosomes with laser tweezers," Scientific Reports **4**, 6866 (2014).

[31] S. N. Olof, J. A. Grieve, D. B. Phillips, H. Rosenkranz, M. L. Yallop, M. J. Miles, A. J. Patil, S. Mann, and D. M. Carberry, "Measuring nanoscale forces with living probes," Nano Letters **12**, 6018–6023 (2012).

[32] D. B. Phillips, M. J. Padgett, S. Hanna, Y. L. Ho, D. M. Carberry, M. J. Miles, and S. H. Simpson, "Shape-induced force fields in optical trapping," Nature Photonics **8**, 400–405 (2014).

[33] D. B. Phillips, D. M. Carberry, S. H. Simpson, H. Schäfer, M. Steinhart, R. Bowman, G. M. Gibson, M. J. Padgett, S. Hanna, and M. J. Miles, "Optimizing the optical trapping stiffness of holographically trapped microrods using high-speed video tracking," Journal of Optics **13**, 044023 (2011).

[34] N. McAlinden, D. G. Glass, O. R. Millington, and A. J. Wright, "Accurate position tracking of optically trapped live cells," Biomedical Optics Express **5**, 1026–1037 (2014).

[35] E. J. Peterman, F. Gittes, and C. F. Schmidt, "Laser-Induced Heating in Optical Traps," Biophysical Journal **84**, 1308–1316 (2003).

[36] P. M. Celliers and J. Conia, "Measurement of localized heating in the focus of an optical trap," Applied Optics **39**, 3396–3407 (2000).

[37] H. Mao, J. R. Arias-Gonzalez, S. B. Smith, I. Tinoco, and C. Bustamante, "Temperature control methods in a laser tweezers system," Biophysical Journal **89**, 1308–1316 (2005).

[38] P. Haro-González, W. T. Ramsay, L. M. Maestro, B. Del Rosal, K. Santacruz-Gomez, M. D. C. Iglesias-De La Cruz, F. Sanz-Rodríguez, J. Y. Chooi, P. R. Sevilla, M. Bettinelli, D. Choudhury, A. K. Kar, J. G. Solé, D. Jaque, and L. Paterson, "Quantum dot-based thermal spectroscopy and imaging of optically trapped microspheres and single cells," Small **9**, 2162–2170 (2013).

[39] L. J. Kong, Y. Zhu, Y. Song, and J. Y. Yang, "Beam steering approach for high-precision spatial light modulators," Chinese Optics Letters **8**, 1085–1089 (2010).

[40] A. Callegari, M. Mijalkov, A. B. Gököz, and G. Volpe, "Computational toolbox for optical tweezers in geometrical optics," Journal of the Optical Society of America B **32**, 11–19 (2015).

[41] D. Zhang, X.-C. Yuan, S. C. Tjin, and S. Krishnan, "Rigorous time domain simulation of momentum transfer between light and microscopic particles in optical trapping," Optics Express **12**, 2220–2230 (2004).

[42] I. C. Lenton, A. B. Stilgoe, H. Rubinsztein-Dunlop, and T. A. Nieminen, "Visual guide to optical tweezers," European Journal of Physics **38**, 034009 (2017).

[43] T. A. Nieminen, N. Du Preez-Wilkinson, A. B. Stilgoe, V. L. Loke, A. A. M. Bui, and H. Rubinsztein-Dunlop, "Optical tweezers: theory and modelling," Journal of Quantitative Spectroscopy and Radiative Transfer **146**, 59–80 (2014).

[44] A. A. M. Bui, A. B. Stilgoe, I. C. Lenton, L. J. Gibson, A. V. Kashchuk, S. Zhang, H. Rubinsztein-Dunlop, and T. A. Nieminen, "Theory and practice of simulation of optical tweezers," Journal of Quantitative Spectroscopy and Radiative Transfer **195**, 66–75 (2017).

[45] I. Verdeny, A. Farré, J. Mas, C. López-Quesada, E. Martín-Badosa, and M. Montes-Usategui, "Optical trapping: A review of essential concepts," Óptica Pura y Aplicada **44**, 527–551 (2011).

[46] G. M. Gibson, J. Leach, S. Keen, A. J. Wright, and M. J. Padgett, "Measuring the accuracy of particle position and force in optical tweezers using high-speed video microscopy," Optics Express **16**, 14561–14570 (2008).

[47] A. Huhle, D. Klaue, H. Brutzer, P. Daldrop, S. Joo, O. Otto, U. F. Keyser, and R. Seidel, "Camera-based three-dimensional real-time particle tracking at kHz rates and Ångström accuracy," Nature Communications **6**, 5885 (2015).

[48] F. Marsà, A. Farré, E. Martín-Badosa, and M. Montes-Usategui, "Holographic optical tweezers combined with back-focal-plane displacement detection," Optics Express **21**, 30282–30294 (2013).

[49] F. Gittes and C. F. Schmidt, "Interference model for back-focal-plane displacement detection in optical tweezers," Optics Letters **23**, 7–9 (1998).

[50] A. Rohrbach, H. Kress, and E. H. K. Stelzer, "Three-dimensional tracking of small spheres in focused laser beams: influence of the detection angular aperture," Optics Letters **28**, 411–413 (2003).

[51] D. Ott, S. Nader, S. N. S. Reihani, and L. B. Oddershede, "Simultaneous three-dimensional tracking of individual signals from multi-trap optical tweezers using fast and accurate photodiode detection," Optics Express **22**, 23661–23672 (2014).

[52] K. C. Vermeulen, J. Van Mameren, G. J. M. Stienen, E. J. Peterman, G. J. Wuite, and C. F. Schmidt, "Calibrating bead displacements in optical tweezers using acousto-optic deflectors," Review of Scientific Instruments **77**, 013704 (2006).

[53] J. R. Staunton, B. Blehm, A. Devine, and K. Tanner, "In situ calibration of position detection in an optical trap for active microrheology in viscous materials," Optics Express **25**, 1746–1761 (2017).

[54] A. Khorshad, S. Nader, S. N. S. Reihani, and M. Tavassoly, "Moiré deflectometry-based position detection for optical tweezers," Optics Letters **42**, 3506–3509 (2017).

[55] S. M. Mousavi, A. Samadi, F. Hajizadeh, and S. N. S. Reihani, "Extended linear detection range for optical tweezers using a stop at the back focal plane of the condenser," Journal of Optics **17**, 065606 (2015).

[56] T. F. Dixon, L. W. Russell, A. Andres-Arroyo, and P. J. Reece, "Using back focal plane interferometry to probe the influence of Zernike aberrations in optical tweezers," Optics Letters **42**, 2968–2971 (2017).

[57] S. Bianchi, F. Saglimbeni, A. Lepore, and R. Di Leonardo, "Polar features in the flagellar propulsion of E. coli bacteria," Physical Review E - Statistical, Nonlinear, and Soft Matter Physics **91**, 062705 (2015).

[58] I. M. Tolić-Nørrelykke, K. Berg-Sørensen, and H. Flyvbjerg, "MatLab program for precision calibration of optical tweezers," Computer Physics Communications **159**, 225–240 (2004).

[59] A. A. M. Bui, A. B. Stilgoe, N. Khatibzadeh, T. A. Nieminen, M. W. Berns, and H. Rubinsztein-Dunlop, "Escape forces and trajectories in optical tweezers and their effect on calibration," Optics Express **23**, 24317–24330 (2015).

[60] W. Grange, S. Husale, H. J. Güntherodt, and M. Hegner, "Optical tweezers system measuring the change in light momentum flux," Review of Scientific Instruments **73**, 2308–2316 (2002).

[61] M. Ribezzi-Crivellari, J. M. Huguet, and F. Ritort, "Counter-propagating dual-trap optical tweezers based on linear momentum conservation," Review of Scientific Instruments **84**, 043104 (2013).

[62] A. Farré, F. Marsà, and M. Montes-Usategui, "Beyond the Hookean Spring Model: Direct Measurement of Optical Forces Through Light Momentum Changes," in "Optical Tweezers. Methods and Protocols," , vol. 1486, A. Gennerich, ed. (Springer, 2017), pp. 41–76.

[63] G. Thalhammer, L. Obmascher, and M. Ritsch-Marte, "Direct measurement of axial optical forces," Optics Express **23**, 6112–6129 (2015).

[64] C. Bustamante and S. B. Smith, "Light-force sensor and method for measuring axial optical-trap forces from changes in light momentum along an optic axis. US 7,133,132 B2," (2006).

[65] J. Mas, A. Farré, C. López-Quesada, X. Fernandez, E. Martín-Badosa, M. Montes-Usategui, and C. Lopez-Quesada, "Measuring stall forces in vivo

with optical tweezers through light momentum changes," in "Optical Trapping and Optical Micromanipulation VIII. Proceedings of SPIE.", (2011), p. 809726.

[66] J. Mas, A. Farré, J. Sancho-Parramon, E. Martín-Badosa, and M. Montes-Usategui, "Force measurements with optical tweezers inside living cells," in "Optical Trapping and Optical Micromanipulation XI. Proceedings of SPIE.", (2014), p. 91640U.

[67] Y. Jun, S. K. Tripathy, B. R. J. Narayanareddy, M. K. Mattson-Hoss, and S. P. Gross, "Calibration of optical tweezers for in vivo force measurements: How do different approaches compare?" Biophysical Journal **107**, 1474–1484 (2014).

[68] M. A. Taylor, M. Waleed, A. B. Stilgoe, H. Rubinsztein-Dunlop, and W. P. Bowen, "Enhanced optical trapping via structured scattering," Nature Photonics **9**, 669–673 (2015).

[69] F. Català, F. Marsà, M. Montes-Usategui, A. Farré, and E. Martín-Badosa, "Extending calibration-free force measurements to optically-trapped rod-shaped samples," Scientific Reports **7**, 42960 (2017).

[70] F. Català, F. Marsà, M. Montes-Usategui, A. Farré, and E. Martín-Badosa, "Influence of experimental parameters on the laser heating of an optical trap," Scientific Reports **7**, 16052 (2017).

[71] M. Robert, O. Neus, D. Cornelia, R. Meissner, N. Oliver, and C. Denz, "Optical Force Sensing with Cylindrical Microcontainers," Particle & Particle Systems Characterization p. 1800062 (2018).

[72] A. A. Bui, A. V. Kashchuk, M. A. Balanant, T. A. Nieminen, H. Rubinsztein-Dunlop, and A. B. Stilgoe, "Calibration of force detection for arbitrarily shaped particles in optical tweezers," Scientific Reports **8**, 1–12 (2018).

[73] Y. Hayasaki, M. Itoh, T. Yatagai, and N. Nishida, "Nonmechanical optical manipulation of microparticle using spatial light modulator," Optical Review **6**, 24–27 (1999).

[74] J. Liesener, M. Reicherter, T. Haist, and H. J. Tiziani, "Multi-functional optical tweezers using computer-generated holograms," Optics Communications **185**, 77–82 (2000).

[75] C. López-Quesada, J. Andilla, and E. Martín-Badosa, "Correction of aberration in holographic optical tweezers using a Shack-Hartmann sensor," Applied Optics **48**, 1084–1090 (2009).

[76] D. G. Grier, "A revolution in optical manipulation," Nature **424**, 810–816 (2003).

[77] A. Farré, M. Shayegan, C. López-Quesada, G. A. Blab, M. Montes-Usategui, N. R. Forde, and E. Martín-Badosa, "Positional stability of holographic optical traps," Optics Express **19**, 21370–21384 (2011).

[78] J. Albero, P. García-Martínez, J. L. Martínez, and I. Moreno, "Second order diffractive optical elements in a spatial light modulator with large phase dynamic range," Optics and Lasers in Engineering **51**, 111–115 (2013).

[79] V. Calero, P. García-Martínez, J. Albero, M. M. Sánchez-López, and I. Moreno, "Liquid crystal spatial light modulator with very large phase modulation operating in high harmonic orders," Optics Letters **38**, 4663–4666 (2013).

[80] D. Engström, M. Persson, J. Bengtsson, and M. Goksör, "Calibration of spatial light modulators suffering from spatially varying phase response," Optics Express **21**, 16086–16103 (2013).

[81] A. van der Horst and N. R. Forde, "Calibration of dynamic holographic optical tweezers for force measurements on biomaterials," Optics Express **16**, 20987–21003 (2008).

[82] J. W. Goodman, *Introduction to Fourier optics* (Roberts and Company Publishers, 2005).

[83] Z. Zhang, H. Yang, B. Robertson, M. Redmond, M. Pivnenko, N. Collings, W. A. Crossland, and D. Chu, "Diffraction based phase compensation method for phase-only liquid crystal on silicon devices in operation," Applied Optics **51**, 3837–3846 (2012).

[84] F. Czerwinski, A. C. Richardson, and L. B. Oddershede, "Quantifying Noise in Optical Tweezers by Allan Variance," Optics Express **17**, 13255–13269 (2009).

[85] J. Mas, "Investigation on force detection methods for optical trapping and sensing inside living cells," Ph.D. thesis (2016).

[86] M. Montes-Usategui, E. Pleguezuelos, J. Andilla, and E. Martín-Badosa, "Fast generation of holographic optical tweezers by random mask encoding of Fourier components," Optics Express **14**, 2101–2107 (2006).

[87] Y. Roichman and D. G. Grier, "Projecting extended optical traps with shape-phase holography," Optics Letters **31**, 1675–1677 (2006).

[88] S.-H. Lee, Y. Roichman, and D. G. Grier, "Optical solenoid beams," Optics Express **18**, 6988–6993 (2010).

[89] O. Brzobohatý, V. Karásek, M. Šiler, L. Chvátal, T. Čižmár, and P. Zemánek, "Experimental demonstration of optical transport, sorting and self-arrangement using a "tractor beam"," Nature Photonics **7**, 123–127 (2013).

[90] M. D. Koch and A. Rohrbach, "Object-adapted optical trapping and shape-tracking of energy-switching helical bacteria," Nature Photonics **6**, 680–686 (2012).

[91] M. D. Koch and A. Rohrbach, "How to calibrate an object-adapted optical trap for force sensing and interferometric shape tracking of asymmetric structures," Optics Express **22**, 25242–25257 (2014).

[92] J. W. Kerssemakers, M. E. Janson, A. van der Horst, and M. Dogterom, "Optical trap setup for measuring microtubule pushing forces," Applied Physics Letters **83**, 4441–4443 (2003).

[93] J. W. J. Kerssemakers, E. Laura Munteanu, L. Laan, T. L. Noetzel, M. E. Janson, and M. Dogterom, "Assembly dynamics of microtubules at molecular resolution," Nature **442**, 709–712 (2006).

[94] K. Berg-Sørensen and H. Flyvbjerg, "Power spectrum analysis for optical tweezers," Review of Scientific Instruments **75**, 594–612 (2004).

[95] A. Farré and F. Marsà, "Optical device for placement in the optical train of a microscope and method of manufacturing such a device, EP 2 884 325 B1," (2017).

[96] N. B. Viana, M. S. Rocha, O. N. Mesquita, A. Mazolli, and P. A. Neto Maia, "Characterization of objective transmittance for optical tweezers," Applied Optics **45**, 4263–4269 (2006).

[97] M. Mahamdeh, C. Pérez Campos, and E. Schäffer, "Under-filling trapping objectives optimizes the use of the available laser power in optical tweezers," Optics Express **19**, 11759–11768 (2011).

[98] R. Power, J. P. Reid, S. Anand, D. McGloin, A. Almohamedi, N. S. Mistry, and A. J. Hudson, "Observation of the binary coalescence and equilibration of micrometer-sized droplets of aqueous aerosol in a single-beam gradient-force optical trap," Journal of Physical Chemistry A **116**, 8873–8884 (2012).

[99] L. Collard, D. Perez-Guaita, B. H. Faraj, B. R. Wood, R. Wallis, P. W. Andrew, and A. J. Hudson, "Light Scattering by Optically-Trapped Vesicles Affords Unprecedented Temporal Resolution of Lipid-Raft Dynamics," Scientific Reports **7**, 1–11 (2017).

[100] G. Volpe, G. Kozyreff, and D. Petrov, "Backscattering position detection for photonic force microscopy," Journal of Applied Physics **102**, 084701 (2007).

[101] J. Huisstede, K. van der Werf, M. Bennink, and V. Subramaniam, "Force detection in optical tweezers using backscattered light," Optics Express **13**, 1113–1123 (2005).

[102] M. Dao, C. T. Lim, and S. Suresh, "Mechanics of the human red blood cell deformed by optical tweezers," Journal of the Mechanics and Physics of Solids **51**, 2259–2280 (2003).

[103] R. E. Jensen, A. E. Aiken Hobbs, K. L. Cerveny, and H. Sesaki, "Yeast mitochondrial dynamics: Fusion, division, segregation, and shape," Microscopy Research and Technique **51**, 573–583 (2000).

[104] D. M. Gates, H. J. Keegan, J. C. Schleter, and V. R. Weidner, "Spectral Properties of Plants," Applied Optics **4**, 11–20 (1965).

[105] T. L. Min, P. J. Mears, L. M. Chubiz, C. V. Rao, I. Golding, and Y. R. Chemla, "High-resolution, long-term characterization of bacterial motility using optical tweezers," Nature Methods **6**, 831–835 (2009).

[106] A. Samadi, C. Zhang, J. C. Chen, S. N. S. Reihani, and Z. Chen, "Evaluating the toxic effect of an antimicrobial agent on single bacterial cells with optical tweezers," Biomedical Optics Express **6**, 112–117 (2015).

[107] I. A. Martínez, S. Campoy, M. Tort, M. Llagostera, and D. Petrov, "A Simple Technique Based on a Single Optical Trap for the Determination of Bacterial Swimming Pattern," PLoS ONE **8**, e61630 (2013).

[108] T. Altindal, S. Chattopadhyay, and X.-L. Wu, "Bacterial Chemotaxis in an Optical Trap," PLoS ONE **6**, e18231 (2011).

[109] R. C. Gauthier, M. Ashman, and C. P. Grover, "Experimental Confirmation of the Optical-Trapping Properties of Cylindrical Objects," Applied Optics **38**, 4861–4869 (1999).

[110] S. H. Simpson and S. Hanna, "Holographic optical trapping of microrods and nanowires," Journal of the Optical Society of America A **27**, 1255–1264 (2010).

[111] A. A. M. Bui, A. B. Stilgoe, T. a. Nieminen, and H. Rubinsztein-Dunlop, "Calibration of nonspherical particles in optical tweezers using only position measurement," Optics Letters **38**, 1244–1246 (2013).

[112] C. Brennen and H. Winet, "Fluid Mechanics of Propulsion by Cilia and Flagella," Annual Review of Fluid Mechanics **9**, 339–398 (1977).

[113] B. Carrasco and J. G. De La Torre, "Hydrodynamic properties of rigid particles: Comparison of different modeling and computational procedures," Biophysical Journal **76**, 3044–3057 (1999).

[114] J. C. Crocker, "Measurement of the hydrodynamic corrections to the Brownian motion of two colloidal spheres," The Journal of Chemical Physics **106**, 2837–2840 (1997).

[115] W. Singer, S. Bernet, N. Hecker, and M. Ritsch-Marte, "Three-dimensional force calibration of optical tweezers," Journal of Modern Optics **47-14**, 2921–2931 (2000).

[116] P. Y. Liu, L. K. Chin, W. Ser, T. C. Ayi, P. H. Yap, T. Bourouina, and Y. Leprince-Wang, "Real-Time measurement of single bacterium's refractive index using optofluidic immersion refractometry," Procedia Engineering **87**, 356–359 (2014).

[117] A. Ortega and J. G. De La Torre, "Hydrodynamic properties of rodlike and disklike particles in dilute solution," The Journal of Chemical Physics **119**, 9914–9919 (2003).

[118] M. Fischer, A. C. Richardson, S. N. S. Reihani, L. B. Oddershede, and K. Berg-Sørensen, "Active-passive calibration of optical tweezers in viscoelastic media," Review of Scientific Instruments **81**, 015103 (2010).

[119] M. A. Welte, S. P. Gross, M. Postner, S. M. Block, and E. F. Wieschaus, "Developmental regulation of vesicle transport in Drosophila embryos: Forces and kinetics," Cell **92**, 547–557 (1998).

[120] C. L. Curl, C. J. Bellair, T. Harris, B. E. Allman, P. J. Harris, A. G. Stewart, A. Roberts, K. A. Nugent, and L. M. D. Delbridge, "Refractive index measurement in viable cells using quantitative phase-amplitude microscopy and confocal microscopy." Cytometry. Part A : the journal of the International Society for Analytical Cytology **65**, 88–92 (2005).

[121] G. S. Gotterer, T. E. Thompson, and A. L. Lehninger, "Angular light-scattering studies on isolated mitochondria," Journal of Cell Biology **10**, 15–21 (1961).

[122] Y. Liu, D. K. Cheng, G. J. Sonek, M. W. Berns, C. F. Chapman, and B. J. Tromberg, "Evidence for localized cell heating induced by infrared optical tweezers," Biophysical Journal **68**, 2137–2144 (1995).

[123] Y. Liu, G. J. Sonek, M. W. Berns, and B. J. Tromberg, "Physiological monitoring of optically trapped cells: Assessing the effects of confinement by 1064-nm laser tweezers using microfluorometry," Biophysical Journal **71**, 2158–2167 (1996).

[124] S. Ebert, K. Travis, B. Lincoln, and J. Guck, "Fluorescence ratio thermometry in a microfluidic dual-beam laser trap," Optics Express **15**, 15493–15499 (2007).

[125] F. Wetzel, S. Rönicke, K. Müller, M. Gyger, D. Rose, M. Zink, and J. Käs, "Single cell viability and impact of heating by laser absorption," European Biophysics Journal **40**, 1109–1114 (2011).

[126] S. C. Kuo, "A simple assay for local heating by optical tweezers." Methods in cell biology **55**, 43–45 (1998).

[127] S. Kedenburg, M. Vieweg, T. Gissibl, and H. Giessen, "Linear refractive index and absorption measurements of nonlinear optical liquids in the visible and near-infrared spectral region," Optical Materials Express **2**, 1588–1611 (2012).

[128] E. A. Abbondanzieri, J. W. Shaevitz, and S. M. Block, "Picocalorimetry of transcription by RNA polymerase," Biophysical Journal **89**, 61–63 (2005).

[129] K. C. Neuman, E. H. Chadd, G. F. Liou, K. Bergman, and S. M. Block, "Characterization of photodamage to Escherichia coli in optical traps," Biophysical Journal **77**, 2856–2863 (1999).

[130] P. Rodriguez Sevilla, Y. Zhang, P. Haro-González, F. Sanz-Rodríguez, F. Jaque, J. García Solé, X. Liu, and D. Jaque, "Avoiding induced heating in optical trap," in "Optical Trapping and Optical Micromanipulation XIV. Proceedings of SPIE.", (2017), p. 1034716.

[131] G. Leitz, E. Fällman, S. Tuck, and O. Axner, "Stress response in Caenorhabditis elegans caused by optical tweezers: Wavelength, power, and time dependence," Biophysical Journal **82**, 2224–2231 (2002).

[132] C. B. Kimmel, W. W. Ballard, S. R. Kimmel, B. Ullmann, and T. F. Schilling, "Stages of embryonic development of the zebrafish," Developmental Dynamics **203**, 253–310 (1995).

[133] B. Wallmeyer, S. Trinschek, S. Yigit, U. Thiele, and T. Betz, "Collective Cell Migration in Embryogenesis Follows the Laws of Wetting," Biophysical Journal **114**, 213–222 (2018).

[134] F. Hörner, R. Meissner, S. Polali, J. Pfeiffer, T. Betz, C. Denz, and E. Raz, "Holographic optical tweezers-based in vivo manipulations in zebrafish embryos," Journal of Biophotonics **10**, 1–10 (2017).

[135] P. L. Johansen, F. Fenaroli, L. Evensen, G. Griffiths, and G. Koster, "Optical micromanipulation of nanoparticles and cells inside living zebrafish," Nature Communications **7**, 10974 (2016).

[136] S. Harlepp, F. Thalmann, G. Follain, and J. G. Goetz, "Hemodynamic forces can be accurately measured in vivo with optical tweezers," Molecular Biology of the Cell **28**, 3252–3260 (2017).

[137] I. A. Favre-Bulle, A. B. Stilgoe, H. Rubinsztein-Dunlop, and E. K. Scott, "Optical trapping of otoliths drives vestibular behaviours in larval zebrafish," Nature Communications **8**, 630 (2017).

[138] H. Turlier, D. A. Fedosov, B. Audoly, T. Auth, N. S. Gov, C. Sykes, J. F. Joanny, G. Gompper, and T. Betz, "Equilibrium physics breakdown reveals the active nature of red blood cell flickering," Nature Physics **12**, 513–520 (2016).

[139] W. W. Ahmed, É. Fodor, M. Almonacid, M. Bussonnier, M. H. Verlhac, N. Gov, P. Visco, F. van Wijland, and T. Betz, "Active Mechanics Reveal Molecular-Scale Force Kinetics in Living Oocytes," Biophysical Journal **114**, 1667–1679 (2018).

[140] C. López-Quesada, A.-S. Fontaine, A. Farré, M. Joseph, J. Selva, G. Egea, M. D. Ludevid, E. Martín-Badosa, and M. Montes-Usategui, "Artificially-induced organelles are optimal targets for optical trapping experiments in living cells," Biomedical Optics Express **5**, 1993–2008 (2014).